Seismic Hazard Analysis using the Numerical DDA Method

Thesis submitted in partial fulfillment
of the requirements for the degree of
"DOCTOR OF PHILOSOPHY"

by

Gony Yagoda-Biran

Submitted to the Senate of Ben-Gurion University
of the Negev

March 2013

Beer-Sheva

Seismic Hazard Analysis using the Numerical DDA Method

Thesis submitted in partial fulfillment
of the requirements for the degree of
"DOCTOR OF PHILOSOPHY"

by

Gony Yagoda-Biran

Submitted to the Senate of Ben-Gurion University
of the Negev

Approved by the advisor Prof. Yossef H. Hatzor ______________________

Approved by the Dean of the Kreitman School of Advanced Graduate Studies Prof. Michal Shapira

____

March 2013

Beer-Sheva

This work was carried out under the supervision of

Professor Yossef H. Hatzor

in the *Department of Geological and Environmental Sciences*

Faculty of Natural Sciences

Ben-Gurion University of the Negev

Research-Student's Affidavit when Submitting the Doctoral Thesis for Judgment

I, Gony Yagoda-Biran, whose signature appears below, hereby declare that:

I have written this Thesis by myself, except for the help and guidance offered by my Thesis Advisor.

The scientific materials included in this Thesis are products of my own research, culled from the period during which I was a research student.

Date: ____________________

Student's name: __________________

Signature:________________

Acknowledgements

I would like to extend my deep gratitude to my Ph.D. advisor, Prof. Yossi Hatzor, for his support and guidance, both academic and mental. After 10 years of working together, I hope this is the beginning of a beautiful friendship.

Dr. Gen-hua Shi is thanked for making the most recent version of 3D-DDA code available for this study, for fixing problems with the code and for useful advises.

I would like to thank my Ph.D. candidacy committee: Dr. Alon Ziv (from BGU at the time) and Prof. Jean Sulem from Ecole des Ponts Paris Tech for their comments and suggestions. I also want to thank Prof. Yehuda Eyal for all his help throughout the years.

I thank the three anonymous reviewers of the thesis for their comments and instructive suggestions.

I also thank Dr. Susan Hough of the USGS, for encouraging us to purse the challenging task of modeling dynamic deformation of discrete element systems in 3D. I thank Prof. Claudio Modena for his help and hospitality at L'Aquila.

Dr. Yuli Zaslavsky and his team from the Geophysical institute of Israel are thanked for conducting the site response analysis survey at Avdat National Park.

The people at National Park Authority are thanked for their help and cooperation: Orit Bortnik, Nili Dvash and Shmuel from Avdat National Park.

Financial support by the Israel Science Foundation through grant ISF-2201, Contract No. 556/08 is greatly acknowledged. The Kreitman School for Advanced Graduate Studies is much acknowledged for the Negev fellowship.

Yael Rosental is thanked for providing essential data and for useful discussions and advises.

The administrative staff at the Department of Geological and Environmental Sciences, mainly Mrs. Rivka Eini and Mrs. Zahala Sharabi, are thanked for their help.

My laboratory friends along the way are thanked for their advises, ideas, help, and time: Dagan Bakun-Mazor, Ilia Weinstein, Omer Biran, Yuval Tal, Elhanan Livne, Huirong Bao, Ksenia Bisnovat, Guy Davidesko, Omri Shitrit, Nir Badt and Ravit Zelig.

My family is thanked for being there for me and for expressing their interest in my research.

My children – Ziv and Nizan, are thanked for waiting for me everyday to pick them up, and helping me keep the right perspective of life.

And last – my man – Omer, is thanked for helping me in every possible way - in field work, in useful advises, in map drawing, and always – for holding my hand.

to Omer, my companion on the road,

and Ziv and Nizan, who joined along the way

Table of Contents

List of Figures

List of Tables

Abstract

This dissertation focuses on seismic hazard analysis through different aspects of the response of both natural and man-made structures to earthquake induced ground motions, as strong ground motions are recognized as one of the most significant damage-causing seismic hazards. The ground motions a particular site would experience during an earthquake are a function of primarily three variables: the source of the seismic waves, the path through which the waves travel, and the specific condition of the site they reach. The research presented in this thesis focuses on the last link in this chain: the site response. The numerical, discrete element, Discontinuous Deformation Analysis (DDA) method, is used in this research for both backward as well as forward analyses.

Throughout this dissertation the DDA method is used as a dynamic computational tool, both in its two-dimensional (2D) as well as three-dimensional (3D) formulation. Since mesh generation in DDA is a challenging task, particularly in 3D simulations due to the lack of a graphic interface in the original software package developed by Dr. Shi, a procedure for creating both 2D and 3D meshes in the DDA, using a computer aided design (CAD) software as a pre-processor, is developed here. The validity and accuracy of the 3D-DDA code were successfully verified with two analytical solutions. Still, many unsuccessful forward modeling trials with the 3D-DDA imply that the 3D-DDA in its current version is still immature for forward modeling of dynamic problems involving complex, multi-block systems.

First, the capability of the numerical 2D-DDA method to perform site response analysis is tested, for the first time. The resonance frequencies obtained for a multi-drum column modeled with DDA are compared to resonance frequencies measured in an experimental site response survey of the column. When the numerical control parameters are properly selected, good agreement is obtained between DDA and the geophysical site response survey in the field. It is found that the choice of the contact spring stiffness, or the numerical penalty, is directly related to the obtained resonance frequency mode as obtained with DDA. The best agreement with the

geophysical test is obtained with a relatively soft contact spring stiffness of k = (1/25) $E*L$, where E is the Young's modulus of the blocks and L is the average block diameter. This optimal k value falls within the range of acceptable k values obtained in preliminary calibration tests performed independently of the field data. The obtained resonance frequency is found to be independent of the time step interval selected. Furthermore, DDA returns only a single resonance mode, whereas the geophysical test results indicate two modes. This discrepancy can be explained by the fixed base used in the DDA model which inhibits soil structure interactions.

Natural rock slopes subjected to seismic excitations can be modeled in some cases by the model of a block on an inclined plane, subjected to a pseudo-static force. A failure mode chart for a block resting on an inclined plane and subjected to gravitational loading with the analytical solutions for limiting equilibrium were published long ago and are currently used routinely in rock slope stability investigations. The failure mode of a block on an incline is a function of three angles: the block angle δ, defining the geometry of the block, the slope inclination angle α, and the interface friction angle ϕ. In this dissertation a new failure mode chart is presented, that incorporates a pseudo-static horizontal force F, simulating the seismic forces that act upon a block during an earthquake. In the new chart, the failure mode of a block is a function of three angles as well, with δ and ϕ remaining the same, but a new angle is introduced, $\psi = \alpha + \beta$, with β being the angle between the resultant of the block's weight W and F, and the vertical direction. Analytical derivations of the newly suggested mode boundaries are presented, along with 2D and 3D numerical simulations that confirm the analytical basis for the proposed stability and mode chart.

Finally, paleo peak ground accelerations (PGA) are estimated for an ancient earthquake that caused damage in the Western Wall Tunnels in the old city of Jerusalem. The importance of such paleo-seismic approach is greatly acknowledged, as recorded data of strong earthquakes in the region are scarce, down to non-existing, and paelo-seismic research can better constrain the seismic risk of the region. Evidence of seismically induced damages can be readily observed at the Western Wall Tunnels. The tunnels are composed of buildings from about 500 BC up until the modern period. One of the interesting findings is a 100 m long bridge, composed of two floors of barrel vaults. In one of the vaults, namely vault 21, one block is displaced downwards by 7 cm relative to its neighbors. The 2D –DDA is utilized for numerical simulations of the vault,

both under gravity and earthquake excitations, with different friction angles and different overburden schemes. Interpretation of results leads to the conclusion that the damage to vault 21 was seismically induced, while the bridge was still serving its purpose, i.e. before it was buried by later constructions and fill materials. The estimated *PGA* required for causing the observed damage is rather high: between 1.5 and 2 *g*. The *PGA* calculated using attenuation relationship for Jerusalem, caused by ancient earthquakes for the relevant time period, is about one order of magnitude smaller: 0.14 and 0.5 *g*, for the earthquakes of 362 and 746 AD, respectively. This requires amplification of the seismic waves beneath the bridge. It is reasonable to assume amplifications can occur at the site, since beneath the bridge there is a layer of between 6 and 12 meters of archaeological fill, with geo-mechanical properties similar to alluvium. The contrast of properties between the fill and the hard bedrock beneath it can readily produce amplification ratios of 10 and higher. In light of these findings, we suggest that the seismic risk map provided by the Israeli Building Code 413 is found wanting, as we show here the local amplifications play a very significant role in structural deformation during shaking in the old city of Jerusalem.

Keywords: *earthquake engineering, numerical modeling, DDA, site response, resonance frequency, rock slopes, toppling, sliding, pseudo-static, paleoseismology, peak ground acceleration, site amplification factor*.

1. Introduction

1.1 General overview

Seismic hazards caused by earthquakes, such as strong ground motions, landslides, rockslides, tsunamis, liquefaction, surface ruptures and more are a societal concern for people and countries all over the world. In an attempt to mitigate life loss and financial damage caused by earthquake hazards, great efforts are invested worldwide in research aimed towards better understanding of earthquake mechanisms, and equally as important, better understanding the response of different structures, both natural and man-made, to ground motions. The ground motions that a particular site would experience during an earthquake are a function of primarily three variables: the source of the seismic waves, the path through which the waves travel, and the specific condition of the site they reach. The research presented in this thesis focuses on the last link in this chain: the site response to remote earthquake tremors, and addresses some of the topics concerning earthquake hazards and structural response to earthquake induced ground motions. The method applied in this research is the numerical, discrete element, Discontinuous Deformation Analysis (DDA) method developed by Dr. Gen-hua Shi at Berkeley in the late 1980's (Shi, 1988; Shi and Goodman, 1988).

Local site effects are well recognized to have a profound influence on surficial ground motions, yet, modeling such a dynamic mechanism has never been attempted in rock engineering context with DDA, or with any other numerical discrete element method that would have been typically applied otherwise to rock engineering problems involving the dynamic interactions of multiple blocks. Once the DDA method is proven applicable for numerical site response analysis, one can perform site response analysis for different, site- specific, complicated geometries, for which no analytical solutions exist. Dynamic site response analysis with the numerical DDA method is discussed in Chapter 3 of this dissertation. The 2D-DDA was proved herein to be applicable for numerical site response analysis, returning resonance frequencies similar to the ones found by the experimental geophysical survey performed in the field, when preliminary calibration of numerical user defined control parameters is performed.

Instability of rock slopes during earthquakes is a major earthquake hazard. When sliding concentrates on a single, infinite plane, rock slopes may be modeled as a single block on an inclined plane. The possible failure modes in this case are: 1) Stable, 2) Sliding, 3) Toppling, and 4) Sliding and Toppling. In Chapter 4 of this dissertation, the classical toppling vs. sliding problem of a single block on an inclined plane is revisited (to be distinguished from the multiple block resting on a stepped base problem that was studied by Goodman and Bray (1976)), but this time with consideration of an additional pseudo-static force, an approach commonly employed in geotechnical earthquake engineering where the entire dynamic earthquake record is replaced by a single static force. An original failure mode chart is derived analytically, and it is found that the mode of failure of a block on an incline subjected to pseudo-static force is a function of three angles, two of which are the friction angle between the block and the slope ϕ, and the block's angle δ, and the third is the angle between the resultant of the block's weight and the pseudo-static force with the vertical direction. The analytical solution is verified and confirmed with both the two-dimensional (2D) and three-dimensional (3D) DDA.

The research of earthquake induced damage to ancient structures, widely observed in Israel, is of great importance, since recorded data of strong earthquakes in the region are scarce, down to non-existing. This research direction belongs, in essence, to the field of paleo-seismology which recently has become to be known as archeo-seismology. Applying sophisticated and robust quantitative tools which originate from numerical analysis in rock mechanics to this young and very important field of science can help constrain, quantitatively, historic earthquake parameters such as the peak ground acceleration (*PGA*) experienced during these earthquakes. Thus the seismic risk associated with a particular region may be better constrained. In Chapter 5 of this dissertation, constraining paleo *PGA* values responsible for mapped damage in a historic Roman bridge situated at one of the most important tourist attractions in the world, the underground tunnels below the Old City of Jerusalem, is demonstrated. The numerical DDA method is utilized to constrain the paleo-*PGA* values through hundreds of simulations, and once these are constrained, some surprising conclusions regarding the amplifications at the site are made, and the time of the damaging earthquake is assessed. We prove that the ancient bridge in the Old City of Jerusalem was damaged by an earthquake while exposed above ground level. The paleo *PGA* causing the damage was high, between 1.5-2 *g*, implying high amplification factors for that region in the Old City of Jerusalem. The candidate earthquakes for causing the damage are the earthquakes reported from 363 and 746 AD (Ben-Menahem, 1991).

1.2 Dissertation outline

This dissertation consists of six chapters, including the introduction.

Chapter 2 is entitled “Research method”. Since all the projects presented in this dissertation share the same research method, the numerical DDA, the numerical approach was assigned a separate chapter, in which the fundamentals of the method are presented and new contributions to the DDA research field made in this study are discussed.

Chapters 3-5 are three different research projects conducted during my Ph.D. studies. Each chapter stands alone, written as a journal paper, and contains all the information required for full comprehension, except for the fundamentals of the DDA as a research method, as these are provided in a separate chapter, and are not repeated in each of those chapters, for brevity.

Chapter 3, entitled “Site response analysis with two-dimensional numerical discontinuous deformation analysis method”, tests the ability of the DDA method to perform numerical site response analysis.

Chapter 4, entitled “A new failure mode chart for toppling and sliding with consideration of earthquake inertia force”, maps the failure modes of a block on an inclined plane subjected to gravity and pseudo-static horizontal force. The mode boundaries, separating the four different modes: stable, sliding, toppling, and sliding+toppling, are derived analytically, and are then verified with the 2D and 3D- DDA codes.

Chapter 5, entitled “Paleo-seismological implications of historic block displacements in the Western Wall Tunnels, the Old City of Jerusalem”, aims to find the paleo *PGA* required for causing observed damage to a single block in a barrel vault in the Western Wall Tunnels, Old City of Jerusalem.

Chapter 6 discusses and summarizes the key findings of the projects above-mentioned.

2. Research method: the Discontinuous Deformation Analysis

The Discontinuous Deformation Analysis (DDA) is the sole research method used in this thesis, therefore it received a separate chapter, in order to refrain from repetition in the different chapters. Section 2.1 reviews the DDA fundamentals, purpose and utilization method, and sections 2.2 – 2.4 present contributions to DDA achieved in this thesis.

2.1 Fundamentals of DDA

2.1.1 Basic concepts of DDA

DDA is an implicit, discrete element method (DEM) proposed by Shi (Shi, 1988, 1993; Shi and Goodman, 1985) to provide a tool useful for investigating the dynamics of blocky rock masses and systems composed of multiple blocks. The two-dimensional DDA (2D-DDA) was proposed first, in the 1980's at UC Berkeley (Shi, 1988, 1993; Shi and Goodman, 1985), and the three- dimensional DDA (3D-DDA) was published later by Shi (2001). In this dissertation both the two-dimensional and the three-dimensional codes are used for numerical simulations. A good review of DDA within the scope of other numerical methods used today to solve problems in rock mechanics and rock engineering is provided by Jing (2003), Jing and Hudson (2002) and Jing and Stephansson (2007). A comprehensive review of 2D-DDA validations and bench-mark tests is provided by MacLaughlin and Doolin (2006).

DDA models a discontinuous material as a system of individually deformable blocks that move independently with minimal amount of interpenetration. The formulation is based on dynamic equilibrium that considers the kinematics of individual blocks as well as friction along the block interfaces. Although belonging to the family of DEMs, DDA closely parallels the finite element method (FEM) and is basically a generalization of it (Shi, 1988). Still, while the formulation of DDA is very similar to the FEM, in the DDA the blocks, or elements, are not restricted to standard shapes as in FEM, and the unknowns are the displacements and deformations of the blocks. These are the result of the accumulation of small time steps. The equilibrium equations are derived by minimizing the total potential energy of the block system. Interpenetration of blocks is minimized by assigning virtual springs at the contacts – when penetration occurs, the springs are shortened, an energy consuming action, therefore introducing numerical penalty due to the principal of minimization of potential energy. The same approach is applied for tension between blocks: in this case the springs are elongated, and therefore there is minimal tension between blocks when the block system attains equilibrium at the end of each time step.

Friction along interfaces is implemented following the Mohr-Coulomb failure criterion. In the two dimensional formulation of DDA each block in the general block system has six degrees of freedom: rigid body translations, rigid body rotation, and the normal and shear strain components. In the three dimensional DDA each block has 12 degrees of freedom: three translations, three rotations, three normal strains and three shear strains (Shi, 2001).

Both the 2D-DDA and 3D-DDA are first order approximations: the blocks are simply deformable, and the stress and strain distribution throughout the block is homogeneous: for each time step the displacement, rotations and strains are calculated at the block centroid. This assumption of constant strain throughout a block can be acceptable in some cases, as in this thesis, where block systems are uniform in shape and size and generally small loading is applied, hence rigid body motion is assumed to be dominant. However, when more heterogeneous block systems are modeled, and especially when modeling stress wave propagation through the modeled block system, a mathematical cover mesh should be used for acquiring the stress distribution within a block, as for example in the Numerical Manifold Method (Shi, 1996b; Shi, 1997).

2.1.2 DDA formulation

2.1.2.1 2D-DDA basic formulation

The discussion below follows a good summary of the governing equations in DDA provided by Ohnishi et al.(2005). The governing equation of the potential energy, Π^{sys}, for large deformations of continuous and discontinuous elastic bodies is given by Hilbert et al.(1994):

$$\Pi^{sys} = \sum_{i=1}^{n} \Pi^{(block)i} = \sum_{i=1}^{n} \left(\Pi^{i} + \sum_{j=1}^{m} \Pi_{PL}^{i,j} \right) \qquad \text{Equation 2-1}$$

where Π^i is the potential energy of the continuum part and $\sum_{j=1}^{m} \Pi_{PL}^{i,j}$ is the potential energy of the contact between blocks. The latter term is evaluated by the minimum potential energy theory, by using a penalty as follows:

$$\Pi_{PL}^{i,j} = \frac{1}{2} k_N \left[\left(d^j - d^i \right) \cdot \hat{n} \right]^2 - \frac{1}{2} k_T \left[d_T^j - d_T^i \right]^2 \quad \text{Equation 2-2}$$

where k_N is the penalty coefficient in the normal direction (referred to as *g0* later in the text), k_T is the penalty coefficient in the shear direction, $\left(d^j - d^i \right) \cdot \hat{n}$ is the amount of penetration between blocks in the normal direction, and d_T is the amount of slip in the shear direction and $\hat{n}$ is the unit vector of the contact plane.

In the DDA method, the equations of motion, formulated from Eq. 2-1 and based on Hamilton's principle, can be written as follows:

$$\mathbf{M}\ddot{\mathbf{d}} + \mathbf{C}\dot{\mathbf{d}} + \mathbf{K}\mathbf{d} = \mathbf{f} \quad \text{Equation 2-3}$$

where **M**, **C**, and **K** are mass matrix, viscosity matrix, and stiffness matrix, respectively, and **d** and **f** are the displacement unknowns and force vectors.

The viscosity matrix **C** in Eq. 2-3 can be re-written in terms of viscosity η and mass matrix **M**:

$$\mathbf{C} = \eta \mathbf{M} \quad \text{Equation 2-4}$$

Eq. 2-3 is solved by Newmark's β and γ method (Hilbert et al., 1994) with $\beta = 0.5$ and $\gamma = 1.0$, and the algebraic equation for displacements is solved for each time increment by

$$\hat{\mathbf{K}} \Delta \mathbf{d} = \hat{\mathbf{f}} \quad \text{Equation 2-5}$$

where $\hat{\mathbf{K}}$, defined as the equivalent global stiffness matrix, is:

$$\hat{\mathbf{K}} = \frac{2}{\Delta t^2} \mathbf{M} + \frac{2\eta}{\Delta t} \mathbf{M} + \frac{\rho^c}{\rho^0} \left[\mathbf{K}_e + \mathbf{K}_s \right] \quad \text{Equation 2-6}$$

and $\hat{\mathbf{f}}$ is defined as:

$$\hat{\mathbf{f}} = \frac{2}{\Delta t} \mathbf{M} \cdot \dot{\mathbf{d}} + \left(\Delta \mathbf{f} - \sum \int \sigma dv \right) - \mathbf{M} \alpha(t) \quad \text{Equation 2-7}$$

$\Delta\mathbf{d}$ is the incremental displacement, $\mathbf{K_e}$ the stiffness matrix of linear term, $\mathbf{K_s}$ initial stress matrix caused by rigid rotation and $\alpha(t)$ is time history of earthquake acceleration.

The plane displacement *(u,v)* of any point *(x,y)* in block *i* can be represented by six displacement variables which yield the displacement matrix of the block, $\mathbf{d}_i$,

$$\mathbf{d}_i = \{u_0 \;\; v_0 \;\; r_0 \;\; \varepsilon_x \;\; \varepsilon_y \;\; \gamma_{xy}\}_i^T, \quad (i = 1,2,\cdots,n) \qquad \text{Equation 2-8}$$

where the first three are the rigid body displacements and rotation (at the centroid), and the last three are normal and shear strains in the block. As shown by Shi (1993), the complete first order approximation of displacements at any point (x, y) take the following form:

$$\begin{Bmatrix} u_x \\ u_y \end{Bmatrix}_i = \mathbf{T}_i\mathbf{d}_i\,, \quad (i = 1,2,\cdots,n) \qquad \text{Equation 2-9}$$

where:

$$\mathbf{T}_i = \begin{bmatrix} 1 & 0 & -(y-y_0) & (x-x_0) & 0 & \dfrac{(y-y_0)}{2} \\ 0 & 1 & (x-x_0) & 0 & (y-y_0) & \dfrac{(x-x_0)}{2} \end{bmatrix}_i \qquad \text{Equation 2-10}$$

Assuming the velocity at the beginning of the time step, which can be obtained from the previous time step, is $\dot{\mathbf{d}}_\mathbf{0}$**,** and that the time interval of a single time step is Δt, then:

$$\ddot{\mathbf{d}} = \frac{2}{\Delta t^2}\left(\mathbf{d} - \Delta t\dot{\mathbf{d}}_\mathbf{0}\right)$$
$$\dot{\mathbf{d}} = \frac{2}{\Delta t}\mathbf{d} - \dot{\mathbf{d}}_\mathbf{0} \qquad \text{Equation 2-11}$$

By substituting Eq. 2-11 into Eq. 2-3 the simultaneous equilibrium equations can be rewritten as:

$$\hat{\mathbf{K}}\mathbf{d} = \hat{\mathbf{f}} \qquad \text{Equation 2-12}$$

Eq. 2-12 can be written in a sub-matrix form as follows:

$$\begin{bmatrix} \hat{\mathbf{K}}_{11} & \hat{\mathbf{K}}_{12} & \hat{\mathbf{K}}_{13} & \cdots & \hat{\mathbf{K}}_{1n} \\ \hat{\mathbf{K}}_{21} & \hat{\mathbf{K}}_{22} & \hat{\mathbf{K}}_{23} & \cdots & \hat{\mathbf{K}}_{2n} \\ \hat{\mathbf{K}}_{31} & \hat{\mathbf{K}}_{32} & \hat{\mathbf{K}}_{33} & \cdots & \hat{\mathbf{K}}_{3n} \\ \vdots & \vdots & \vdots & \ddots & \vdots \\ \hat{\mathbf{K}}_{n1} & \hat{\mathbf{K}}_{n2} & \hat{\mathbf{K}}_{n3} & \cdots & \hat{\mathbf{K}}_{nn} \end{bmatrix} \begin{Bmatrix} \mathbf{d}_1 \\ \mathbf{d}_2 \\ \mathbf{d}_3 \\ \vdots \\ \mathbf{d}_n \end{Bmatrix} = \begin{Bmatrix} \hat{\mathbf{f}}_1 \\ \hat{\mathbf{f}}_2 \\ \hat{\mathbf{f}}_3 \\ \vdots \\ \hat{\mathbf{f}}_n \end{Bmatrix}$$ Equation 2-13

where $\hat{\mathbf{K}}_{ij}(i, j = 1,2,\cdots,n)$ are 6×6 sub-matrices; $\mathbf{d}_i$ and $\hat{\mathbf{f}}_i(i = 1,2,\cdots,n)$ are 6×1 sub-matrices corresponding to block *i*. Each coefficient K_{ij} is defined by the contacts between blocks *i* and *j*, and where $i = j$ K_{ii} is defined by the material properties of block *i*.

The equilibrium equations are derived by minimizing the total potential energy *Π* produced by the forces and stresses. The i^{th} row of Eq. 2-13 consists of six linear equations:

$$\frac{\partial \Pi}{\partial d_{ri}} = 0, \quad r = 1,\ldots,6$$ Equation 2-14

where d_{ri} represents the deformation variables of block *i*. The total potential energy *Π* is the summation over all the potential energy sources.

2.1.2.2 3D-DDA basic formulation

The displacement matrix *[D]* of the 3D-DDA is:

$$[D]^T = \begin{pmatrix} u_c & v_c & w_c & r_x & r_y & r_z & \varepsilon_x & \varepsilon_y & \varepsilon_z & \gamma_{yz} & \gamma_{xz} & \gamma_{xy} \end{pmatrix}$$
Equation 2-15

where $\begin{pmatrix} x_c \\ y_c \\ z_c \end{pmatrix}$ is the centroid of the block, and $\begin{pmatrix} u_c \\ v_c \\ w_c \end{pmatrix}$ are its displacements.

For the i^{th} block, it can be written:

$$\begin{pmatrix} u \\ v \\ w \end{pmatrix} = [T_i(x, y, z)][D_i]$$ Equation 2-16

where $[T_i(x, y, z)]$ is defined as:

$$[T(x,y,z)] = \begin{pmatrix} 1 & 0 & 0 & 0 & (z-z_c) & -(y-y_c) & (x-x_c) & 0 & 0 & 0 & (z-z_c)/2 & (y-y_c)/2 \\ 0 & 1 & 0 & -(z-z_c) & 0 & (x-x_c) & 0 & (y-y_c) & 0 & (z-z_c)/2 & 0 & (x-x_c)/2 \\ 0 & 0 & 1 & (y-y_c) & -(x-x_c) & 0 & 0 & 0 & (z-z_c) & (y-y_c)/2 & (x-x_c)/2 & 0 \end{pmatrix}$$

Equation 2-17

The coefficient matrix of the obtained simultaneous equilibrium equations is the same as in the 2D-DDA, Eq. 2.3, only here each element K_{ij} in the coefficient matrix is a 12x12 submatrix, and D_i and F_i are 12x1 submatrices.

Again, the equilibrium equations are derived by minimizing the total potential energy Π, and the i^{th} row of Eq. 2.3 consists of 12 linear equations:

$$\frac{\partial \Pi}{\partial d_{ri}} = 0, \quad r = 1, \ldots, 12$$

Equation 2-18

2.1.3 User defined numerical control parameters in DDA

The DDA code used in this research is an advanced version of the original code developed by Shi (1993), licensed for the specific purposes of this research by the developer, Dr. Gen-hua Shi. Several user defined numerical parameters are required for input in DDA:

dd – the dynamic control parameter. For a fully static analysis, where the velocity is zeroed at the beginning of each time step, *dd* = 0 is used. For a fully dynamic analysis, where the velocity at the beginning of a time step is inherited from the velocity at the end of the previous time step, *dd* = 1 is selected. Any number between 0 and 1 corresponds to a measure of kinetic (numerical) "damping" in the analysis, i.e. *dd* = 0.97 means 3% velocity decrease from the end of a time step to the beginning of the next. This parameter can be used for inserting damping effects, as viscose damping is not implemented in the original code of the DDA.

g0 – the contact spring stiffness or the penalty, also denoted as "*k*"– the stiffness of the normal virtual springs assigned to the contacts, in order to minimize penetration and tension. The *g0* value must be very carefully selected, as it very much affects the results of the analysis. If possible, it should be selected by comparing the DDA results to an existing analytical solution, and performing iterations until a satisfying agreement is obtained. A recommendation made by Shi (1996a) in the DDA user manual is to use a value of $k = E*L$, where E is Young's modulus and L is the average diameter of block.

g1 – time step interval, also denoted as Δ. This number should be small enough so as to guarantee infinitesimal displacements at each time step. Careful and educated selection of the *g1* value will ensure both high efficiency and high accuracy of the numerical solution. As mentioned in chapter 3 of the dissertation, the time step interval may also serve as a damping mechanism, as larger Δ values enhance the algorithmic damping which is inherit to DDA.

g2 – assumed maximum displacement per time step ratio: a dimensionless quantity related to the size of the model. It is used to find possible contacts between blocks, and should be small enough to ensure infinitesimal displacement at each time step, and to ensure the convergence of the solution.

2.2 3D-DDA verification

The 2D-DDA has been verified by many researchers, including the author (Yagoda-Biran and Hatzor, 2010). A review of the history of 2D-DDA verification is presented by MacLaughlin and Doolin (2006). The 3D-DDA however has not been verified as extensively as the 2D-DDA, and therefore verification studies for simple cases, for which an analytical or semi-analytical solution exists, are performed in this thesis, in many cases for the first time.

2.2.1 Block sliding on an inclined plane

The problem of a block sliding on an incline has been verified for the 2D-DDA, and is addressed in detail in Chapter 4. This is a very attractive problem for verification studies, because of its simplicity, both analytical and numerical. In this subsection the 3D-DDA is verified with an analytical solution for the block on an incline problem.

The 3D-DDA mesh is constructed of a triangular prism base block, serving as the incline, with height of 10 m, inclination angle of α = 45^{o} and depth of 5 meters. The sliding block is a box, with dimensions 1 m*1 m*0.5 m (see Figure 2.1). The base block is fixed in space by 7 fixed points, and cannot move, and the sliding block is loaded by two loading points, for the third step of the verification study, as explained below.

The verification study of the block on an incline was performed in three steps: first the response of the block when subjected to gravity, starting at rest, was examined in section 2.2.1.1, then the block was given initial horizontal velocity in section 2.2.1.2, and finally the block was subjected to one- dimensional horizontal sinusoidal acceleration, in section 2.2.1.3.

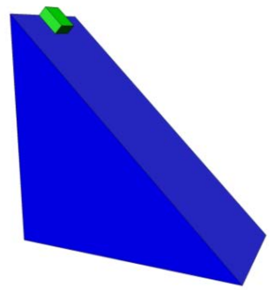

Figure 2.1. The 3-D model used for the 3D-DDA validation of a block on an inclined plane.

2.2.1.1 Downslope displacements under gravitational loading

The first step of the verification study was subjecting the sliding block to gravity alone. The block downslope displacements were compared with the displacements calculated by an analytical solution for the problem, presented below.

The forces acting on the block on an incline are the gravitational force, the normal from the incline and the frictional force. The downslope destabilizing force F_d can be expressed as

$$F_d = mg\sin\alpha \qquad \text{Equation 2-19}$$

where m is the block's mass and α is the inclination angle of the base block. The stabilizing force, F_s, i.e. the frictional force, can be expressed as

$$F_s = mg\cos\alpha\tan\phi \qquad \text{Equation 2-20}$$

where ϕ is the friction angle of the interface between the base block and the sliding block. Therefore the downslope acceleration, $\ddot{d}(t)$, which is the resultant force acting on the block in the downslope direction divided by the mass, is

$$\ddot{d} = g\sin\alpha - g\cos\alpha\tan\phi\,. \qquad \text{Equation 2-21}$$

Double integration over time of the acceleration term in Eq. 2.11 will give the displacement *d(t)* (with zero initial velocity and displacement)

$$d(t) = \frac{1}{2}\ddot{d}t^2 = \frac{1}{2}g(\sin\alpha - \cos\alpha\tan\phi)t^2$$ Equation 2-22

Table 2-1 lists the numerical and physical parameters used in the first step of the verification study.

Table 2-1. Numerical and physical parameters used in the first step of the verification study

Parameter	**value**
dd – dynamic parameter	1
g0 – normal contact spring stiffness	$4*10^8$ N/m
g1 – time step interval	0.001 sec
g2 – maximum displacement ratio	0.001
density	2700 kg/m^3
Young's modulus	40 GPa
Poisson's ratio	0.18

The downslope displacement history was compared for three values of friction angle: 10, 20 and 30° (remembering the inclination angle of the slope is 45°). In Figure 2.2a the results of the first step of the verification study are presented. Note the agreement between the analytical and numerical solutions. In Figure 2.2b the relative numerical error, defined as $error = \frac{disp_{analy} - disp_{numer}}{disp_{analy}} \times 100\%$, is presented. After 0.2 sec the numerical error drops to below 1%, demonstrating the excellent agreement between the two solutions.

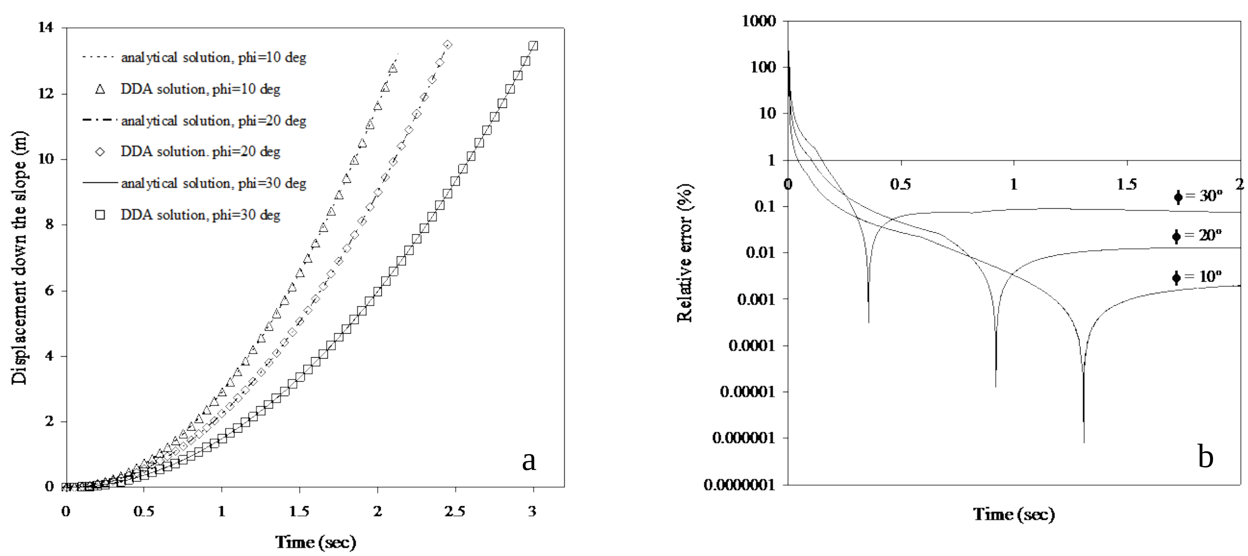

Figure 2.2. a) Downslope displacement histories of a block on an inclined plane subjected to gravity alone. Legend: curves - analytical solution, symbols – DDA solution. b) The relative numerical error.

2.2.1.2 Downslope displacements under gravitational loading and initial velocity

The next step of the verification study is applying initial velocity $\dot{d}_0$ to the sliding block, and comparing the downslope displacements of the block to the ones computed by the analytical solution. Similar to the analytical solution presented in step one, double integration over time of the acceleration term yields:

$$d(t) = \frac{1}{2}\ddot{d}t^2 + \dot{d}_0 t = \frac{1}{2}g(\sin\alpha - \cos\alpha\tan\phi)t^2 + \dot{d}_0 t \qquad \text{Equation 2-23}$$

In this verification step the numerical and physical parameters remain identical to the values presented in Table 2-1, except for the time step interval that was set to 0.0001 sec.

The initial velocities were applied in the horizontal direction at three different values: 0.01 m/sec, 0.1 m/sec and 1 m/sec. Results for downslope displacement history are presented in Figure 2.3a. The agreement between the analytical and the numerical solutions is good for all three different velocities, as can be verified by the relative numerical error plotted in Figure 2.3b : less than 1% after 0.5 sec of the analysis.

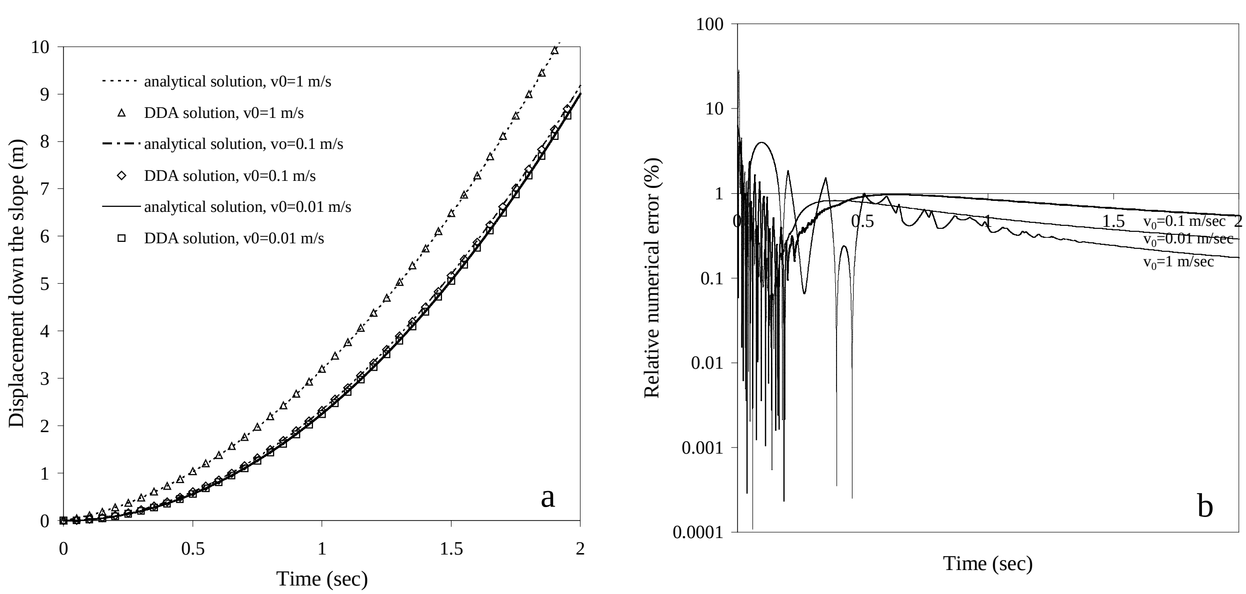

Figure 2.3. a) Downslope displacement histories of a block on an inclined plane subjected to gravity and different initial velocities. Legend: curves - analytical solution, symbols - DDA solution. b) The relative numerical error.

2.2.1.3 Downslope displacements under gravitational and one-dimensional sinusoidal acceleration

The third step of the verification study is comparing the downslope displacements of the block computed by an analytical solution, with those obtained by the 3D-DDA, where the sliding block is subjected to a one-dimensional horizontal sinusoidal acceleration in the form of $\ddot{d}(t) = A\sin(\omega t)$, in addition to the constant gravitational acceleration.

The analytical solution is as follows: as the friction angle of the interface between the slope and the sliding block is set to ϕ = 50° in this verification step, higher than the inclination angle α = 45°, block sliding will initiate only when the acceleration has reached the value of the yield acceleration and beyond. This type of analysis is called Newmark type analysis (Newmark, 1965) although it was developed independently by Goodman and Seed (1966) in their classic paper on earthquake induced displacements in sand embankments. It can be shown (Goodman and Seed, 1966; Newmark, 1965) that in the case of a block on an inclined plane, the yield acceleration is $\ddot{d}_{yield} = \tan(\phi - \alpha)g$. Once the sinusoidal input acceleration has reached or exceeded $\ddot{d}_{yield}$, at time t_1, the block begins to gain downslope velocity and displacement. When the sinusoidal input acceleration drops below the value of $\ddot{d}_{yield}$, the velocity decreases, as the block is restrained by the frictional resistance, until it reaches zero and the block is at rest. When the sinusoidal input acceleration exceeds $\ddot{d}_{yield}$ again at time t_2, motion will commence and so on, see Figure 2.4.

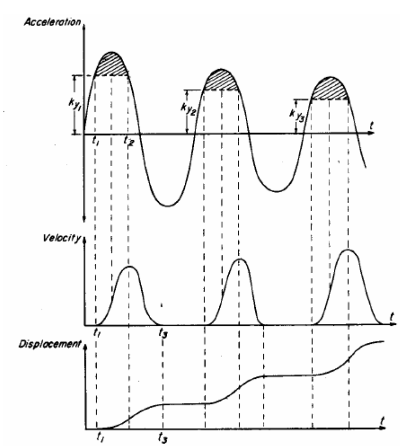

Figure 2.4. Newmark type analysis. Shaded areas are the times at which acceleration exceeds $\ddot{d}_{yield}$. From Goodman and Seed (1966).

To obtain the Newmark displacement, double integration over time of the downslope acceleration $\ddot{d}(t)$ must be performed, where:

$$\ddot{d}(t) = [A\sin(\omega t)\cos\alpha + g\sin\alpha] - \tan\phi[g\cos\alpha - A\sin(\omega t)\sin\alpha] \qquad \text{Equation 2-24}$$

and A and ω are the input acceleration amplitude and the input angular frequency, respectively. Double integration of Equation 2.14 yields (after Kamai and Hatzor, 2008):

$$d(t) = g\left[(\sin\alpha - \cos\alpha\tan\phi)\left(\tfrac{1}{2}t^2 - \theta t + \tfrac{1}{2}\theta^2\right)\right] + \frac{A}{\omega^2}\left[(\cos\alpha + \sin\alpha\tan\phi)(\omega\cos(\omega\theta)(t-\theta) - \sin(\omega t) + \sin(\omega\theta))\right] \qquad \text{Equation 2-25}$$

where θ is the time when $\ddot{d}_{yield}$ is exceeded and downslope displacement initiates. Since block displacement initiates only once $\ddot{d}_{yield}$ is reached or exceeded, double integration of the downslope acceleration is performed as long as the downslope acceleration $> \ddot{d}_{yield}$, or the velocity > 0. The amplitude and frequency used for the input acceleration are 2 m/sec^2 and 1 Hz, respectively. The numerical and physical parameters are identical to the ones listed in Table 2-1, except for the time step size that was set to 0.0001 sec and the normal contact spring stiffness that was set to $7*10^9$ N/m. As mentioned earlier, friction was set to $\phi = 50^{\circ}$.

In Figure 2.5a the downslope displacement histories calculated by the Newmark analysis and the DDA code are presents. The agreement between the two is good, and can again be expressed in terms of relative error, presented in Figure 2.5b. During most of the analysis the error remains below 3%.

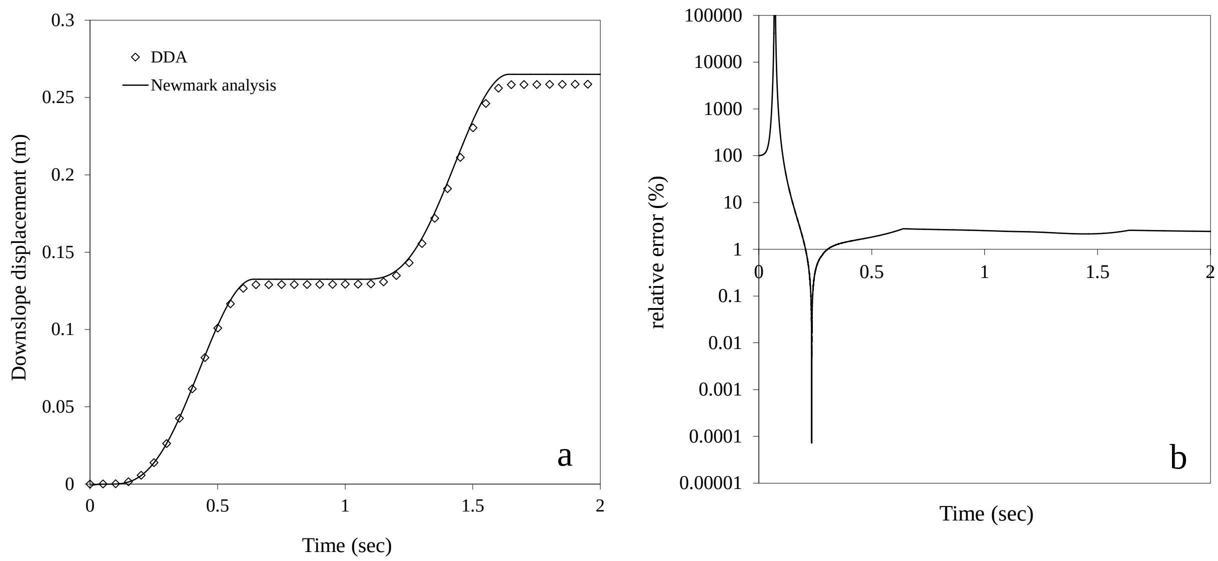

Figure 2.5. a) Downslope displacement histories of a block on an inclined plane subjected to gravity and 1-D sinusoidal input function. Legend: curve - analytical solution, symbols - DDA solution. b) The relative numerical error.

2.2.2 Block response to induced displacements in the foundation

A verification of the case of a responding block to a moving foundation is presented in this section, comparing the 3D-DDA numerical solution to a semi-analytical solution. The verification is based on the one-dimensional verification study performed by Kamai and Hatzor (2008), only here the displacements, velocities and accelerations are 3D vectors.

2.2.2.1 The semi-analytical solution

The model used for the verification study is composed of two blocks (Figure 2.6): a lower block, subjected to time dependent displacements, and an upper block that responds to the displacements of the lower one.

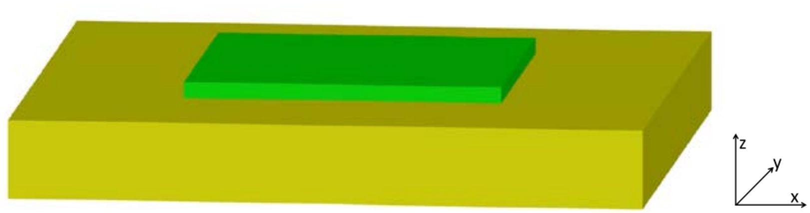

Figure 2.6. The 3D model used in the verification study. The lower yellow block is displaced by the time-dependent displacement vector, and the displacements of the green, upper, responding block are measured.

The dimensions of the blocks and their physical properties are irrelevant for the analytical solution, since it only considers the friction coefficient, as shown below. For the 3D-DDA, though, block dimensions and properties are of importance.

Each of the two blocks, which are denoted from hereon 1 and 2 for the lower and upper blocks, respectively, has time dependent displacements $\bar{d}(t)$, velocities $\dot{\bar{d}}(t)$ and accelerations $\ddot{\bar{d}}(t)$. The displacement induced to block 1, $\bar{d}_1$, is in the form of a cosine function:

$$\bar{d}_1(t) = \bar{A}\left(1 - \cos\left(2\pi\bar{f}t\right)\right) \qquad \text{Equation 2-26}$$

where $\bar{A}$ and $\bar{f}$ are the amplitude and frequency of motion, respectively.

The forces acting on block 2 are its weight, *mg*, the normal from block 1 $N = m_2g$ and the frictional force between the two blocks, $\mu * m_2 g$, where μ is the friction coefficient. Newton's second law of motion yields that the acceleration of block 2 is $\left|\ddot{\bar{d}}_2\right| = \mu * g$.

Following Kamai and Hatzor (2008), the direction of the frictional force, and therefore of $\ddot{\bar{d}}_2$, is determined by the **direction** of the relative velocity between the two blocks, $\dot{\bar{d}}* \equiv \dot{\bar{d}}_1 - \dot{\bar{d}}_2$, defined by the unit vector of the relative velocity, $\hat{\dot{d}}*$. When $\left|\dot{\bar{d}}*\right| = 0$, the acceleration of block 2 ($\ddot{\bar{d}}_2$) is determined by the acceleration of block 1 ($\ddot{\bar{d}}_1$). When the acceleration of block 1 exceeds the yield acceleration $\mu * g$, over which block 2 no longer moves in harmony with block 1, the frictional force direction is determined by the direction of $\hat{\dot{d}}^*$, but the magnitude of $\ddot{\bar{d}}_2$ is equal to $\mu * g$. This is summarized with a few simple conditions:

If $\left|\dot{\bar{d}}*\right| = 0$ …………….. and $\left|\ddot{\bar{d}}_1\right| \le \mu * g$ ……………… then $\ddot{\bar{d}}_2 = \ddot{\bar{d}}_1$

and $\left|\ddot{\bar{d}}_1\right| > \mu * g$ ………………. then $\ddot{\bar{d}}_2 = (\mu * g)\cdot \hat{\ddot{d}}_1$

If $\left|\dot{\bar{d}}*\right| \ne 0$ ……………………………………...………………….. then $\ddot{\bar{d}}_2 = (\mu * g)\cdot \hat{\dot{d}}*$

This set of conditions and inequalities was applied using a MATLAB script, with a time step of 0.0001 sec. Since the time step size has a significant effect on the results of the “analytical” solution, it is actually a semi-analytical solution.

2.2.2.2 The numerical model

The actual model used for the 3D-DDA is shown in Figure 2.6. The dimensions of block 1 are 4 m*4 m*0.5 m, and the dimensions of block 2 are 2 m*2 m*0.1 m. Block 2 was designed to be very flat, so as to avoid rotations during motion. The physical and numerical control parameters used in the verification analyses are listed in Table 2-2.

Table 2-2. Physical and numerical control parameters used in the verification study of the responding block

Parameter	**Value**
dd - dynamic parameter	1 (fully dynamic)
g0 - normal contact spring stiffness	$1*10^9$ N/m
g1 - time step size	0.0001 sec
g2 - maximum displacement ratio	0.001
density	2250 kg/m^3
Young’s modulus	17 GPa
Poisson’s ratio	0.22

All numerical simulations lasted seven seconds of real time, where in the first two seconds no displacements were applied, allowing for gravity "turn-on" and settlement of the springs.

2.2.2.3 Comparison under one direction of induced motion

The first step was inducing displacements to block 1 in the *x*-direction (see Figure 2.6) only, similar to the work reported by Kamai and Hatzor (2008), and comparing the 3D-DDA results to the semi-analytical solution. This was done for three different cases:

1) Constant amplitude (A) and friction (μ), and changing frequency (f), of which results are presented in Figure 2.7.
2) Constant f and μ, and changing A, results presented in Figure 2.8.
3) Constant f and A, and changing μ, results presented in Figure 2.9.

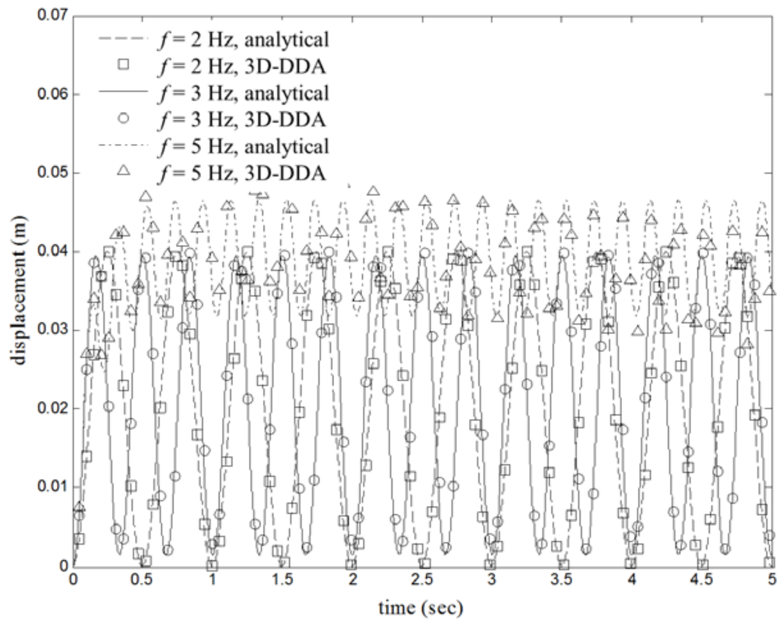

Figure 2.7. Comparison between the analytical solution (curves) and 3D-DDA solution (symbols). Amplitude of A = 0.02 m for the input motion and a friction coefficient of 0.6 remained unchanged, while input motion frequency changed. Notice the excellent agreement between the two solutions for frequencies of 2 and 3 Hz, while the solution for 5 Hz shows some deviations.

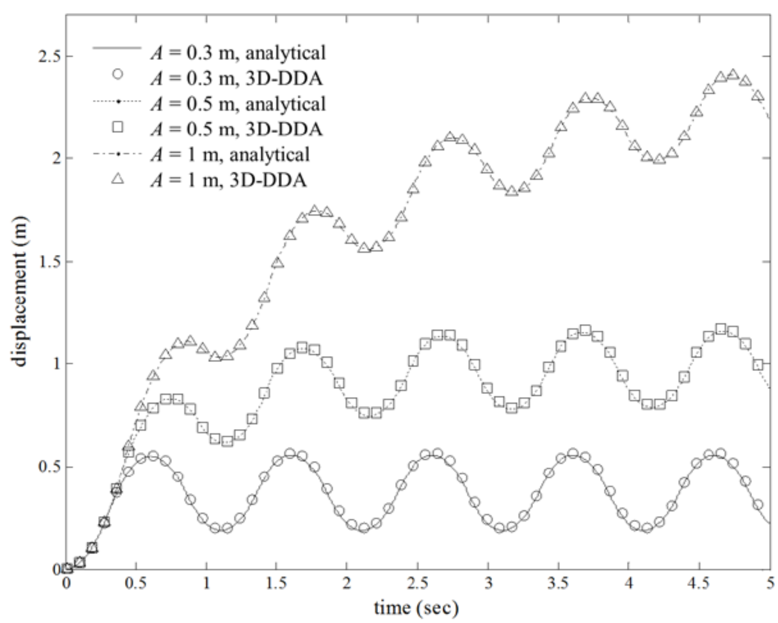

Figure 2.8. Comparison between the analytical solution (curves) and 3D-DDA solution (symbols). Frequency of 1 Hz for the input motion and a friction coefficient of 0.6 remained unchanged, while input motion amplitude changed. Notice the excellent agreement between the two solutions.

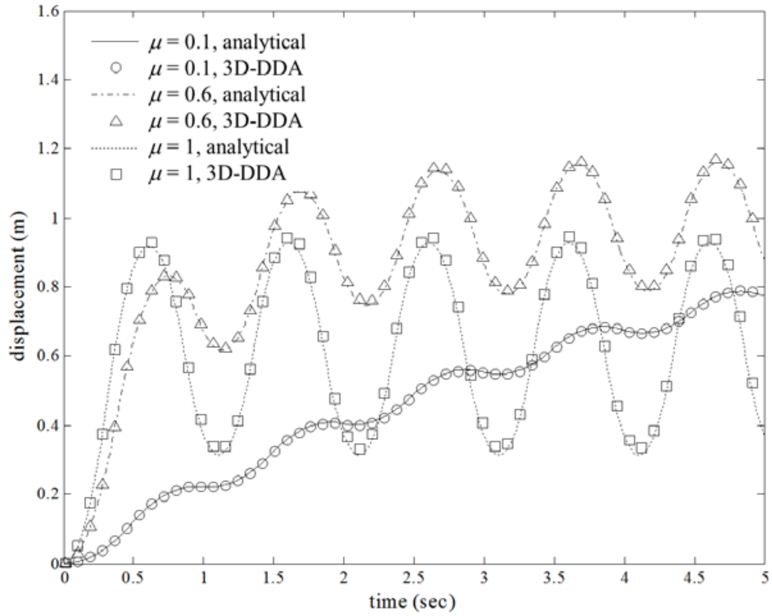

Figure 2.9. Comparison between the analytical solution (curves) and 3D-DDA solution (symbols). Frequency of 1 Hz and amplitude of 0.5 m for the input motion remained unchanged, while the friction coefficient changed. Notice the excellent agreement between the two solutions.

As can be observed from Figures 2.7-2.9, the 3D-DDA is in good agreement with the analytical solution when responding to one- dimensional displacement, except when input frequency is relatively high, as in the case where $f = 5$ Hz (Figure 2.7).

2.2.2.4 Comparison under two directions of induced motion

In the second step of the verification study, displacements were induced to the lower block in the *x* and *y* directions (see Figure 2.6), each with different amplitude and frequency. Results are presented in Figure 2.10 and 2.11. Figure 2.10 shows the **resultant** displacement vs. time, while Figure 2.11 is a 3D plot of the *x* and *y* displacements vs. time, presented as the vertical axis.

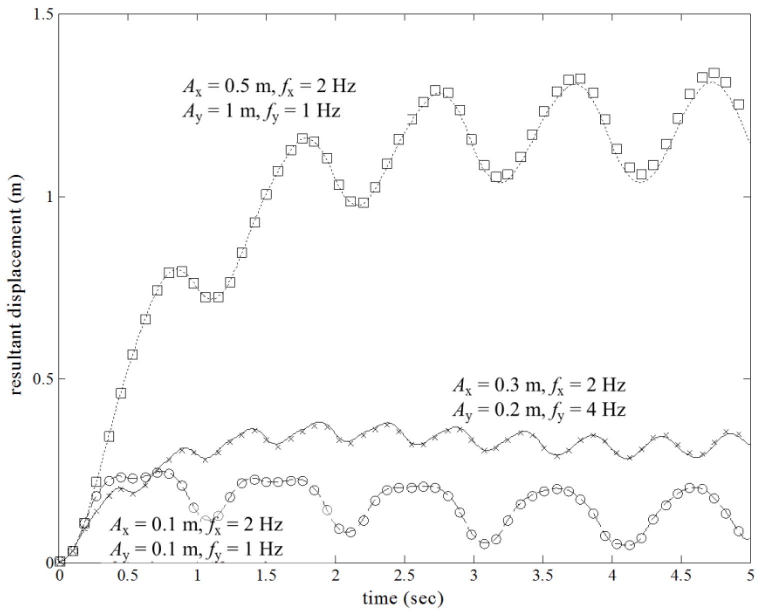

Figure 2.10. Comparison between analytical (curves) and 3D-DDA (symbols) solutions. Each set of curves and symbols corresponds to a different set of amplitude and frequency for the input displacements, noted beside the data. Notice the excellent agreement between the two solutions.

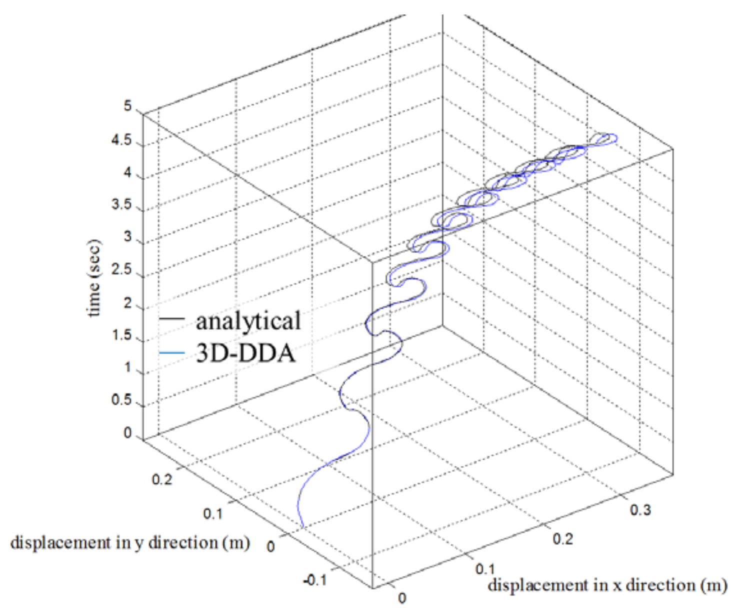

Figure 2.11. Comparison between analytical (black curve) and 3D-DDA (blue curve) solutions. This analysis is for x amplitude and frequency of 0.3m and 2 Hz and y amplitude and frequency of 0.2m and 4 Hz, respectively. Notice the good agreement between the two solutions that decreases with analysis time.

2.2.2.5 Comparison under three directions of induced motion

The third verification step was subjecting block 1 to sinusoidal displacements in all three directions: *x*, *y* and *z*. Adding sinusoidal displacement in the *z* direction affects the response of block 2 in the way that it changes the normal force between the two blocks, and therefore the frictional force between them. This in turn changes the acceleration of block 2, $\ddot{\bar{d}}_2$, and yields a different displacement time history. Applying time-dependent displacements in the *z* direction is actually equivalent to time-dependent changes in *g*: when block 1 has positive *z* acceleration ($\ddot{d}_1\hat{k} > 0$), it is added to *g*. When $\ddot{d}_1\hat{k}$ is negative, it is subtracted from *g*. The analytical solution in this case assumes no other effect of the vertical displacement of block 1 on the horizontal displacement of block 2. The induced displacement function is:

$$\bar{d}_1(t) = 0.1(1-\cos(2\pi 2t))\cdot\hat{i} + 0.1(1-\cos(2\pi 4t))\cdot\hat{j} + 0.1(1-\cos(2\pi t))\cdot\hat{k} \qquad \text{Equation 2-27}$$

Figures 2.12 and 2.13 present results of the verification study with three components of induced displacements. Figure 2.12 presents the resultant horizontal (*x-y* plane) displacement vs. time, for different values of the *k* - normal contact spring stiffness. The black heavy curve is the analytical solution, and the light colorful curves are the 3D-DDA numerical solutions for different values of *k*. The range of stiffness that best fits the analytical solution is between $1*10^7$ and $1*10^9$ N/m, with stiffness of $k = 1*10^7$ N/m, or 0.0003 *E*L*, being the optimal selection, where *E* is the Young's modulus of the block and *L* is the length of the line across which the contact springs are attached. When considering 3D-DDA, it might be more relevant to compare *k* to *E*A*, where *A* is the area across which the contact springs are attached. In this case, $k = 1*10^7$ is ~0.0001 *E*A*, not much different from *E*L*. Figure 2.13 demonstrates this with the relative numerical error, defined in section 2.2.1.1. Note that for the results obtained with $k = 1*10^7$ N/m, the relative error stays below 3% for the entire analysis, and the error is well below 10% for $k = 1*10^8$ and $1*10^9$ N/m as well. This implies that for this case study, the optimal value for normal contact spring stiffness should be between 2 and 4 orders of magnitude less than *E*L*, the value recommended by Shi in his user manual (Shi, 1996a) for 2D-DDA.

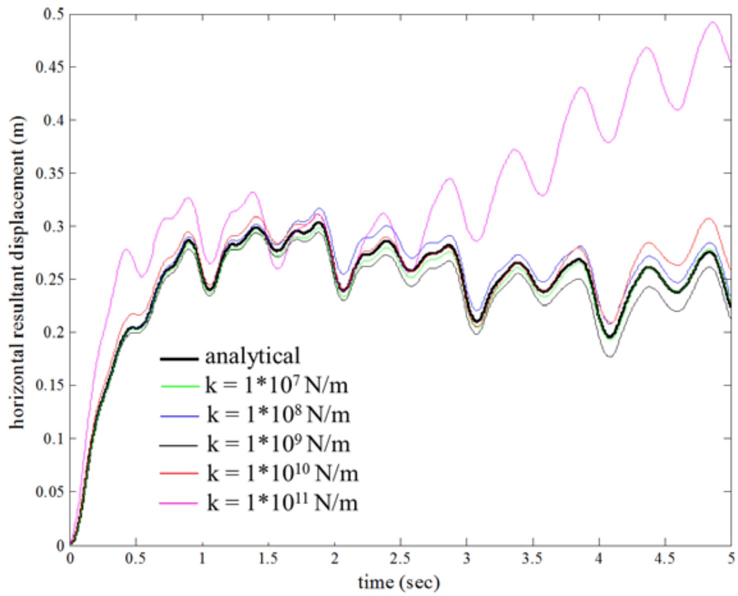

Figure 2.12. Comparison between analytical (black heavy curve) and 3D-DDA (light colorful curves) solutions. The best fit is obtained with contact spring stiffness of k = 1*10^7 N/m, but the overall trend of the analytical solution is maintained for all values of stiffness.

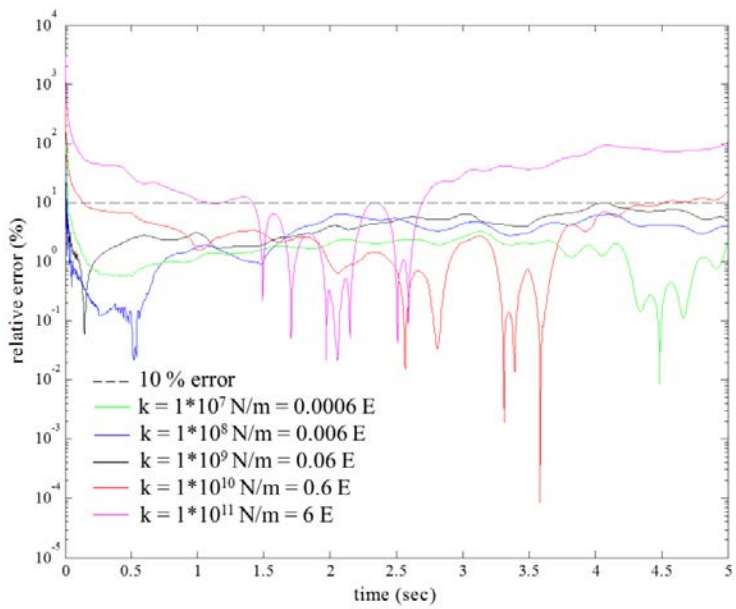

Figure 2.13. Relative numerical error for the different solutions presented in Figure 2.12. Note the black dashed line, indicating error of 10%. The green curve, representing contact spring stiffness of 1*10^7 N/m, remains below 3% error the entire time span of the analysis, and is the best fit for this case.

2.2.3 3D-DDA limitations

Sections 2.1.2.1 and 2.2.2 proved that the 3D-DDA provides accurate displacements, compared with analytical solutions, and therefore is capable of modeling dynamic problems with block systems composed of several blocks. However, many trials performed during my research towards this thesis prove that the current version of the 3D-DDA code is incapable of dealing with multi-block systems for realistic dynamic simulations, and many numerical problems occur when trying to run forward dynamic analyses of complicated multi-block systems. An example for one case is presented below.

An attempt was made to model a masonry structure (see Figure 2.14a) from the city of L'Aquila, Italy that was severely damaged by an earthquake on April 2009. The goal was to model the masonry structure before the damage in 3D-DDA, subject it to earthquake accelerations recorded during that earthquake, and obtain damage similar to that observed in the field.

a  b 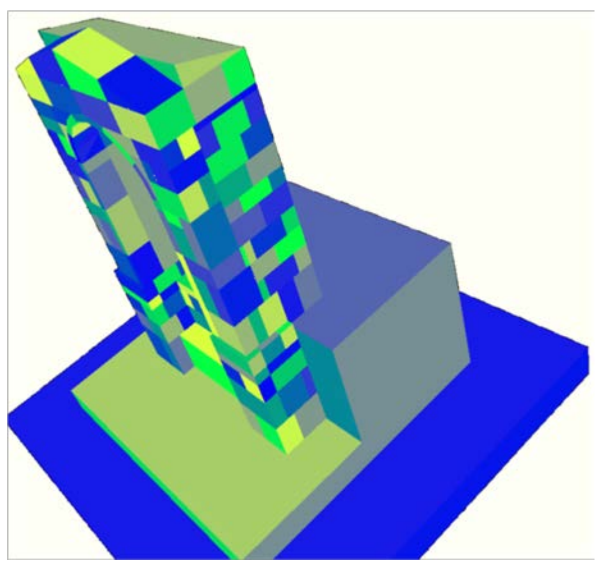

Figure 2.14. a) The masonry structure selected for 3D-DDA modeling in the city of L'Aquila, Italy. b) The 3D-DDA model.

The model was constructed in the 3D-DDA block cutting code 'tc' with the procedure described in section 2.3.2, and consisted of 197 blocks. Forward analyses of this model would converge only with dynamic parameter value of *dd* = 0.97 or less and a time step size no larger than 0.00001 sec, probably due the large number of blocks, and therefore contacts. Such a combination of kinetic damping and time step size leads to restrained displacements, as presented in section 2.4.1, not to mention the very long CPU time required to complete the analysis. In this case study, where displacements are the desirable output, these limitations of the current version of the 3D-DDA code are not tolerable. Therefore, from here on in this dissertation when multi-block systems are modeled, the 2D-DDA code is utilized, with clearly stated and admitted simplifying assumptions regarding boundary conditions.

2.3 From CAD to DDA – easy mesh construction using AutoCAD® software

2.3.1 Motivation

Modeling three dimensional multi-block structures in 3D-DDA is an elaborate and challenging task. The block cutting code in 3D-DDA, i.e. the ‘tc’ code, does not have a graphic interface, and does not accept three- dimensional blocks as input, but rather two- dimensional triangles, of which the blocks are built. For example, in order to build a rectangular face of a box, two triangles will be required, with three vertices in each. Therefore, to form a simple box, one needs to enter the vertices for 12 triangles. This becomes rather complicated if one wishes to model complex structures of a few tens of blocks and more. This difficulty calls for an easier modeling technique, which was developed during this research, and is described here. This technique was originally developed for 3D-DDA modeling, as it is more complex than the 2D-DDA modeling, but can be used with some modifications, as will be described, for 2D-DDA modeling as well. It is important to state that this procedure is intended for modeling discrete blocks, such as in masonry structures or discrete blocks formed in nature, and not rock masses, that form by intersections of systematic joint sets.

2.3.2 Modeling with CAD in 3D-DDA

The steps for constructing a mesh in the 3D-DDA using CAD software are described below. The procedure is demonstrated for a single cubic block sized 3 m*3 m*3 m:

1) Sketch the model in a computer aided design (CAD) software (Figure 2.15). CAD software is designed just for that: modeling structures. It uses a graphic interface and is usually

user friendly. Here the AutoCAD® software by Autodesk® (Autodesk, 2011) was used. The definitions and commands will therefore be those used in AutoCAD® software.

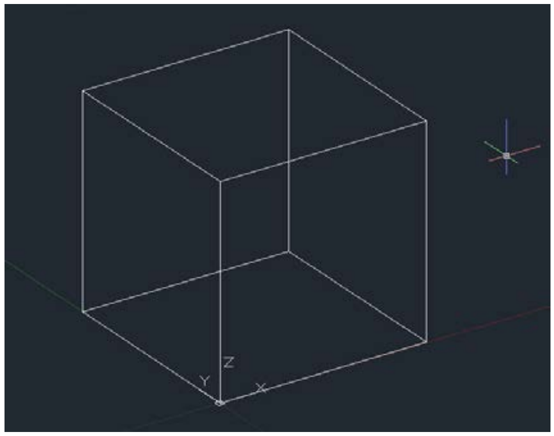

Figure 2.15. The modeled cube in AutoCAD.

2) Important note: AutoCAD® software has an entity named “block”, so in order to distinguish between the AutoCAD® block and the modeled block, the modeled block will be referred to here as ‘cube’. Insert an attribute block in each vertex of the cube (Figure 2.16). Each vertex should receive a number as an attribute. The numbers must be consecutive, starting from one (in order for the MATLAB code to run properly later). If you intend to use special points as well (fixed, loading and measurement points), insert attribute blocks at their locations as well, and number them consecutive to the vertices. In this example a measurement point is inserted to the block’s centroid.

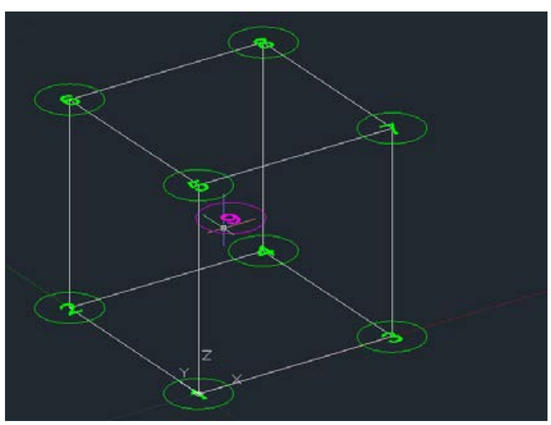

Figure 2.16. The modeled cube. The vertices are marked by consecutive numbers from 1 to 8 by green block attributes, and a measurement point is placed in the centroid of the cube, and marked by a pink block attribute numbered 9.

Use the Data Extraction (DX) command of the AutoCAD® software, to produce an excel file which contains a table of the vertices, with their attribute number and their *x, y, z* coordinates. Another information field that might be useful is the *layer* field. Once the excel file is created, sort the data according to the attribute numbers. Make sure they are consecutive. Name that excel file “coordinates”. The “coordinates” file, created by the AutoCAD® software and sorted by the user for consecutively ordered attribute numbers, is shown below in Table 2-3. The first column is the number of the vertex, or the attribute, the next three columns are the *x*, *y* and *z* coordinates and the last column is the layer.

Table 2-3. Output file of the vertices coordinates

SPACE	**Position X**	**Position Y**	**Position Z**	**Layer**
1	0	0	0	coordinates
2	0	3	0	coordinates
3	3	0	0	coordinates
4	3	3	0	coordinates
5	0	0	3	coordinates
6	0	3	3	coordinates
7	3	0	3	coordinates
8	3	3	3	coordinates
9	1.5	1.5	1.5	measurement points

3) Create a second excel file that contains a table with 5 columns in it. Each *row* of that table will be a triangle family. The first three *columns* are the three vertices that form the triangle. Each vertex will be named after the attribute number it received in the CAD model. The 4th column is the joint material number for the triangle family, and the 5th column is the block material number for that triangle. Name that file “blocks”. If special points are in use, create more excel files that contain the numbers of the special points. Name those files “fixed points”, “measurement points”, “loading points” etc.

Example:

In order to create the cube shown in Figure 2.15, six faces need to be formed, each face composed of two triangles. The “blocks” file that forms the cube is presented in Table 2-4.

Table 2-4. The “blocks” file that contains information regarding triangle families

vertex 1	vertex 2	vertex 3	joint material	block material
1	5	7	0	0
1	7	3	0	0
2	6	5	0	0
2	5	1	0	0
2	6	8	0	0
2	8	4	0	0
4	8	7	0	0
4	7	3	0	0
1	2	4	0	0
1	4	3	0	0
5	6	8	0	0
5	8	7	0	0

The “measurement points” file will contain a single cell with the number “9”.

4) Write and run a script (here performed with MATLAB) that reads the “blocks” file, and retrieves the vertex coordinates from the “coordinates file” according to the vertex (attribute) number. This code also reads the special points files, and retrieves the coordinates for the special points. This code will later create a ‘.txt’ file which the ‘tc’ code of the 3D-DDA can accept as input. Once the ‘tc’ code runs, it will create a ‘bl’ file, which holds in it all the geometrical information of the model, ready to be input for the dynamic forward analysis code of 3D-DDA, ‘tf’.

An example of a MATLAB code used here is presented below.

```
triangles=xlsread(‘blocks');  %create a matrix from the xls file with triangle families
[rows,columns]=size(triangles);
families=(rows);      %number of triangle families
coordinates=xlsread(‘coordinates’);  %create a matrix from the xls file with the coordinatesfpoints=xlsread(‘fixed points');  % create a matrix from the xls file with the fixed
%points
[frows,fcolumns]=size(fpoints);
lpoints=xlsread(‘loading points'); % create a matrix from the xls file with the loading points
[lrows,lcolumns]=size(lpoints);
mpoints=xlsread('measurement points'); % create a matrix from the xls file with the measurement
%points
[mrows,mcolumns]=size(mpoints);
a=[]; %matrix for the triangle family data (1  1  1)
b=[]; %matrix for the coordinates output
c=[]; %matrix for fixed points
d=[]; %matrix for loading points
e=[]; %matrix for measurement points
fixed=frows; %number of fixed points
load=lrows; %number of loading points
meas=mrows; %number of measurement points
hole=0; %number of hole points used in the mesh
bolt=0; %number of blots used in the mesh
points=[fixed load meas hole bolt]; % the line containing # of special points
% in the following lines: the loop for retrieving the coordinates for the triangle families
for i=1:rows
    vertex1=triangles(i,1);
```

```
    value1=coordinates(vertex1, 2:end);
    vertex2=triangles(i,2);
    value2=coordinates(vertex2, 2:end);
    vertex3=triangles(i,3);
    value3=coordinates(vertex3, 2:end);
    b=[b;value1;value2;value3;0 0 0];
    a=[a;1 triangles(i,4) triangles(i,5)];
    i=i+1;
end
% in the following lines: the loop for retrieving the coordinates for the fixed points
for j=1:frows
     vertex1=fpoints(j,1);
     value1=coordinates(vertex1, 2:end);
     c=[c;value1];
end
% in the following lines: the loop for retrieving the coordinates for the loading points
for j=1:lrows
     vertex1=lpoints(j,1);
     value1=coordinates(vertex1, 2:end);
     d=[d;value1];
end
% in the following lines: the loop for retrieving the coordinates for the measurement points
for j=1:mrows
        vertex1=mpoints(j,1);
     value1=coordinates(vertex1, 2:end);
     e=[e;value1];
end
%in the following lines: writing the compatible file for the tc code
fid=fopen('tc.txt', 'wt');
fprintf(fid,'%d \n',families);
fprintf(fid,'%d %d %d %d %d \n',points);
fprintf(fid,'%d %d %d \n',a');
fprintf(fid,'%d \t %d \t %d \t \n',b');
fprintf(fid,'%d %d %d \n',c');
fprintf(fid,'%d %d %d \n',d');
fprintf(fid,'%d %d %d \n',e');
fclose(fid);
```

The procedure of the mesh construction is briefly described in the flow chart in Figure 2.17.

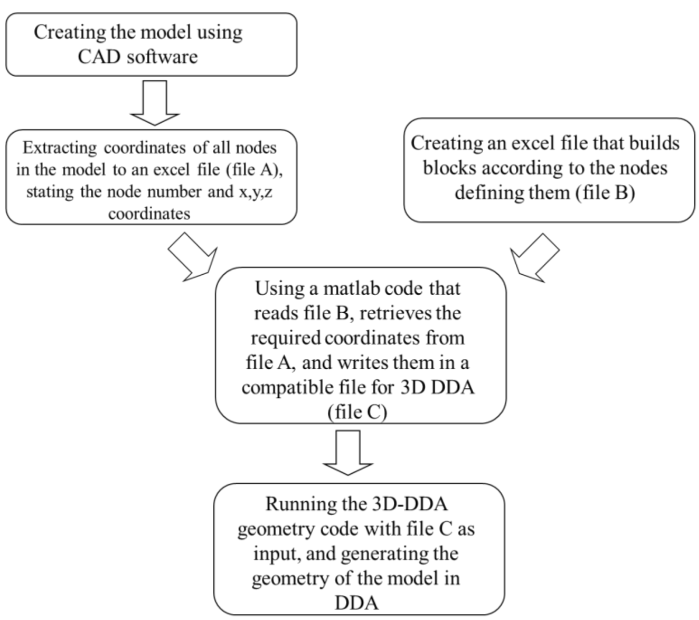

Figure 2.17. The procedure of mesh construction in 3D-DDA with AutoCAD.

2.3.3 Modeling with CAD in 2D-DDA

As stated earlier, modeling in 2D-DDA is much simpler than the 3D-DDA, but the CAD comes in handy here as well, as the 2D-DDA has no graphic interface either. The steps for constructing a mesh in the 2D-DDA using CAD are described below. The procedure is demonstrated for a single square block of the size 3 m*3 m, with a measurement point at its center.

1) Sketch the model in AutoCAD® software using the “line”, rather than the “polyline” command (Figure 2.18). Special points and material lines should also be sketched as well. Here a measurement point is inserted to the center of the square. The different types of input should be put in different layers, clearly named (i.e. blocks, material lines, fixed points etc.).

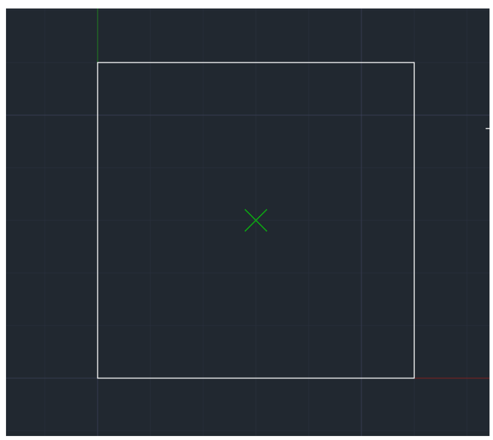

Figure 2.18. The modeled square in AutoCAD. The white lines forming the square are placed in a layer named “blocks”, and the green X marking the measurement point is placed in a layer named “measurement points”.

2) Export the data using the Data Extraction (DX) command of the AutoCAD® software to an excel file which contains the coordinates of the start and end points of the different lines, the coordinates of the special points, as well as the layer names. In this example that excel file is named “coordinates”. This file doesn’t have to be sorted in any way, unless the order of the special points or the blocks is important. For example, if there are 9 measurement points, they should be sorted in a way that will allow the user to clearly identify them when reading the output of the DDA program. The ‘coordinates’ file for the example shown here is presented in Table 2-5.

Table 2-5. The 'coordinates' output file of the DX command of AutoCAD

Layer	Start X	Start Y	End X	End Y	Position X	Position Y
measurement points					1.5	1.5
blocks	3	0	0	0		
blocks	0	0	0	3		
blocks	3	3	3	0		
blocks	0	3	3	3		

3) Write and run a script (here performed with MATLAB) that reads the 'coordinates' file, and according to the name of the layer, puts the input coordinates data in the right place in the 'dc' input file. The script used in the example shown here is presented below:

```
clear;
[line_coord, layer]=xlsread('coordinates’); %reads the file with the line coordinates
[rows,columns]=size(line_coord);
a=[]; % line geometry matrix
b=[]; % fixed point matrix
c=[]; %loading point matrix
d=[]; %material line matrix
e=[]; %measurement point matrix
f=[]; %boundary joints
% the next loop will sort the different types of data in the ‘coordinates’ file to the different
%matrices
for i=1:rows
    if findstr(layer{i},'blocks')
        a=[a;line_coord(i, 1:4), 1];
    end
    if findstr(layer{i}, 'fixed points')
        b=[b;line_coord(i, 5:6), line_coord(i, 5:6)];
    end
    if findstr(layer{i},'load points')
        c=[c;line_coord(i, 5:6)];
    end
    if findstr(layer{i},'material lines')
        d=[d;line_coord(i, 1:4), 1];
    end
     if findstr(layer{i},'measurement points')
        e=[e;line_coord(i, 5:6)];
     end
     if findstr(layer{i},'boundary')
        f=[f;line_coord(i, 1:4),1];
     end
    end
mat_line=size(d,1);
bolt=0;
fixed=size(b,1);
load=size(c,1);
meas=size(e,1);
hole=0;


fid=fopen('dc.txt', 'wt'); % open file for writing
fprintf(fid,'%d \n',0.001);  %write to file minimum edge length parameter
fprintf(fid,'%d   %d \n',size(a,1), size(f,1)); % write to file  total number of   lines and of
%boundary lines
fprintf(fid,'%d \n', mat_line); %write to file number of material lines
fprintf(fid,'%d  %d  %d  %d  %d  \n', bolt, fixed, load, meas, hole); % write to file numbers of
%special points
fprintf(fid,'%d %d %d %d %d \n',a'); % write to file the matrix of the line geometry and joint
%material lines
fprintf(fid,'%d %d %d %d %d \n',f');
fprintf(fid,'%d %d %d %d %d \n\n',d');
fprintf(fid,'%d %d %d %d \n\n',b');
```

```
fprintf(fid,'%d %d  \n',c');
fprintf(fid,'%d %d \n',e');
fclose(fid);
```

The procedure of mesh construction with AutoCAD in 2D-DDA is briefly described in the flow chart in Figure 2.19.

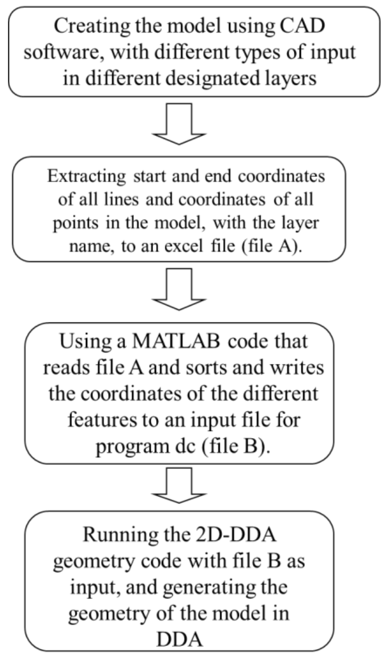

Figure 2.19. A flow chart describing the procedure of mesh construction using AutoCAD in 2D-DDA.

2.4 Numerical and modeling issues with 3D-DDA

2.4.1 The coupled effect of dynamic parameter and time step interval

During simulations of a multi-block model with 3D – DDA, several numerical problems were observed. In a discrete element mesh of 197 blocks (see Figure 2.14), it was found that in order for the numerical solution to converge, a very small time step interval in the order of 10^{-5} sec must be used, as well as kinetic damping of at least 3%, i.e. *dd* = 0.97 (see section 2.1.3). Numerical simulations with those parameters provided displacements that were a few orders of magnitude smaller than expected. A semi-analytical analysis was performed in order to find the source of the unexpected small displacements.

Using the MATLAB software package, the time dependent displacements of a mass driven by a constant force were computed (Figure 2.20).

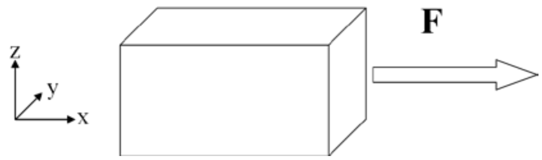

Figure 2.20. The model used for the semi- analytical simulations.

The input acceleration of the mass is constant. The simulations were performed under different user specified time step interval (Δt) and dynamic coefficient (*dd*). As explained in section 2.1.3, the dynamic coefficient introduces kinetic (numerical) damping into the system, by multiplying the initial velocity of the block at the beginning of a time step by the *dd* parameter, after inheriting the terminal velocity from the previous time step. The semi-analytical calculations performed at each time step are presented in Figure 2.21, with trapezoidal integration (different from the DDA, where analytical Simplex integration is used (Shi, 1988)).

$$\ddot{u}_{i,initial} = const.$$
$$\dot{u}_{i,initial} = dd * \dot{u}_{i-1,final}$$
$$u_{i,initial} = u_{i-1,final}$$

$$\ddot{u}_{i,final} = const.$$
$$\dot{u}_{i,final} = \dot{u}_{i,initial} + \ddot{u}\Delta t$$
$$u_{i,final} = u_{i,initial} + \dot{u}_{i,final}\Delta t$$

Δt

Figure 2.21. The calculations at each time step of the semi-analytical solution.

First a dynamic coefficient of 0.97, which corresponds to 3% of kinetic damping, was used with different values of time step interval, with the lowest being 0.00001 sec, and the highest being 0.01 sec. The results are presented in Figure 2.22. As is evident from Figure 2.22, the time step interval is a crucial parameter which controls the accumulated displacement during the analysis when kinetic damping is used. The displacement accumulated after 0.5 sec with time step interval of 0.00001 sec ($1.041e^{-5}$ m) is almost 3 orders of magnitude smaller than the accumulated displacement after 0.5 sec with time step interval of 0.01 sec (0.005 m), under the same force applied. This result clearly demonstrates the significance of the time step size selection when kinetic damping is applied (for example in (Hatzor et al., 2004)).

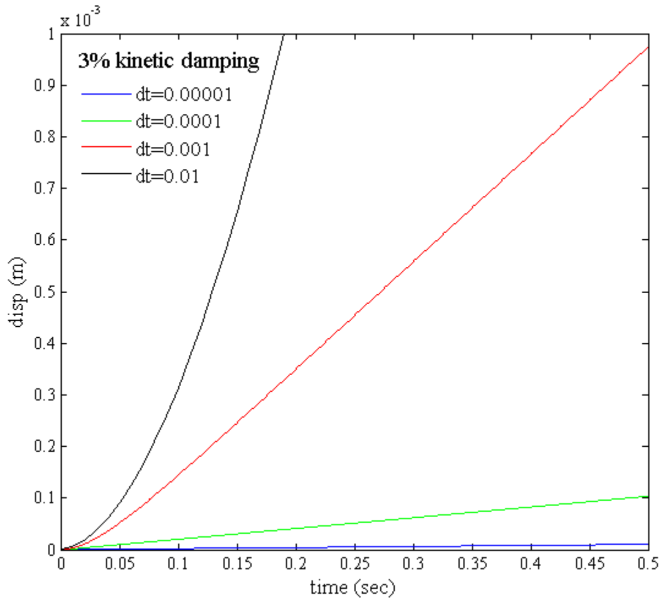

Figure 2.22. Results of simulations with kinetic damping of 3% for different values of time step interval.

The same procedure was performed with the 3D-DDA. 3D- DDA simulations were modeled by two blocks: an overriding block subjected to a constant horizontal force (or acceleration), and an underlying stationary block that exists only to prevent free falling of the overriding block (Figure 2.23). Friction between blocks is set to 0.

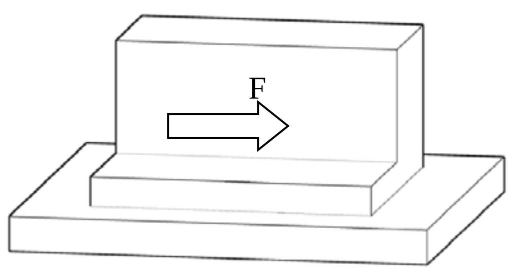

Figure 2.23. The model used in the DDA analyses.

Force was applied at the centroid of the overriding block. Four time step intervals were used in these simulations, following the semi-analytical solution, results presented in Figure 2.24 (semi-logarithmic scale).

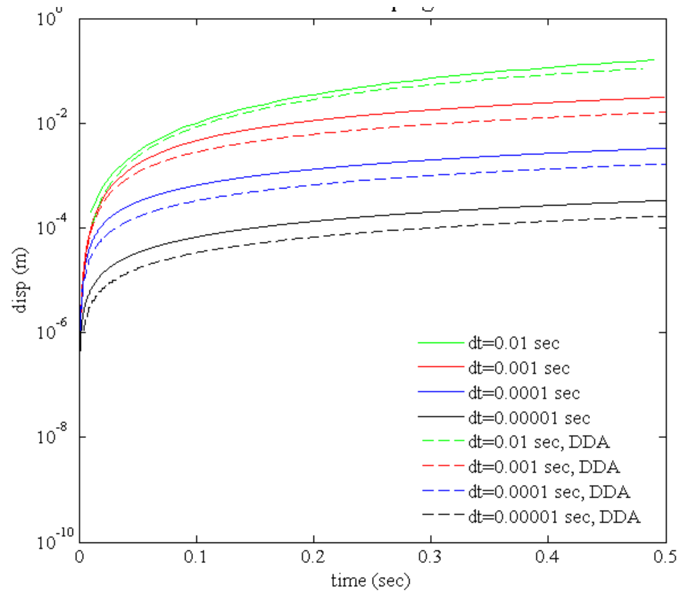

Figure 2.24. Comparison between 3D-DDA and semi-analytical simulations at four different time step intervals and damping of 3%. Solid curves are the semi-analytical solution, and dashed curves are 3D-DDA solution.

As can be observed in Figure 2.24, the DDA solution does not follow the exact values of the analytical solution, but does follow the same trend: the accumulated displacement decreases with decreasing time step interval, by three orders of magnitude. The difference between the two solutions could be explained by the different integration schemes, as mentioned above.

This phenomenon was not observed when no kinetic damping was used: the time step size had no effect on the cumulative displacement. Figure 2.25 presents the results of 3D-DDA as well as analytical simulations for different time step intervals with 0% kinetic damping. The 3D-DDA solution follows the values of the analytical solution: the time step interval has no effect on the cumulative displacement when no kinetic damping is used.

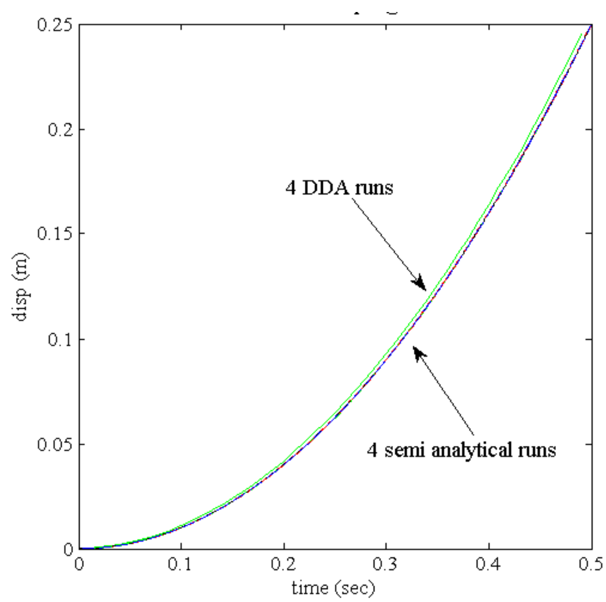

Figure 2.25. Four 3D-DDA simulations and four semi-analytical simulations with different time step intervals (similar to the ones used in Figures 2.21 and 2.23) with 0% damping.

When the time step interval was fixed, and the dynamic coefficient *dd* was set to four different values, 1, 0.99, 0.98 and 0.97 (corresponds to 0, 1, 2 and 3% kinetic damping), the effect of the damping value was examined. This procedure was performed for four Δ values: 0.01, 0.001, 0.0001 and 0.00001 sec. Results are presented in Figure 2.26. From Figure 2.26 it is evident that introducing kinetic damping has a significant effect on the accumulated displacement, but this effect weakens with increasing time step interval. The smaller the time step interval is, the difference between the accumulated displacement of 0% and 1 % damping grows larger. Furthermore, it seems that the largest difference in accumulated displacement is indeed between 0% and 1% damping, and smaller damping values show much smaller displacement differences between them.

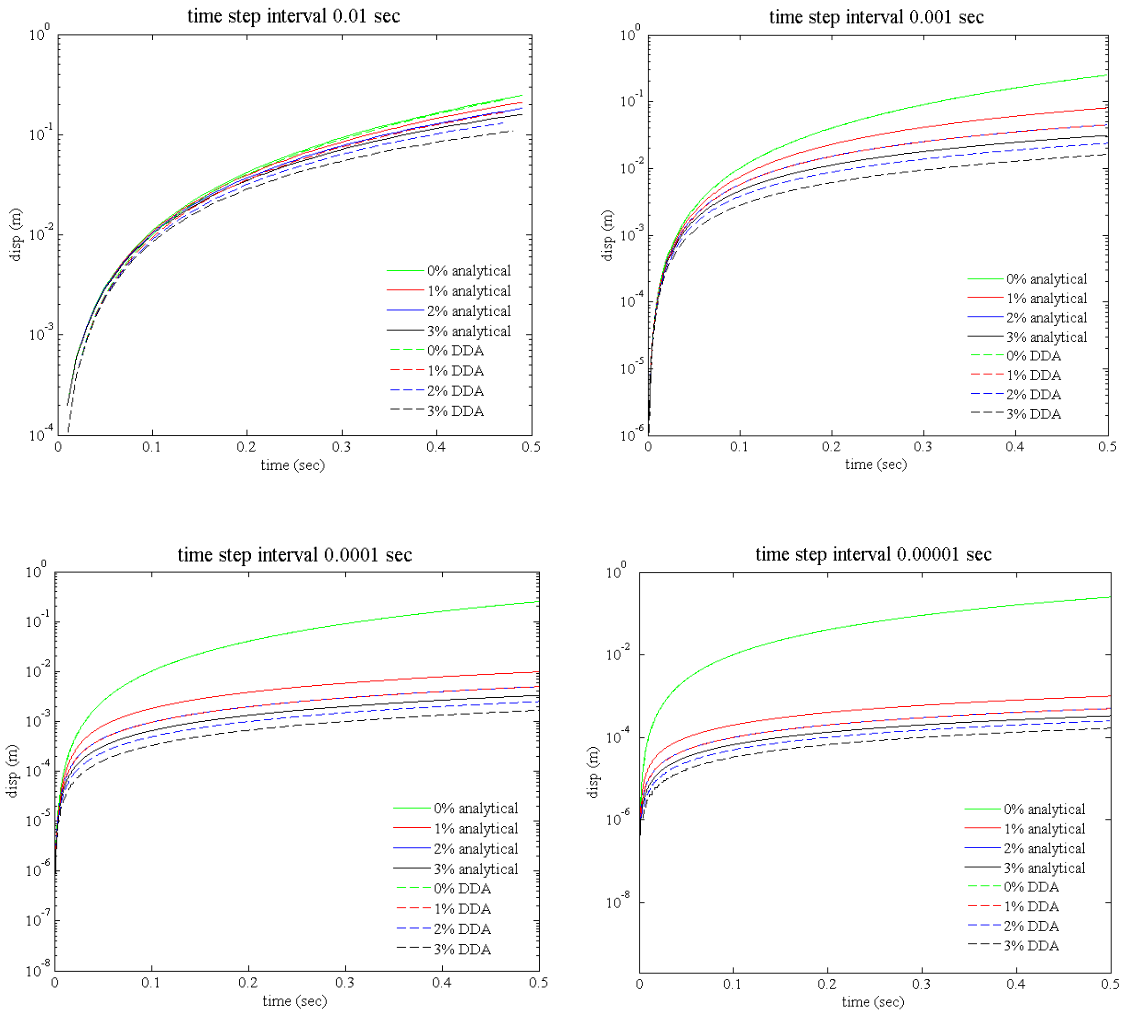

Figure 2.26. Results of simulations with constant time step intervals and different damping values.

To summarize, the combination of a very small time step interval and kinetic damping of a small percentage significantly decreases the cumulative displacement during the simulation. It is also evident that a small increase in kinetic damping coefficient will not make a great difference when very small time steps are used. In general, it is preferable to use *dd* = 1 in dynamic simulations, as the displacements will be reduced due to the algorithmic damping inherit to the DDA in any event, but sometimes multi block systems do not converge in the latest 2D-DDA code version we utilize in this research without introduction of some kinetic damping; often 1% to 2% kinetic damping proves to be sufficient to enable the system of equations to converge during open-close iterations in every time step. The coupled effect of kinetic damping and time step size as demonstrated here, should be taken into consideration when convergence of the solution requires the use of $dd < 1$, and when analyzing results of simulations where kinetic damping is used, as these two numeric control parameters can lead to numeric errors that have no physical basis.

2.4.2 A note on proper force input to a loading point in site response studies

2.4.2.1 The problem

When attempting to simulate an earthquake, one way to do so is to use a model of a stationary base, incapable of moving, overlain by a moving base, simulating the shaking ground, either excited by acceleration or displaced by displacement time history. The modeled structure, either natural or manmade, lies above the moving base, free to respond to the vibrations. Input of displacement time history is performed by directly assigning displacements to a fixed point. Exciting the base with acceleration time history is carried out with a loading point, to which loads have to be assigned, which means the acceleration time history has to be multiplied by the block mass, in order to obtain force values (Newton's second law $F = ma$). The question arising in this case is whether only the mass of the induced base block should be considered, or should the mass of the responding blocks mounting the base (i.e. the structure itself) be considered as well.

2.4.2.2 The test

A simulation study was performed in order to determine which approach is the most appropriate. A mesh composed of three blocks was modeled (Figure 2.27): bottom stationary base block, middle induced block, and top responding block. Friction between the lower two blocks was set to 0, and the friction between the upper two blocks was set to a very high value, so as to avoid any frictional force effects on the displacement of the middle block.

Figure 2.27. The mesh used for the mass dilemma study. The lowermost block is fixed, the middle block is the moving base (friction between the two lower blocks is set to 0) and the upper block is responding.

The acceleration function used as input for the middle block is $\ddot{d}(t) = A\sin(\omega t)$, with amplitude of A = 2 m/sec^2 and frequency of $\omega = 2\pi$ sec^{-1} (f = 1 Hz). The displacements of the middle block were measured, and later on compared with the displacements calculated by a simple analytical solution for a block starting at rest ($\dot{d}(0) = 0$), that does not depend on the mass of the block:

$$d(t) = -\frac{A}{\omega^2}\sin(\omega t) + \frac{A}{\omega}t \qquad \text{Equation 2-28}$$

2.4.2.3 The results

Figure 2.28 presents the comparison between the displacements calculated by the analytical solution in Eq. 2.18, independent of mass, and the displacements obtained with 2D-DDA, where the loaded block is subjected to the input acceleration function multiplied by the mass of a) the induced block only and b) the induced and responding blocks. As is evident from Figure 2.28b, where an excellent agreement between the analytical and numerical solutions when the acceleration function is multiplied by the mass of both blocks is observed, using the masses of both blocks is the correct approach.

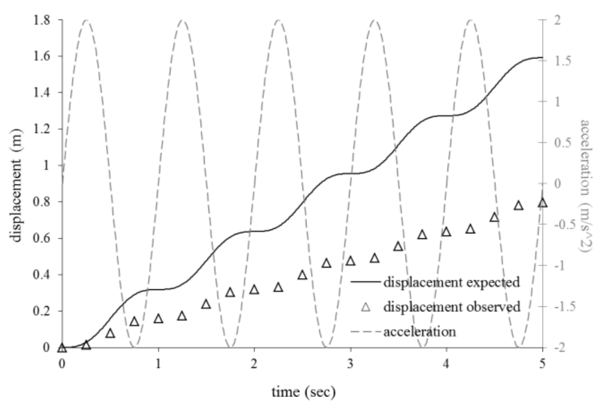

a

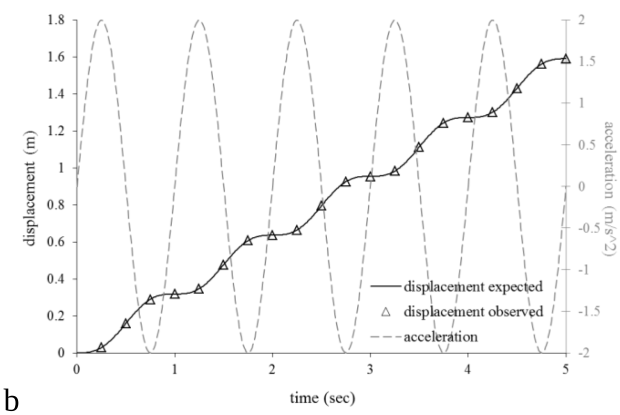

b

Figure 2.28. Comparison between the analytical solution and the DDA solution for the model presented in Figure 2.27, subjected to acceleration function of $\ddot{d}(t) = A\sin(\omega t)$ multiplied by a) the mass of the induced middle block and b) the mass of both the induced and responding blocks.

To summarize, when dynamically exciting a structure with an acceleration time history through a loading point scheme, as explained in section 2.4.2.1, the acceleration record should be multiplied by the mass of the block containing the loading point, as well as the mass of all the overriding blocks, if exist, in order to correctly represent the dynamic forces.

3. Site response analysis with two-dimensional numerical discontinuous deformation analysis

3.1 Introduction

In this chapter the possibility of performing numerical site response analysis is explored. The advantages of numerical site response analysis are evident, since a reliable numerical platform will render complicated and expensive field tests less necessary. For this purpose the dynamic, implicit, discrete-element numerical two – dimensional Discontinuous Deformation Analysis (2D-DDA) method (Shi, 1993) is employed. The site response analysis results obtained with 2D-DDA are compared with an experimental site response survey performed in the field for a historic, tall and slender limestone multi-drum column situated in Avdat National Park, a World Heritage Site in southern Israel.

3.1.1 Scientific background

The analysis of seismic site response is very important since the amplification of seismic waves in some specific areas can be very strong (Burridge et al., 1980; Cruz et al., 1993; Olsen, 2000; Seed and Idriss, 1969; Semblat et al., 2005). Reflections and scattering of seismic waves near the surface, at layer interfaces, or around topographic irregularities often worsen the consequences of earthquakes (Semblat et al., 2000). The maximum amplification and corresponding resonance frequency depend on several factors including the thickness of the overlying layers, their shear modulus, damping ratio, and density (Siddiqqi and Atkinson, 2002). Although alternating layer stiffness in the soil column (e.g. Seed and Idriss, 1969) and geometrical basin effects (e.g. Field, 1996) have been cited as the most common sources of amplification, topographic effect has been reported to be a significant source of motion amplification as well (e.g. Ashford et al., 1997; Bouchon and Barker, 1996; Zaslavsky and Shapira, 2000a). While it is well established that soft soil deposits may amplify ground motion, it is often assumed that hard-rock sites are safe. However, recent studies suggest that rock sites may also exhibit significant amplification, possibly because of their shear-wave velocity gradient (Beresnev and Atkinson, 1997; Boore and Joyner, 1997; Steidl et al., 1996).

Ground motions developed near the surface are typically attributed to upward propagation of shear waves from an underlying rock formation (Idriss and Seed, 1967). If the ground surface, the rock surface and the boundaries between soil layers are essentially horizontal, the lateral extent of the deposit has no influence on the response and the deposit may be considered as a series of semi-infinite layers. In such cases the ground motions induced by a seismic excitation at the base are the result of only shear deformations in the soil and the deposit may be considered as a one-dimensional shear beam. Site response in this case may be estimated using well developed, one-dimensional computational approaches, such as the program SHAKE (Lysmer et al., 1972; Schnabel et al., 1972). If however the ground surface, the rock surface or the boundaries between different soil layers are inclined, analyses of the response of the soil deposit can only be performed by numerical techniques.

3.1.2 Avdat National Park – historical, geographical and geological overview

Avdat, a major ancient Nabatean road station along the Route of Spices from Petra to Gaza, lies in the central Negev highlands of southern Israel, 655 m above sea level and 80 m above its surroundings (see Figures 3.1, 3.2). Avdat was established in the 3rd century BC, and was annexed to the Roman Empire at 106 AD along with the entire Nabatean kingdom (Negev, 1988). The city includes remains from the Nabatean, Roman and Byzantine periods. Avdat was abandoned in 636 AD, never to be occupied again. A strong earthquake that struck the region between 631-636 AD is believed to have been the main reason for its abandonment (Fabian, 1998). Indeed, many buildings in Avdat show evidence of seismic damage, including ones that were used in the 7th century AD (Mazor and Korjenkov, 2001). In 2005, the Avdat National Park was declared a UNESCO world heritage site.

Figure 3.1. A location map of Avdat National Park. Inset: plate tectonic setting of the Dead Sea Transform (DST), a left lateral fault, which transfers the opening in the Red Sea to the collision between Arabia and Eurasia by northward movement of the Arabian plate with respect to the African Plate. NAF and EAF are the Northern and Eastern Anatolian Faults, respectively.

Figure 3.2. Aerial photo of Avdat. The ellipse delineates the site of experimental survey. At the time of the site response survey only one column was standing at the site, the rest were taken down for restoration. Photograph by Yuval Nadel.

The city of Avdat lies on the Avdat Highlands, which consist of rocks from the Eocene (50-35 million years before present) locally known as the Matred Formation which consists of hard limestone with Nummulites (Zilberman, 1989). Avdat is located about 50 km east of the Dead Sea Transform, an active strike-slip fault that separates the Arabian tectonic plate to the east and the African plate to the west (see Figure 3.1). The expected PGA for the region is 0.087 *g*, with 10% probability of exceedance in 50 years (S.I.I., 2004).

3.2 Research methods

The structure selected for the site response analysis is a single multi-drum free standing column that was used for supporting the roof of a Nabatean temple (Figure 3.3), located at the "Terrace", a lookout point to the west, delineated by the ellipse in Figure 3.2.

Figure 3.3. The multi-drum column selected for site response analysis at Avdat.

3.2.1 Experimental site response measurements

The site response survey was performed by a professional team from the Geophysical Institute of Israel, under our supervision, and preliminary results are reported by Zaslavsky et al.(2011). Data acquisition equipment included a 12-channel amplifier with band pass filters of 0.2-25 Hz, GPS (for timing) and a laptop computer with analog-to-digital conversion card. Digital recordings were made at a sampling rate of 100 samples per second at 16-bit resolution. The GII-

SDA, digital seismic data acquisition system is designed for site response field investigations. The seismometers used were single component sensitive velocity transducers (L4C by Mark Products) with a natural frequency of 1.0 Hz and 70% critical damping. All the equipment including sensors, power supply, amplifiers, personal computers and connectors were installed on a vehicle, which also served as a recording center. Four velocity seismometers were placed on the column: two at the top of the column, and two nearest to its base. Each pair of seismometers was placed perpendicular to one another in north-south and east-west directions (X and Y, respectively, see Figure 3.4).

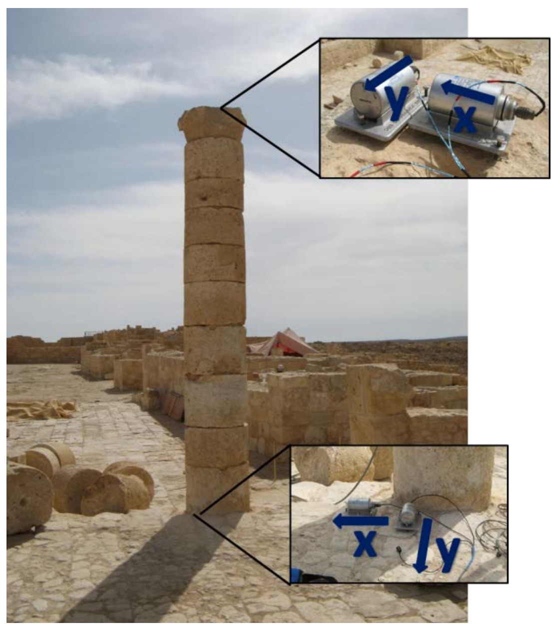

Figure 3.4. Seismometers location on the column.

The response of the column to three different loading modes was recorded with the velocity seismometers positioned at the top and base of the column as follows: 1) ambient, or background, noise; 2) dynamic load applied at the base of the column by impact of a sledgehammer (see Figure 3.5a), and 3) static load obtained by application of manual push and release at the top of the column (see Figure 3.5b).

a)  b) 

Figure 3.5. Different excitation modes at the experimental site response survey. a) sledgehammer blows to the bottom of the column and b)manual push to the top of the column.

3.2.2 Numerical site response analysis

The numerical method used for the numerical site response analysis is the 2D-DDA. The fundamentals of the DDA are reviewed in Chapter 2 of this dissertation, and will not be reviewed again here. Still, an important point specifically regarding this chapter should be made. As pointed out in Chapter 2, the DDA computes the first order approximation of displacements at any point (x, y) (Shi, 1993). By adopting first order displacement approximation, the distribution of the stresses and strains is constant in a block, a simplification that limits the accuracy of the DDA method when dealing with wave propagation problems in relatively large blocks with respect to the wave length size. Therefore, the issue of wave propagation accuracy with DDA is addressed in this section in some detail.

In this study, very small disturbances were applied to a multi drum column, either by applying a gentle push at the top or by applying a blow with a sledgehammer at the bottom of the column, and the response spectra for data computed with DDA were compared to the response spectra for data measured in the field. Because the disturbance is very small, no out of plane or wobbling motions between the drums were expected during column vibration and therefore a two dimensional approach was assumed valid in this case.

3.2.2.1 The model

The 2D-DDA mesh is comprised of eleven blocks: one large foundation block, fixed in space by three fixed points, and ten rectangular blocks, placed one on top of the other with proportions similar to the actual column in the field. The model was excited in either one of two loading points: one at the lowermost drum, simulating the sledgehammer impacts, or "dynamic" loading, and one at the uppermost drum, representing the manual push, or "static" loading (see Figure 3.6).

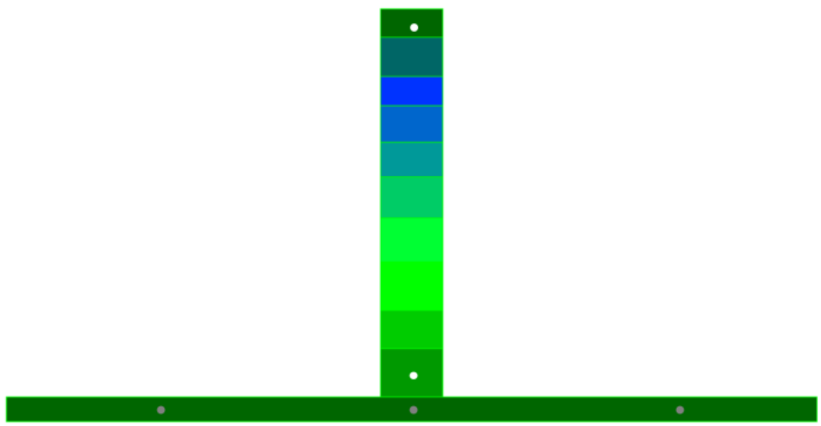

Figure 3.6: The 2D-DDA mesh used in the numerical modeling of the Avdat column. The lowermost block is fixed in place by three fixed points (grey circles), dynamic load is applied in either of the two loading points (white circles).

3.2.2.2 Optimization of numerical control parameters

Before performing simulations under external forces, several models loaded by gravity alone were analyzed in order to optimize the user defined numerical control parameters, while the blocks settle under their own weight. Simulations under gravity only were run for 15 seconds of real time. Two Δ (time step size) values were used: 0.01 and 0.001 sec. The assumed maximum displacement per time step ratio was set equal to Δ, and sensitivity analysis was performed to optimize the penalty value (k) for the two time step sizes. Two numerical responses to gravitational load were investigated: 1) the time it takes for the initial oscillations of the column in the vertical direction to stabilize, an effect referred to herein as "gravity turn-on", and 2) a numerical artifact where horizontal displacements of the uppermost block, which naturally have no physical meaning when subjecting the symmetrical column to vertical gravitational loading, are obtained. The numerical and physical parameters used in the simulations are listed in Table 3-1.

Table 3-1. Numerical and physical parameters used in the Avdat column simulations

Parameter	**value**
Dynamic parameter *dd*	1 (fully dynamic)
k (contact spring stiffness)	$1x10^{7}$ - $1x10^{11}$ N/m
Δ (time step size)	0.01-0.001 sec
Maximum displacement ratio	Identical to Δ
Density	2250 kg/m^3
Young's modulus	17 GPa
Poisson's ratio	0.22

Results of sensitivity analyses are presented in Table 3-2. Gravity turn-on is achieved much faster with the larger time step, because of the inherent algorithmic damping in DDA, the amount of which is directly proportional to the time step size (Doolin and Sitar, 2004). Furthermore, the smaller artificial horizontal displacements are obtained when using a larger time step, again, because of the algorithmic damping effect. The selection of the optimal contact spring stiffness for forward modeling was made based on the results of the sensitivity analyses for the smaller time step as it was more sensitive to the change in penalty value. The range of optimal contact spring stiffness is between $1x10^8$ and $1x10^9$ N/m (shaded in Table 3-2).

Table 3-2. Sensitivity analysis of numerical control parameters for gravitational load only using the 2D-DDA model shown in Figure 3.6. All other input parameters are listed in Table 3-1. Legend: Δ = time step interval, *k* = contact spring stiffness, u = horizontal displacement of the uppermost block

k (N/m)	**Δ = 0.001 sec**		**Δ= 0.01 sec**	
	Real Time to gravity turn on (sec)	**u (cm)**	**Real Time to gravity turn on (sec)**	**u (cm)**
$1x10^7$	Not stable	N/A	Not stable	N/A
$5x10^7$	8	0	1	0.000005
$1x10^8$	5 to 6	0	1	0.000002
$2x10^8$	3 to 4	0	0.5	0.000001
$3x10^8$	2 to 3	0	0.7	0
$4x10^8$	2 to 3	0	0.7	0
$5x10^8$	2 to 3	0	N/A	N/A
$6x10^8$	2 to 3	0	N/A	N/A
$7x10^8$	2 to 3	0	N/A	N/A
$8x10^8$	2 to 3	0	0.6	0

$9x10^8$	2 to 3	0	N/A	N/A
$1x10^9$	2	0	N/A	N/A
$2x10^9$	2	0	0.55	0
$3x10^9$	2	0.000006	N/A	N/A
$4x10^9$	2	0	N/A	N/A
$5x10^9$	Not stable	Not stable	0.5	0
$6x10^9$	Not stable	Not stable	N/A	N/A
$1x10^{10}$	Not stable	Not stable	1	0
$1x10^{11}$	N/A	N/A	1	0
$1x10^{13}$	N/A	N/A	1	0

3.2.2.3 Numerical loading modes

As mentioned earlier, load was applied at either of the two loading points marked by white circles in Figure 3.6. When simulating dynamic impact (sledgehammer blow), force was applied at a single time step of the analysis by a pulse function (Figure 3.7a). When simulating static load (manual push and release), force was applied as a step function (Figure 3.7b), for a time interval of one second. Dynamic load was applied with values between 10,000 and 300,000 N; column vibrations were not always obtained under the lower load values. Static load was applied with values between 100 and 3000 N; higher load values triggered some initial translation of the uppermost block in the horizontal direction, followed by free vibrations of the column.

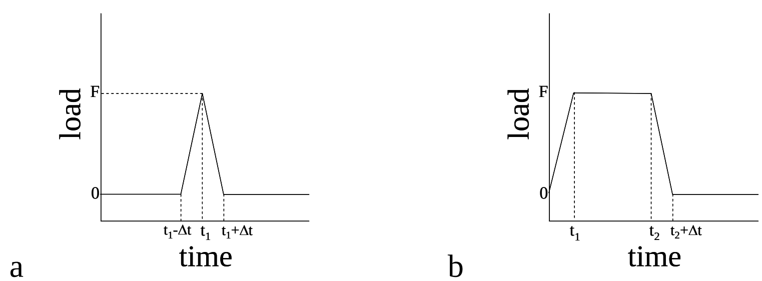

Figure 3.7: Input loading functions used as input in 2D-DDA simulations: a) dynamic load function used to simulate sledgehammer impulse applied at the base of the column, b) static load function used to simulate the push and release applied manually at the top of the column.

3.3 Results

3.3.1 Field experiment results

The vibrations recorded in the seismometers under the different modes of excitation were analyzed by the GII team for modal frequencies, as these appear as local peaks in the Fourier velocity spectra (Zaslavsky et al., 2011). The first and second resonance modes obtained under the three different styles of excitations are similar, with the first resonance mode at 3.0 – 3.8 Hz and the second mode at 4.2 – 5.3 Hz (see Figure 3.8).

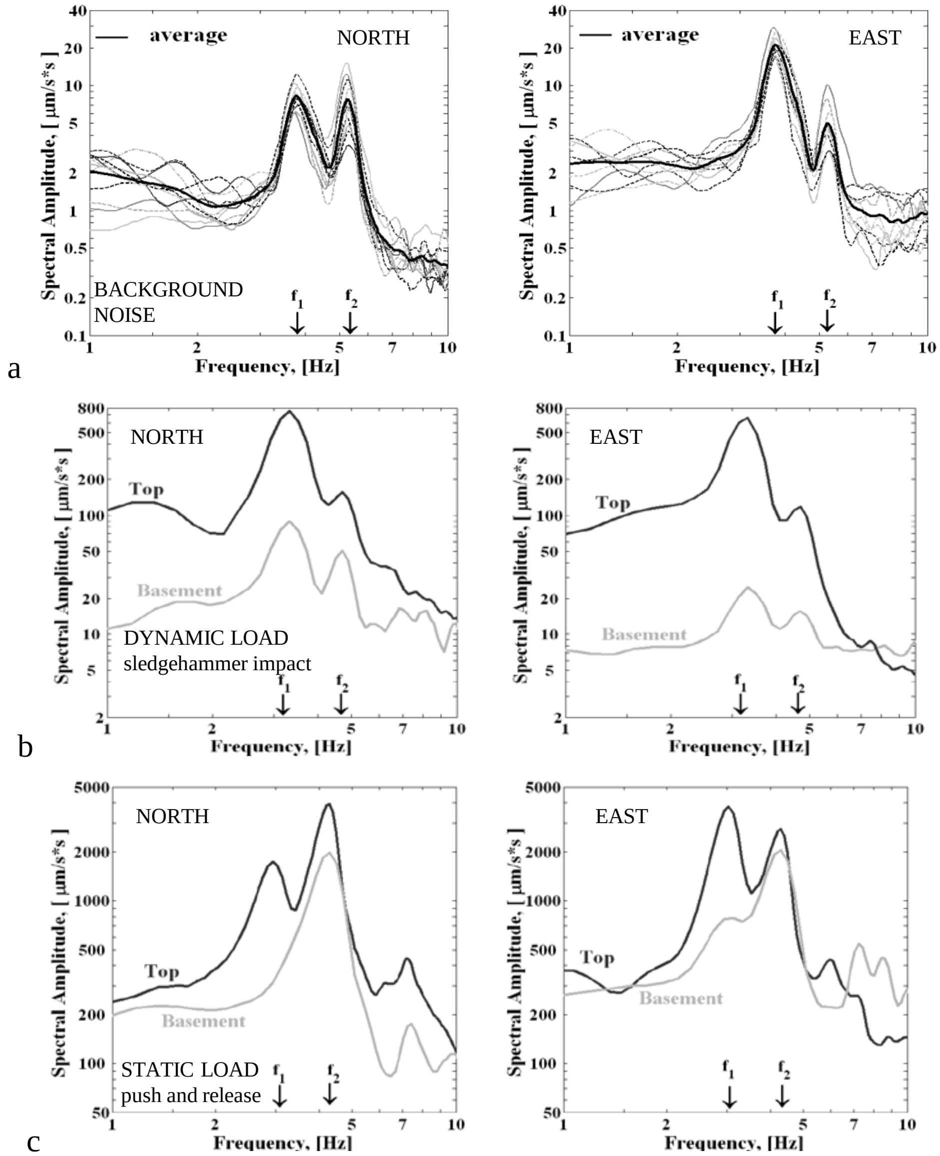

Figure 3.8. Experimentally obtained Fourier velocity amplitude spectra in X (H332) and Y (H748) directions for ambient (a), dynamic (b), and static (c) excitation at the base and top of the column. After (Zaslavsky et al., 2011).

3.3.2 Numerical results

An example of the response of the uppermost block of the column to static load of 1000 N is presented in Figure 3.9. These displacements were obtained with *k* value of $4*10^8$ N/m. Note the vertical oscillations of the block during the first two seconds – this is the "gravity turn-on" effect mentioned in 3.2.2.2. No displacements were observed in the vertical direction after the first two seconds of oscillations. As for the horizontal displacement – no displacements were observed in this simulation until t = 4 sec, when the static force was applied, and at t = 5 sec, when the static force was removed, the column started its free vibrations. Note that the amplitude of the motion decreases with time, but the frequency remains unchanged, implying the column does not enter the rocking mode, as the frequency of motion of a free standing rocking column changes with time due to energy loss at impact (Housner, 1963; Makris and Roussos, 2000; Yagoda-Biran and Hatzor, 2010).

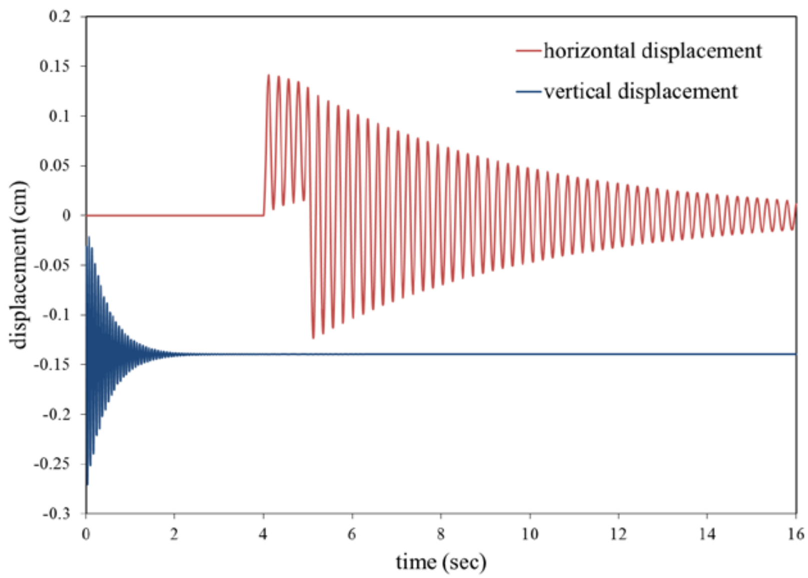

Figure 3.9. The horizontal and vertical displacements of the uppermost block of the multi drum column, when subjected to static load of 1000N, with $k = 4x10^8$ N/m.

FFT analysis of the data presented in Figure 3.9 is shown in Figure 3.10 along with the average curve obtained from the geophysical experiments. Note that the results of the field experiment indicate two modes, whereas DDA results indicate only a single mode. This discrepancy could arise from soil structure interactions that may be present in the field but are prohibited in the DDA model as the base block is fixed in the model (see Figure 3.6).

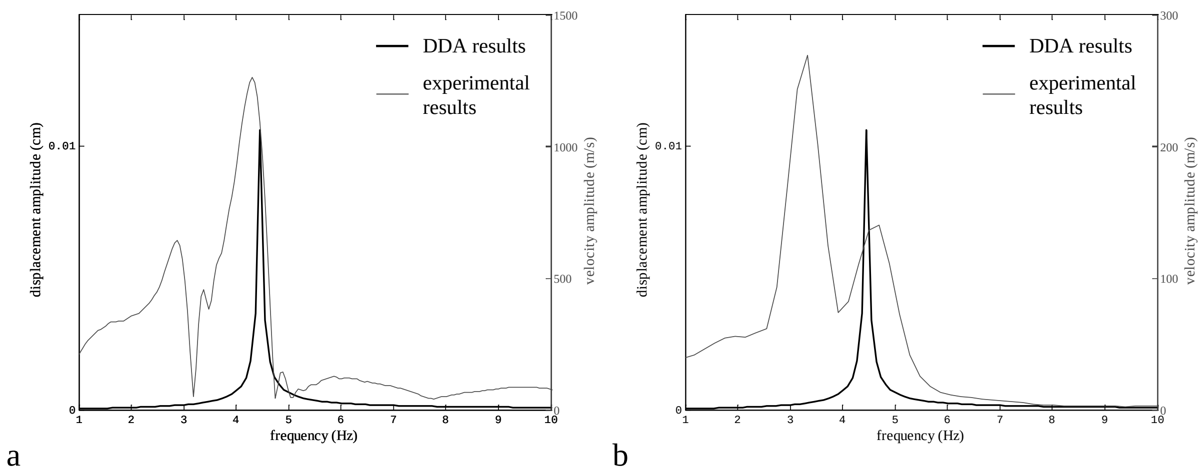

Figure 3.10: Response spectra of studied column: comparison between DDA and experimental results. DDA simulations were executed with penalty value of $4x10^8$ N/m. a) static loading, b) dynamic loading.

Results of dynamic DDA simulations under static and dynamic loads are presented in Table 3-3 with the obtained dominant frequencies under different values of contact spring stiffness. Inspection of the results in Table 3-3 leads to the following conclusions:

1) The dominant frequency of the modeled system obtained with DDA is highly dependent upon the penalty value. It increases with increasing spring stiffness from 2.3 Hz with k = $1x10^8$ N/m to 6.3 Hz with k = $1x10^9$ N/m.
2) The dominant frequency of the modeled system as obtained with DDA does not depend on the loading mechanism or the magnitude of the applied force; similar values are obtained for both static and dynamic loading for the entire range of simulated loads.
3) The dominant frequency of the modeled system as obtained with DDA does not depend on the time interval used (a range of 0.01 to 0.0001 sec was analyzed, results for Δ = 0.0001 sec not shown here for brevity).
4) Finally, all the dominant frequencies that were obtained with 2D-DDA for the optimal range of spring stiffness are in the range of the two dominant modes obtained experimentally at the site. This result confirms the validity of 2D-DDA as a site response analysis tool for geotechnical earthquake engineering.

Table 3-3: Results of the column response to external "dynamic" and "static" forces. The choice of penalty value which returns results that best agree with field experiment is shaded

Contact spring stiffness (N/m)	**Dominant frequency (Hz) for dynamic loading**	**Dominant frequency (Hz) for static loading**
$1x10^8$	2.3-2.4	2.4
$2x10^8$	3.3	3.3
$4x10^8$	4.2-4.3	4.3-4.5
$7x10^8$	5.1	5.1-5.2
$1x10^9$	5.9-6	5.9, 6.2-6.3

3.4 Discussion

A well-known dilemma in dynamic numerical analysis is the best choice of the time step size, since it is not only critical for the stability and efficiency of the solution, but also for its accuracy. In this work, one criterion for selecting an optimal penalty value was the absence of horizontal displacements when subjecting a multi block column to gravitational load. Inspection of sensitivity analyses results (Table 3-2) reveals that when using a relatively large time step size of 0.01 sec no horizontal displacements are obtained numerically for a larger range of penalty values than when using a relatively small time step of 0.001 sec. The absence of horizontal displacements when using the larger time step results from the algorithmic damping effect (Doolin and Sitar, 2004). It should be pointed out, however, that with increased time step size the numerical error increases and therefore a smaller time step would be more desirable, from an accuracy stand point. There is a price to pay, however, when using a smaller time step: stability and gravity turn-on will be achieved after a longer period of real time, due to a lesser algorithmic damping effect. This will require longer CPU time before obtaining a stable solution, an issue that may be a problem when solving a multi-block system, even with fast computers.

Regarding the penalty value and its effect on numerical results, it was shown here that the obtained resonance frequency with DDA is highly dependent upon the choice of *k* (see Table 3-3) with higher dominant frequencies obtained with increasing *k* values, as illustrated in Figure 3.11. This is intuitive, because with increasing *k* value the modeled structure is expected to behave more rigidly. Furthermore, the amplitude of the resonance modes clearly decreases with increasing penalty value, as shown in Figure 3.11. In order to obtain an acceptable penalty value for such problems a preliminary calibration test may be necessary, as performed here (see Table 3-2). Indeed, the best fit penalty value for the field test of $4*10^8$ N/m falls well within the acceptable range of penalty values obtained from the preliminary calibration, where a range from $1*10^8$ N/m to $1*10^9$ N/m proved acceptable.

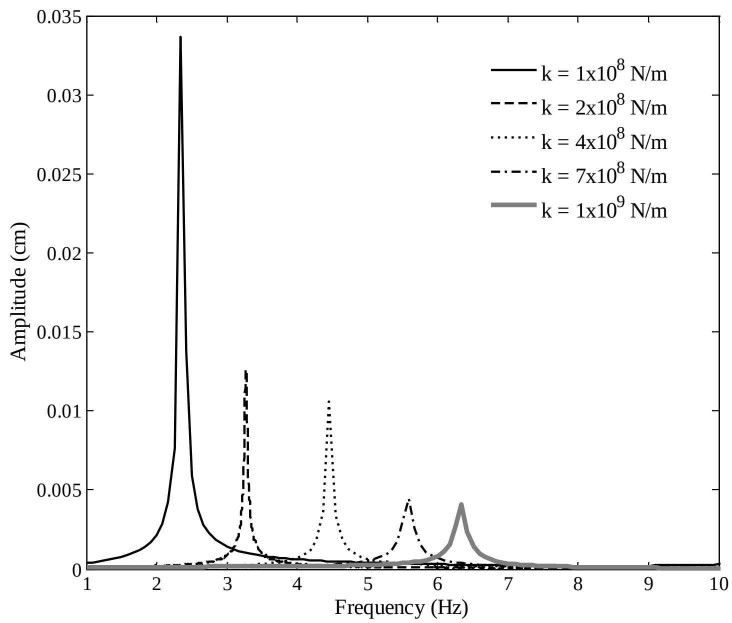

Figure 3.11. FFT spectra of the displacements of the uppermost block of the column, under 5 different values of penalty.

To choose the optimal k value one may resort to previously published recommendations and examine them in light of new findings reported here. Shi in his user's manual (Shi, 1996a) recommends that $k = E*L$ where E is Young's modulus and L is the average block diameter. In the multi drum column problem modeled here E = 17 GPa and L = 0.6 m, yielding a recommended k value by Shi of $1x10^{10}$ N/m , whereas the best fit penalty value found in this study is 1.5 orders of magnitude lower (see Table 3-3). Using the recommended k value by Shi would lead to instability of the solution with the Δ selected (see Table 3-2). The reason for the low best-fit penalty value with respect to Shi's recommendation could be related to the condition of the interface, its roughness, and the presence of some infilling material between the drums.

An interesting note to be made here is that in a previous study performed by the author (Yagoda-Biran and Hatzor, 2010) it was also found that while the recommended penalty value by Shi for a monolithic column studied there was $1.8*10^9$ N/m, the best fit between DDA and the analytical solution for the rocking column problem (Makris and Roussos, 2000) was obtained with a penalty parameter of $8.3*10^7$ N/m, also some two orders of magnitude lower than recommended by Shi.

3.5 Summary and Conclusions

The ability of 2D-DDA to perform site response analysis is examined in this chapter. A multi drum column from the World Heritage Site of Avdat is modeled with 2D-DDA, and its dynamic response is compared with experimental data obtained in a geophysical site response survey conducted at the site. Results indicate that DDA returns a resonance frequency range that is very close to the value obtained experimentally. It was found that the contact spring stiffness, or penalty value, has a great effect on both the resonance frequency as well as the amplitude obtained by DDA. The numerically obtained resonance frequency was found to increase with increasing penalty value whereas its amplitude decreases, as would be expected intuitively. The optimal k value as obtained by comparison between DDA and the geophysical experiment is found to be $k = (1/25)(E*L)$, much lower than recommended by Shi. Perhaps this result reflects the softness of the physical column in reality due to the interfaces between drums which contain some infilling materials. The dominant frequency is found to be independent of the time step size.

4. A new failure mode chart for toppling and sliding with consideration of earthquake inertia force

4.1 Introduction

Rock slope failures involving single plane sliding or toppling have been studied extensively in the past. The problem has typically been formulated for the case of a block on an inclined plane. The model of a block on an inclined plane can help simulate many problems in rock slope engineering: it can be used to represent finite rock blocks formed by intersections of steeply inclined joints and shallowly inclined bedding planes and thus it can sometimes be used to simulate landslides or rock slides. The simplicity of the model and its attractive applicability calls for development of analytical solutions, as these are quite useful in practice.

A block on an incline has four different possible modes of failure (consider Figure 4.1): 1) static stability, 2) downslope sliding, 3) toppling and sliding simultaneously and 4) rotation and toppling. The failure mode is controlled by the geometry of both the block and the inclined plane, and the frictional resistance of the interface between them, the three of which are defined by three angles as follows (see Figure 4.1): δ – the block aspect angle defined by the ratio of the block width b and height h, α – the inclination angle of the slope, will be referred to herein as the slope angle, and ϕ – the friction angle of the interface between the slope and the block. Any combination of these three angles will determine whether the block will move or not, and if so, what will be the mode of its first motion. Clearly, correct assessment of the failure mode is a prerequisite for correct risk assessment and sound support design.

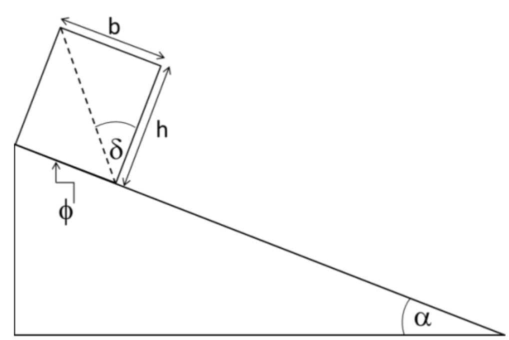

Figure 4.1. Sign convention for the block on an inclined plane model used in this paper.

Ashby (1971) and Hoek and Bray (1977) derived and plotted the modes of failure for the case of block on an incline in δ - α space using static limit equilibrium analysis (LEA). Static LEA implies finding the forces acting on the block at a state of limiting equilibrium, namely, before imminent failure. Ashby's (1971) and Hoek and Bray's (1977) chart is presented in Figure 4.2.

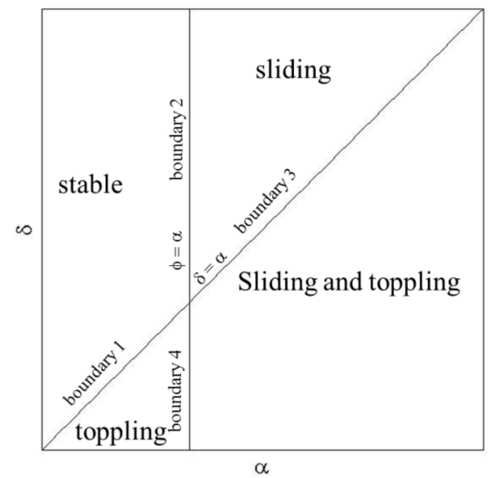

Figure 4.2. Kinematic conditions for sliding and toppling for a block on an inclined plane – static analysis. (after Ashby, 1971).

According to results of the static LEA performed by Ashby (1971) and Hoek and Bray (1977), when $\alpha < \phi$ the block will either be stable ($\delta > \alpha$) or topple ($\delta < \alpha$). When $\alpha > \phi$ the block will either slide ($\delta > \alpha$), or slide and topple simultaneously ($\delta < \alpha$). The original boundaries between those failure modes are assigned numbers here (see Figure 4.2); these numbers will be referred to herein when discussing failure mode boundaries.

Voegele (1979) compared the analytical results with distinct element method (DEM) simulations and discovered that in some cases while the block should have failed in sliding and toppling according to the mode chart in Figure 4.2, in fact it experienced sliding alone when studied with DEM. Thus, he concluded that the Hoek and Bray (1977) chart was too elementary to predict the exact dynamic behavior of slender blocks resting on an inclined plane.

Bray and Goodman (1981) revisited this problem and treated boundary 3 in Figure 4.2 as a "dynamic" boundary. Their approach changed the condition for sliding to $\alpha > \phi$, and $\delta \geq \phi$ (see

Figure 4.3). Yu et al. (1987) later found that results of DEM simulations and physical models agree with Bray and Goodman's (1981) modified chart.

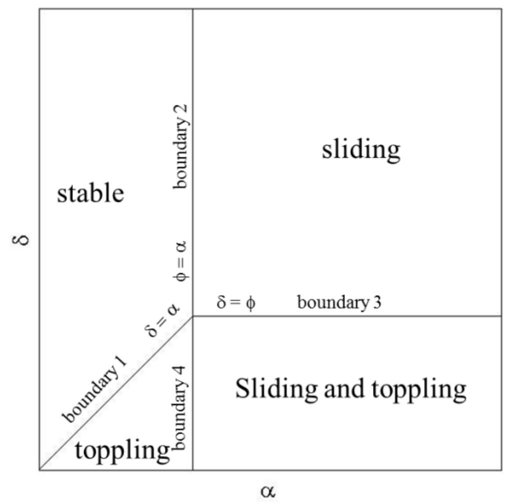

Figure 4.3. Kinematic conditions for sliding and toppling with the modified boundary 3. After Bray and Goodman (Bray and Goodman, 1981).

Sagaseta (1986) argued that Bray and Goodman's modification is correct but incomplete because at boundary 4 the state of equilibrium is dynamic rather than static; the derivation of the equilibrium equations for that boundary are provided in his paper. Yeung (1991) studied this problem with two dimensional Discontinuous Deformation Analysis method (2D-DDA, (Shi, 1988, 1993; Shi and Goodman, 1985 ; Shi and Goodman, 1989)) and compared his results to the chart published by Bray and Goodman (1981). He discovered that while 2D-DDA results agree with the first three boundaries, reassuring the modification of Bray and Goodman (1981) to boundary 3, there is a discrepancy between the results obtained by 2D-DDA and the behavior predicted by boundary 4 in Bray and Goodman's chart. In some cases, while Bray and Goodman's chart predicts sliding and toppling, DDA results suggest toppling only. This led Yeung (1991) to treat boundary 4 as a dynamic boundary as well. The analytical solution for boundary 4 as derived by Yeung (1991) is presented in the next paragraph , with incorporation of dynamic effects into the solution.

When a block is on the verge of toppling, the hinge (center of rotation, see Figure 4.4) tends to move upslope. This movement may prevent sliding, even when permissible by virtue of kinematics, namely when $\phi < \alpha$. Boundary 4 distinguishes between toppling with and without sliding, therefore the analytical solution derived by Yeung (1991) assumes limiting friction ($\phi = \alpha$). Figure 4.4 schematically describes the state of forces acting on the block at boundary 4.

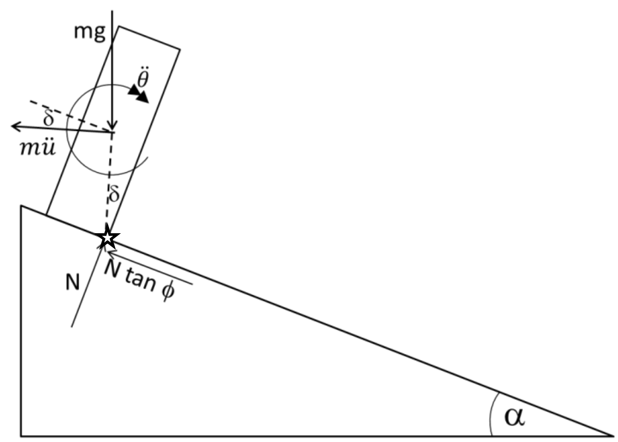

Figure 4.4. The dynamics of the block at boundary 4. The block is toppling, hence it has rotational acceleration from which linear acceleration $\ddot{u}$ is derived, and is on the verge of sliding. The rotation hinge is marked with a star. After Yeung (1991).

When the block is toppling and at the onset of sliding, it is under pure rotation, therefore its angular acceleration $\ddot{\theta}$ at the hinge and at the centroid are identical. The forces acting on the block are its weight *mg*, acting at the centroid, the normal from the incline *N*, and the limiting friction force $N\tan\phi$, both acting at the hinge.

Applying Newton's second law, both parallel and perpendicular to the slope, and taking moments about the centroid of the block, three equations with four variables ($\ddot{\theta}$, $\ddot{u}$, ϕ and N) can be written:

$$mg\sin\alpha - N\tan\phi = m\ddot{u}\cos\delta \quad \text{Equation 4-1}$$

$$N - mg\cos\alpha = m\ddot{u}\sin\delta \quad \text{Equation 4-2}$$

$$N\tan\phi\frac{h}{2} - N\frac{b}{2} = \frac{1}{12}m\left(h^2 + b^2\right)\ddot{\theta} \quad \text{Equation 4-3}$$

The fourth equation relates $\ddot{\theta}$ and $\ddot{u}$:

$$\ddot{u} = \frac{1}{2}\ddot{\theta}\sqrt{h^2 + b^2} \qquad \text{Equation 4-4}$$

Solving the set of equations yields the following equation for a friction angle satisfying boundary 4, with any combination of α and δ:

$$\tan\phi = \frac{3\sin\delta\cos(\alpha-\delta)+\sin\alpha}{3\cos\delta\cos(\alpha-\delta)+\cos\alpha} \qquad \text{Equation 4-5}$$

or:

$$\tan\alpha = \frac{3\cos^2\delta\tan\phi - 3\sin\delta\cos\delta + \tan\phi}{3\sin^2\delta - 3\sin\delta\cos\delta\tan\phi + 1} \qquad \text{Equation 4-6}$$

A modified chart for the different modes after correction of boundary 4 for dynamic LEA is presented in Figure 4.5 following Yeung (1991), for the case of ϕ = 30°. With the modified boundary 4 Yeung obtained good agreement between 2D-DDA and the modified kinematic chart.

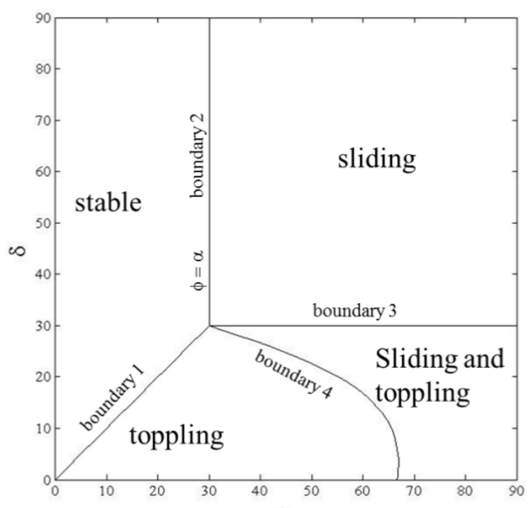

Figure 4.5. Kinematic conditions for sliding and toppling with modified boundary 4, for ϕ = 30°. After Yeung (1991).

In a classic paper, Goodman and Bray (1976) further developed a static LEA solution for the toppling failure of multiple blocks, where the slope is represented by a series of blocks resting on a stepped basal discontinuity. They distinguished between three modes: block toppling, flexural toppling, and both block and flexural toppling. Following Goodman and Bray, flexural toppling and block toppling have been further investigated by many groups, both analytically (Amini et al., 2009; Amini et al., 2012; Aydan and Kawamoto, 1992; Bobet, 1999; Liu et al., 2008; Majdi and Amini, 2011; Sagaseta et al., 2001), experimentally (Adhikary et al., 1997; Amini et al., 2009) and numerically (Bobet, 1999; Brideau and Stead, 2010; Scholtes and Donze, 2012). The mode of block slumping has also been studied analytically and numerically by Kieffer (1998).

4.2 Three dimensional visualization of the kinematic mode chart

In the introduction section it was shown that the mode of failure of a single block on an incline depends on three variables: the angles α, ϕ and δ. A three dimensional representation of the mode chart is therefore called for, as presented in Figure 4.6. The 3D space, the three axes of which are the three angles, is divided into the four regions of block behavior, namely Mode 1 – stable, Mode 2 – sliding, Mode 3 – sliding and toppling, and Mode 4 – toppling. Consider Figure 4.6a, the different failure modes are plotted as follows:

Mode 1, the stable mode, is above the red surface (delineating the $\alpha = \delta$ surface) and to the left of the blue surface (delineating the $\alpha = \phi$ surface*)*.

Mode 2, the sliding mode, is above the green surface (delineating the $\phi = \delta$ surface) and to the right of the blue surface (delineating the $\alpha = \phi$ surface).

Mode 3, the sliding and toppling mode, is below the green surface, indicating the $\phi = \delta$ surface, and in front of the curved surface representing Eq. 4.6 (note that in this view the curved surface is actually behind the green surface).

Mode 4, or the toppling mode, is below the red surface, indicating $\alpha = \delta$, and behind the curved surface representing Eq. 4.6.

Figure 4.6a presents the 3D space from a point of view similar to those of Figures 4.2, 4.3 and 4.5 but for different values of ϕ. In Figure 4.6b the mapped 3D boundaries are viewed from vector (-1, -1, -1). When using (-1, -1, -1) as a viewing vector, vector (1, 1, 1) is reduced to a point, and the surfaces separating the different modes are reduced to lines. With this mapping the 3D space appears as a 2D space where it is easier to perceive the boundaries between the four modes.

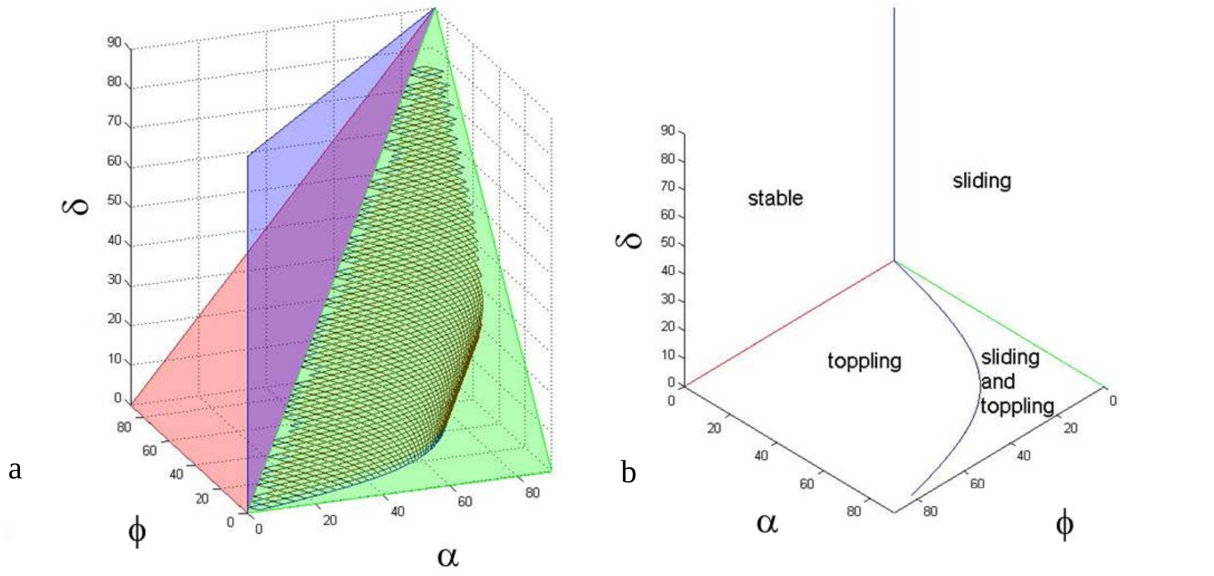

Figure 4.6. Kinematic conditions for toppling and sliding. a) a point of view similar to Figures 4.2, 4.3 and 4.5. b) Isometric point of view, viewing vector (-1, -1, -1).

4.3 Adding pseudo-static inertia force to toppling analysis

When trying to determine stability and failure mode under seismic conditions, a common practice in geotechnical engineering is to impose a static force, acting at the centroid of the block, in order to simulate the inertia force of an earthquake at a certain moment during the dynamic earthquake vibration. Typically, the peak ground acceleration (*PGA*) of the earthquake record is converted into a pseudo-static horizontal force *F* acting at the centroid, normalized by the block weight *W*, hence the earthquake acceleration coefficient *k* is defined, i.e. $F = kW$. Figure 4.7 illustrates the schematics of the block on an incline problem with a horizontal static force *F*.

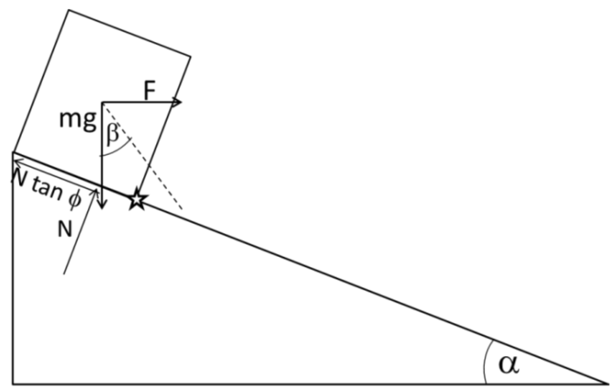

Figure 4.7. Force diagram for a block on an incline with pseudo- static force *F*. The hinge of rotation is marked by a star.

When adding the pseudo-static force *F*, a new angle β is introduced, defined here as the angle between the block self-weight *W* and the resultant of force *F* and block self-weight *W* (see Figure 4.7), namely:

$$\tan\beta = \frac{F}{W} = k \qquad \text{Equation 4-7}$$

In this section a mode analysis for the block on an incline problem with horizontal force $F = kW$ is derived.

Boundary 1: between toppling and stable modes

The forces acting on the block at this boundary are *W, F, N* and the frictional resistance. At the onset of toppling the normal and the frictional forces act at the hinge, therefore they do not contribute to the moments acting on the block. In order for the block to remain stable against toppling, the line of action of the resultant of *F* and *W* must pass through the hinge, this way producing no moments as well. In other words, the stabilizing moments have to be equal to the driving moments at a state of limiting equilibrium:

$$\frac{1}{2}bW\cos\alpha = \frac{1}{2}hW\sin\alpha + \frac{1}{2}hF\cos\alpha + \frac{1}{2}bF\sin\alpha \qquad \text{Equation 4-8}$$

Inserting the definition of β into Eq. 4.8 yields:

$$\frac{b}{h} = \frac{\sin\alpha + \cos\alpha\tan\beta}{\cos\alpha - \sin\alpha\tan\beta} = \frac{\tan\alpha + \tan\beta}{1 - \tan\alpha\tan\beta} = \tan(\alpha + \beta) \quad \text{Equation 4-9}$$

Therefore at the point of limiting equilibrium with respect to toppling:

$$\delta = \alpha + \beta \quad \text{Equation 4-10}$$

If $\delta < \alpha + \beta$, the block will topple.

If $\delta > \alpha + \beta$, the block will be stable.

Boundary 2: between sliding and stable modes

At the point of imminent sliding, friction is limiting, therefore the force preventing sliding at the point of limiting equilibrium with respect to sliding is $N\tan\phi$.

Force equilibrium parallel to the sliding direction yields:

$$N\tan\phi = F\cos\alpha + W\sin\alpha \quad \text{Equation 4-11}$$

Force equilibrium perpendicular to the sliding direction yields:

$$N = W\cos\alpha - F\sin\alpha \quad \text{Equation 4-12}$$

Inserting Eq. 4.12 into Eq. 4.11, and using results from Eq. 4.9, yields:

$$\tan\phi = \frac{F\cos\alpha + W\sin\alpha}{W\cos\alpha - F\sin\alpha} = \frac{\sin\alpha + \cos\alpha\tan\beta}{\cos\alpha - \sin\alpha\tan\beta} = \tan(\alpha + \beta) \quad \text{Equation 4-13}$$

Therefore the limiting condition for sliding is $\phi = \alpha + \beta$.

Boundary 3: between sliding and sliding + toppling modes

Bray and Goodman (1981) treated boundary 3 as a dynamic one, since the block is both sliding and on the verge of toppling.

According to Newton's second law, the force equilibrium in the downslope direction is:

$$F\cos\alpha + W\sin\alpha - N\tan\phi = m\ddot{u} \quad \text{Equation 4-14}$$

Force equilibrium perpendicular to the slope yields:

$$N = W\cos\alpha - F\sin\alpha \qquad \text{Equation 4-15}$$

Finding $\ddot{u}$ from Eq. 4.14 and 4.15, and using Eq. 4.7:

$$m\ddot{u} = F\cos\alpha + W\sin\alpha - \tan\phi(W\cos\alpha - F\sin\alpha) = W[\tan\beta\cos\alpha + \sin\alpha - \tan\phi(\cos\alpha - \tan\beta\sin\alpha)]$$

Equation 4-16

Since the block is on the verge of rotating, the sum of moments about the hinge is (see Figure 4.7):

$$\frac{h}{2}F\cos\alpha + \frac{b}{2}F\sin\alpha + \frac{h}{2}W\sin\alpha = \frac{b}{2}W\cos\alpha + \frac{h}{2}m\ddot{u} \qquad \text{Equation 4-17}$$

Substituting Eq. 4.16 into Eq. 4.17 yields:

$$b/h = \tan\phi \qquad \delta = \phi \qquad \text{Equation 4-18}$$

Therefore, the limiting condition for dynamic equilibrium for boundary 3 is $\delta = \phi$.

Boundary 4: between toppling and sliding + toppling modes

Yeung (1991) treated boundary 4 as a dynamic boundary because at this boundary the block is toppling and on the verge of sliding.

According to Newton's second law, force equilibrium in the downslope direction yields:

$$F\cos\alpha + W\sin\alpha - N\tan\phi = m\ddot{u}\cos\delta \qquad \text{Equation 4-19}$$

and the force equilibrium perpendicular to the slope yields:

$$F\sin\alpha + N - W\cos\alpha = m\ddot{u}\sin\delta \qquad \text{Equation 4-20}$$

Taking moments about the centroid (since at the onset of sliding the angular acceleration is uniform about the block) will again yield Eq. 4.3. Solving Eq. 4.3, 4.4, 4.19 and 4.20 yields:

$$\tan\phi = \frac{3\sin\delta\cos[\delta - (\alpha+\beta)] + \sin(\alpha+\beta)}{3\cos\delta\cos[\delta - (\alpha+\beta)] + \cos(\alpha+\beta)} = \frac{3\sin\delta\cos(\delta-\psi) + \sin\psi}{3\cos\delta\cos(\delta-\psi) + \cos\psi} \qquad \text{Equation 4-21}$$

The complete derivation of boundary 4 is provided in appendix A.

To summarize, in the case where a horizontal force of magnitude $F = kW$ acts on the centroid of the block, the boundaries of the failure modes become a function of three angles: ϕ, δ and $\boldsymbol{\psi = \alpha + \beta}$, instead of α for the case of gravitational loading alone. Alternatively, if using k instead of β is preferable, then

$$\psi = \tan^{-1}\frac{k+\tan\alpha}{1-k\tan\alpha} \qquad \text{Equation 4-22}$$

4.4 Verification of the dynamic toppling and sliding boundaries with DDA

As mentioned earlier, Yeung (1991) verified the 2D-DDA with the analytical solutions of mode analysis under gravitational loading. He found that 2D-DDA results agreed well with the analytical solution for sliding or toppling and utilized the DDA results to modify the dynamic boundary between toppling and sliding + toppling (boundary 4) . Here both 2D and 3D-DDA are used to verify the pseudo-static analysis which considers an additional inertia force. DDA basics will not be reviewed here as they were thoroughly discussed in Chapter 2 of the thesis.

The 3D-DDA code is relatively new, and has not been extensively verified as the 2D-DDA code. Thus we begin with verification of 3D-DDA using the existing analytical solution for the four failure modes of the block on an incline problem, in section 4.4.1. Once verified, we use 2D and 3D-DDA to confirm our modified boundaries which also consider pseudo-static loading, in sections 4.4.2 and 4.4.3, respectively.

The block and the incline are modeled in the DDA, and a measurement point, of which displacements and rotations are documented throughout the simulations, is placed at the hinge (see Figure 4.7). The displacements and rotations of the measurement point for the first 0.5 sec of the simulation are then examined, and their values determine the nature of the failure mode. It is important to state here that in DDA the rotations are uniform throughout the block, because of the first order approximation.

The following criteria are adopted to judge the obtained failure mode from DDA output:

- The block is considered *stable* if the recorded displacements at the measurement point are less than 0.001 m and are arrested, and if the rotation is less than 0.0001 radians.

- The block is *sliding* if the displacements are more than 0.001 m and the block accelerates, and if the rotation is less than 0.0001 radians.
- The block is *toppling* if the displacements are less than 0.001 m, but the rotation is more than 0.0001 radians.
- The block is *sliding and toppling* if both the displacement is larger than 0.001 m and the rotation is larger than 0.0001 radians

A flow chart describing the failure mode judgment criteria for DDA output is presented in Figure 4.8.

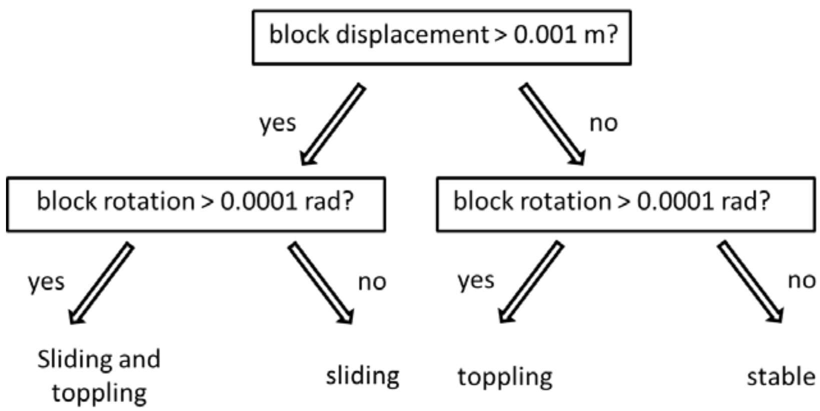

Figure 4.8. Flow chart describing criteria for determination of failure mode in numerical simulations

4.4.1 Verification of 3D-DDA with mode analysis charts under gravitational loading

The numerical and physical parameters used in the verification study of the 3D-DDA are presented in Table 4-1. For the sake of comparison with the original verification study performed by Yeung (1991) the control parameters used in his analysis are provided in Table 4-2.

Table 4-1. Numerical and physical parameters used for 3D-DDA verification study

Parameter	**Value**
Static-dynamic parameter *dd*	1 (fully dynamic)
Normal contact spring stiffness *g0*	$1x10^9$ N/m
Maximum time step interval *g1*	0.00001 sec.
Maximum displacement ratio *g2*	0.0001
Density	2730 kg/m^3
Young’s modulus	42.9 GPa
Poisson’s ratio	0.18

Table 4-2. Numerical and physical parameters used for 2D-DDA verification study by Yeung (1991)

Parameter	**Value**
Static-dynamic parameter *dd*	0 (fully static)
Normal contact spring stiffness *g0*	$1x10^{10}$ N/m
Maximum time step interval *g1*	0.05 sec.
Maximum displacement ratio *g2*	0.005
Density	3000 kg/m^3
Young's modulus	10 GPa
Poisson's ratio	0.49

As can be observed from Tables 4-1 and 4-2, the density and Young's modulus are of the same order of magnitude, whereas the time step interval and the normal contact spring stiffness in 3D-DDA are three and one orders of magnitude lower, respectively. The normal contact spring stiffness, or *k*, selected for the verification study is between (1/6) to (1/26) $E*L$, where E is Young's modulus and L is the average block diameter, the value recommended by Shi.

The friction angle selected for the study was 20^o in most analyses. The list of analyses performed in the verification study is provided in Table 4-3,and projection of the results on the three-dimensional mode chart is presented in Figure 4.9. The agreement between the 3D-DDA and the analytical solution is excellent.

Table 4-3. Analytical mode analysis vs. 3D-DDA results for gravitational loading

α	ϕ	δ	**mode predicted by analytical solution**	**mode obtained by DDA**
15	20	14	toppling	toppling
15	20	14.4	toppling	toppling
15	20	14.8	toppling	toppling
15	20	15.2	stable	stable
15	20	15.6	stable	stable
15	20	16	stable	stable
15	20	30	stable	stable
15	20	50	stable	stable
15	20	70	stable	stable
40	20	19	sliding + toppling	sliding + toppling
40	20	19.8	sliding + toppling	sliding + toppling
40	20	20.2	sliding	sliding
40	20	21	sliding	sliding
40	20	30	sliding	sliding
14	20	15	stable	stable

14.8	20	15	stable	stable
15.2	20	15	toppling	toppling
15.6	20	15	toppling	toppling
16	20	15	toppling	toppling
30	20	15	toppling	toppling
40	20	15	sliding + toppling	sliding + toppling
50	20	15	sliding + toppling	sliding + toppling
10	20	50	stable	stable
19	20	50	stable	stable
19.8	20	50	stable	stable
20.2	20	50	sliding	stable
20.6	20	50	sliding	stable
21	20	50	sliding	sliding
30	20	50	sliding	sliding
40	20	50	sliding	sliding
50	20	50	sliding	sliding
30	40	30.96	stable	stable
10	20	30.96	stable	stable
50	60	56.31	stable	stable
30	5	11.31	sliding	sliding
10	5	8.53	sliding	sliding
50	45	56.31	sliding	sliding
30	40	11.31	toppling	toppling
10	20	8.53	toppling	toppling
50	60	38.66	toppling	toppling
50	45	38.66	toppling	toppling
30	30	11.3	sliding + toppling	sliding + toppling
10	9	8.53	sliding + toppling	sliding + toppling
22	20	50	sliding	sliding
20.8	20	50	sliding	sliding
15	20	10	toppling	toppling
22	20	10	toppling	toppling
30	20	11.31	toppling	toppling
37	20	11.31	toppling	toppling
37	20	15	toppling	toppling
22	20	18	toppling	toppling

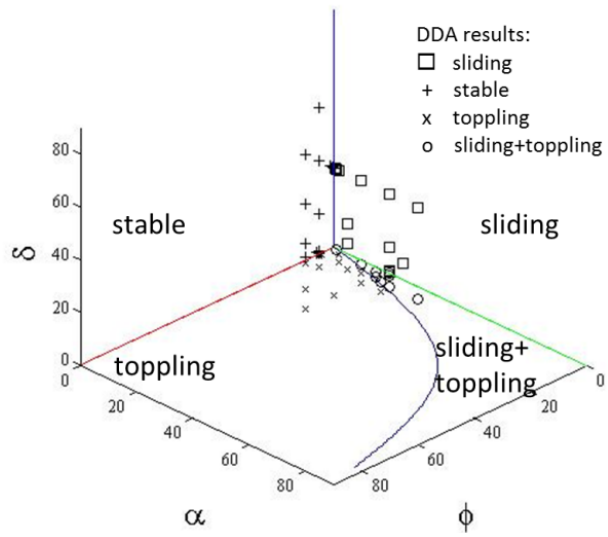

Figure 4.9. Results of 3D-DDA verification analysis with the analytical solution.

4.4.2 Verification of the mode analysis charts with 2D-DDA for pseudo-static force

The 2D-DDA has been verified many times in the past, and has proved to be a useful and reliable tool for numerical modeling of discontinuous problems in geomechanics and rock mechanics (e.g. Kamai and Hatzor, 2008; MacLaughlin and Doolin, 2006; Yagoda-Biran and Hatzor, 2010). Therefore we use the 2D-DDA to confirm the analytical solution derived for a block on an incline subjected to gravity and a horizontal pseudo-static force. The physical and numerical parameters used in the 2D-DDA simulations are presented in Table 4-4. The time step size that can be used in the 2D-DDA is 100 times larger than the one used in 3D-DDA, and the spring stiffness is identical to the value used by Yeung (1991) (see Table 4-2), and is between 0.4 and 1.7 of $E*L$ (depending on the size of the sliding block, determining δ), the value recommended by Shi (1996a).

Table 4-4. Physical and numerical control parameters used in the 2D-DDA with external force *F*

Parameter	**Value**
Static-dynamic parameter *dd*	1 (fully dynamic)
Normal contact spring stiffness *g0*	1×10^{10} N/m
Maximum time step interval *g1*	0.001 sec.
Maximum displacement ratio *g2*	0.001
Density	2730 kg/m^3
Young's modulus	42.9 GPa
Poisson's ratio	0.18

Since the addition of an external force F introduces a new angle to the mode chart, the angle $\psi = \alpha+\beta$, different values for ψ can be generated by changing β (through a change in F) without changing α. This allows for fast modeling and multiple simulations using the same DDA mesh. The α used in the verification study was 10^{o}. Table 4-5 lists the different simulations and their results for the 2D-DDA verification.

Table 4-5. Analytical mode analysis vs. 2D-DDA with horizontal force F

$\psi\ (\alpha+\beta)$	ϕ	δ	**Mode predicted by analytical solution**	**Mode obtained by DDA**
29	35	30.96	stable	stable
29.5	35	30.96	stable	stable
30	35	30.96	stable	stable
30.5	35	30.96	stable	stable
30.9	35	30.96	stable	stable
31	35	30.96	toppling	toppling
31.5	35	30.96	toppling	toppling
32	35	30.96	toppling	toppling
32.5	35	30.96	toppling	toppling
30	50	30.96	stable	stable
30.5	50	30.96	stable	stable
30.9	50	30.96	stable	stable
31	50	30.96	toppling	toppling
31.5	50	30.96	toppling	toppling
32.5	50	30.96	toppling	toppling
18	20	30.96	stable	stable
18.5	20	30.96	stable	stable
19	20	30.96	stable	stable
19.5	20	30.96	stable	stable
19.8	20	30.96	stable	stable
20.2	20	30.96	sliding	sliding
21	20	30.96	sliding	sliding
21.5	20	30.96	sliding	sliding
22	20	30.96	sliding	sliding
48	50	30.96	toppling	toppling
49.8	50	30.96	toppling	toppling
52	50	30.96	toppling	toppling
35	30	30.96	sliding	sliding + toppling
36	30	30.96	sliding	sliding
35	29	30.96	sliding	sliding
35	25	30.96	sliding	sliding
40	30	30.96	sliding	sliding
45	30	30.96	sliding	sliding
50	30	30.96	sliding	sliding
60	30	30.96	sliding	sliding

70	30	30.96	sliding	sliding
80	20	30.96	sliding	sliding
85	40	30.96	sliding + toppling	sliding + toppling
66	40	30.96	sliding + toppling	sliding + toppling
64	40	30.96	sliding + toppling	sliding + toppling
62	40	30.96	toppling	toppling
80	40	30.96	sliding + toppling	sliding + toppling
82	50	30.96	toppling	toppling
84	50	30.96	toppling	sliding + toppling
86	50	30.96	sliding + toppling	sliding + toppling
80	60	30.96	toppling	toppling
70	10	30.96	sliding	sliding
70	20	30.96	sliding	sliding
70	40	30.96	sliding + toppling	sliding + toppling
70	50	30.96	toppling	toppling
20	21	20.30	stable	toppling
20	21	30.96	stable	stable
20	21	40.03	stable	stable
20	21	50.19	stable	stable
20	21	60.11	stable	stable
20	21	71.57	stable	stable
20	19	20.30	sliding	sliding
20	19	30.96	sliding	sliding
20	19	40.03	sliding	sliding
20	19	50.19	sliding	sliding
20	18.9	60.11	sliding	sliding
20	19	71.57	sliding	sliding
20	80	20.30	stable	stable
30	80	30.96	stable	stable
40	80	40.70	stable	stable
50	80	50.19	stable	stable
60	80	60.40	stable	stable
70	80	70.35	stable	stable
20	80	19.80	toppling	toppling
30	80	29.25	toppling	toppling
40	80	39.35	toppling	toppling
50	80	49.24	toppling	toppling
60	80	59.53	toppling	toppling
70	80	69.68	toppling	toppling
10	5.8	6.84	sliding	sliding
20	6	6.84	sliding	sliding
30	16	16.70	sliding	sliding
40	26	26.57	sliding	sliding
50	35	35.75	sliding	sliding
60	43	43.53	sliding	sliding
70	54	54.46	sliding	sliding
80	63	63.43	sliding	sliding

10	8	6.84	sliding + toppling	sliding + toppling
20	8	6.84	sliding + toppling	sliding + toppling
30	17	16.70	sliding + toppling	sliding + toppling
40	27	26.57	sliding + toppling	sliding + toppling
50	36	35.75	sliding + toppling	sliding + toppling
60	44	43.53	sliding + toppling	sliding + toppling
70	55	54.46	sliding + toppling	sliding + toppling
80	64	63.43	sliding + toppling	sliding + toppling
20	10	7.07	sliding + toppling	sliding + toppling
30	20	17.22	sliding + toppling	sliding + toppling
40	20	12.95	sliding + toppling	sliding + toppling
50	20	7.07	sliding + toppling	sliding + toppling
60	40	33.02	sliding + toppling	sliding + toppling
70	50	42.92	sliding + toppling	sliding + toppling
80	62	53.06	toppling	sliding + toppling
20	10	6.05	toppling	toppling
30	20	16.17	toppling	toppling
40	20	11.97	toppling	toppling
50	20	6.05	toppling	toppling
60	40	32.05	toppling	toppling
70	50	41.99	toppling	toppling
80	62	52.00	toppling	toppling
18	30	29.00	stable	stable
50	30	29.00	sliding + toppling	sliding + toppling
40	30	29.00	sliding + toppling	sliding + toppling
35	30	29.00	sliding + toppling	sliding + toppling
32	30	29.00	toppling	toppling
50	35	29.00	toppling	toppling

In Figure 4.10 snapshots from two 2D-DDA simulations under pseudo-static force are presented. Note that a small increase in the friction angle is sufficient for changing the failure mode.

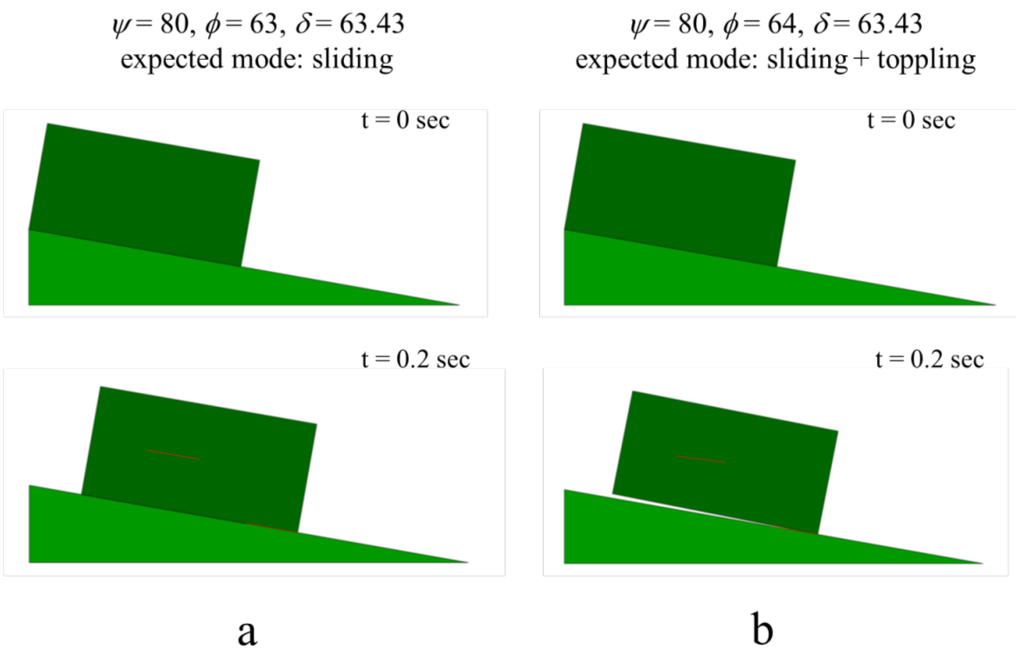

Figure 4.10. Snapshots from two simulations separated by boundary 3, i.e. a) sliding and b) sliding+toppling. Note the slight increase in ϕ between the two simulations, that results in a different failure mode.

Figure 4.11 presents the results of the 2D-DDA simulations with external force F in the ψ, ϕ and δ space. Note the excellent agreement between the numerical DDA and analytical solutions.

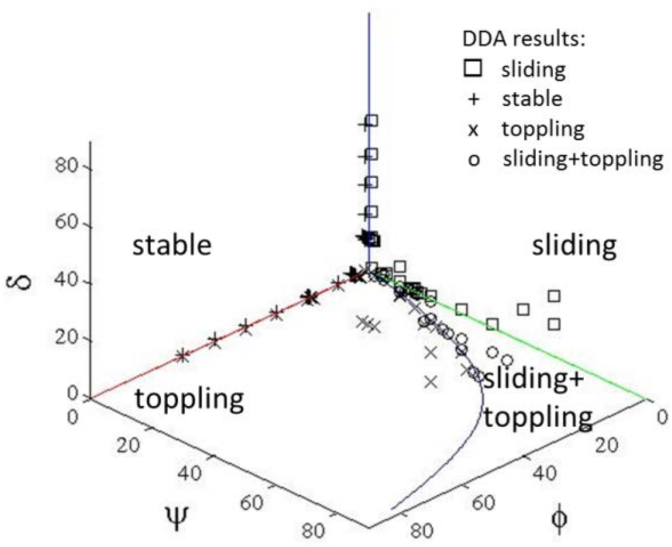

Figure 4.11. Results of 2D-DDA verification analysis with the analytical solution, with application of external force.

As mentioned before, DDA simulations were performed with a fixed inclination angle of 10^o, and the angle ψ was altered by the force F. A few simulations were performed with different inclination angles, to make sure results of the simulations are repeated, and the results confirmed the modeling assumption made here for simplicity.

4.4.3 Verification of the mode analysis charts with 3D-DDA for pseudo-static force

A similar process of verification was performed with the 3D-DDA. The physical and numerical control parameters are identical to the ones used in the gravitational loading verification in section 4.4.1, and are listed in Table 4-1. In Figure 4.12 snapshots from two 3D-DDA simulations under pseudo-static force are presented.

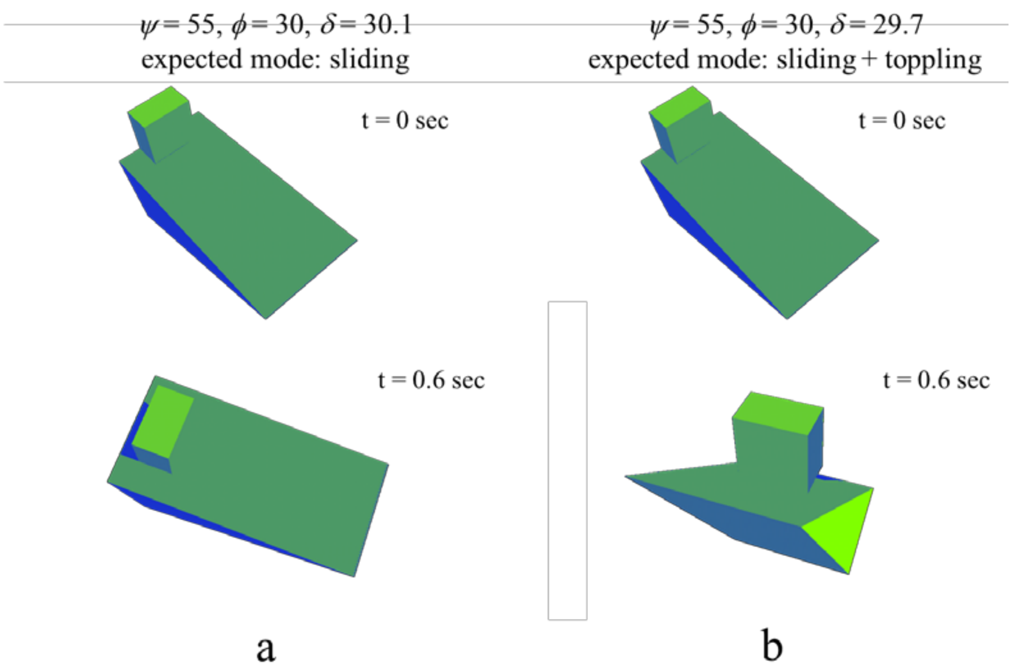

Figure 4.12. Snapshots from two simulations separated by boundary 3, i.e. a) sliding and b) sliding+toppling. Note the small difference in δ that results in a different failure mode. The late snapshots were taken from an advanced stage of the simulation, in order for the deformation to be visible.

The analyses performed in this section are listed in Table 4-6, and results are plotted in Figure 4.13. Note the good agreement between the analytical solution and the 3D-DDA.

Table 4-6. Analytical mode analysis vs. 3D-DDA with horizontal force *F*

ψ $(\alpha+\beta)$	ϕ	δ	**mode predicted by analytical solution**	**mode obtained by DDA**
29	80	30.96	stable	stable
29.5	80	30.96	stable	stable
30	80	30.96	stable	stable
30.5	80	30.96	stable	stable
30.9	80	30.96	stable	stable
31	80	30.96	toppling	toppling
31.5	80	30.96	toppling	toppling
32	80	30.96	toppling	toppling
32.5	80	30.96	toppling	toppling
33	80	30.96	toppling	toppling
27	28	30.96	stable	stable
27.5	28	30.96	stable	stable
27.8	28	30.96	stable	stable
28.2	28	30.96	sliding	sliding
28.5	28	30.96	sliding	sliding
29	28	30.96	sliding	sliding
60	40	30.96	toppling	toppling
60.5	40	30.96	toppling	toppling
61	40	30.96	toppling	toppling
61.5	40	30.96	toppling	toppling
62	40	30.96	toppling	toppling
62.5	40	30.96	toppling	toppling
63	40	30.96	toppling	toppling
63.5	40	30.96	sliding + toppling	sliding + toppling
64	40	30.96	sliding + toppling	sliding + toppling
64.5	30	30.96	sliding + toppling	sliding + toppling
65	30	30.96	sliding + toppling	sliding + toppling
65.5	30	30.96	sliding + toppling	sliding + toppling
55	30	30.96	sliding	sliding
55	30	30.54	sliding	sliding
55	30	30.11	sliding	sliding
55	30	29.68	sliding + toppling	sliding + toppling
55	50	19.80	toppling	toppling
20	21	20.30	toppling	toppling
20	21	30.96	stable	stable
20	21	40.03	stable	stable
20	21	50.19	stable	stable
20	21	60.11	stable	stable
20	21	71.57	stable	stable
20	19	20.30	sliding	sliding
20	19	30.96	sliding	sliding
20	19	40.03	sliding	sliding
20	19	50.19	sliding	sliding

20	18.9	60.11	sliding	sliding
20	19	71.57	sliding	sliding
20	80	20.30	stable	stable
30	80	30.96	stable	stable
40	80	40.70	stable	stable
50	80	50.19	stable	stable
60	80	60.40	stable	stable
70	80	70.35	stable	stable
20	80	19.80	toppling	toppling
30	80	29.25	toppling	toppling
40	80	39.35	toppling	toppling
50	80	49.24	toppling	toppling
60	80	59.53	toppling	toppling
70	80	69.68	toppling	toppling
10	5.8	6.84	sliding	sliding
20	6	6.84	sliding	sliding
30	16	16.70	sliding	sliding
40	26	26.57	sliding	sliding
50	35	35.75	sliding	sliding
60	43	43.53	sliding	sliding
70	54	54.46	sliding	sliding
80	63	63.43	sliding	sliding
10	8	6.84	sliding + toppling	sliding + toppling
20	8	6.84	sliding + toppling	sliding + toppling
30	17	16.70	sliding + toppling	sliding + toppling
40	27	26.57	sliding + toppling	sliding + toppling
50	36	35.75	sliding + toppling	sliding + toppling
60	44	43.53	sliding + toppling	sliding + toppling
70	55	54.46	sliding + toppling	sliding + toppling
80	64	63.43	sliding + toppling	sliding + toppling
20	10	7.07	sliding + toppling	sliding + toppling
30	20	17.22	sliding + toppling	sliding + toppling
40	20	12.95	sliding + toppling	sliding + toppling
50	20	7.07	sliding + toppling	sliding + toppling
60	40	33.02	sliding + toppling	sliding + toppling
70	50	42.92	sliding + toppling	sliding + toppling
80	62	53.06	sliding + toppling	sliding + toppling
20	10	6.05	toppling	toppling
30	20	16.17	toppling	toppling
40	20	11.97	toppling	toppling
50	20	6.05	toppling	toppling
60	40	32.05	toppling	toppling
70	50	41.99	toppling	toppling
80	62	52.00	toppling	toppling
30	80	30.96	stable	stable
30	80	29.25	toppling	toppling

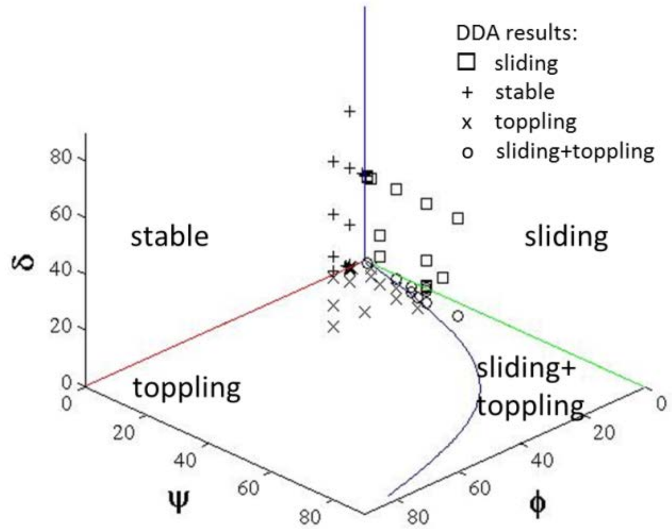

Figure 4.13. Results of 3D-DDA verification analysis with the analytical solution, with application of external force.

4.5 Summary and conclusions

Previous research regarding the problem of a block on an incline is reviewed here. Then, for the first time, the four possible modes (stability, sliding, sliding+toppling and toppling) are mapped in a three dimensional space, as the modes are a function of three angles: the block angle δ (block width / block height), the friction angle of the interface between the slope and the block ϕ, and the inclination of the slope α. Then a new failure mode chart is derived, incorporating the frequently used pseudo-static approach in geotechnical earthquake engineering. The numerical 3D-DDA code is then verified with mode analysis for gravitational loading, and the pseudo-static mode chart, derived here, is confirmed with the 2D and 3D-DDA codes.

In the new chart, derived in this research, the mode of failure of the block is again a function of three angles: δ, ϕ, and a new angle, $\psi = \alpha + \beta$, β being the angle between the resultant of the block weight and the pseudo-static force applied on the block, and the vertical direction. Verification of the 3D-DDA with the formerly derived analytical solution for a block on an inclined plane under gravitational loading alone proves the 3D-DDA can accurately solve the problem. Furthermore, the 2D and 3D DDA simulations of the block subjected to pseudo-static horizontal force confirm the new analytical boundaries derived here, and once again confirm the dynamic nature of boundary 4, which separates toppling from sliding and toppling.

When designing a proper support for rock masses that can be modeled as a block on an incline, it is sometimes crucial to take into account seismic forces that can affect the stability of the rock mass. The new chart for failure modes, with the incorporation of a pseudo-static horizontal force simulating the seismic force of an earthquake, is an easy, more intuitive way to understand and predict the behavior of rock masses subjected to seismic loads, when these are modeled as a pseudo-static horizontal force. When using the new chart, the pseudo-static force for the mode analysis should be carefully selected, taking into account seismic hazard assessments in the region discussed, and preferably site effects, where these are known.

5. Paleo-seismological implications of historic block displacements in the Western Wall Tunnels, the Old City of Jerusalem

5.1 Introduction

After proving that site response analysis is feasible with 2D-DDA in chapter 3, and using the 2D-DDA code for verification of a pseudo-static approach for a block on an inclined plane in chapter 4, in this chapter we will attempt to use the 2D-DDA to constrain paleo peak ground acceleration (*PGA)* values that struck a specific region. We choose to demonstrate the approach on the highly important, from cultural, historical and religious perspective, Western Wall Tunnels complex underneath the foundations of Temple Mount in the Old City of Jerusalem. Constraining paleo *PGA* values in regions where recorded earthquake data is scarce or doesn't exist, like the Old City of Jerusalem, is a highly important task, as it is a way to assess the seismic hazard at these seismically active regions.

Constraining paleo *PGA* through backward analysis of seismically induced damage in historic masonry structures using numerical approaches belongs to a research that could be categorized as "archeo-seismology" and has been explored recently by others as well. Kamai and Hatzor (2008) utilized the 2D-DDA to investigate displacements of blocks in damaged archeological masonry arches at two sites in Israel, when subjected to sinusoidal accelerations. They found the *PGA* and frequency of motion that were likely to cause the observed damage. Yagoda-Biran and Hatzor (2010) used a similar approach to investigate the collapse of archeological monolithic columns in northern Israel, and constrained the *PGA* of the event that caused the collapse. Other research groups used seismically induced damage in archeological structures to investigate other earthquake parameters, such as source mechanism and back azimuth of motion (Caputo et al., 2011; Hinzen, 2009, 2012). A summary of quantitative methods in archeo-seismology is provided by Hinzen et al.(2011). While in the research projects mentioned earlier the boundary conditions of the problem were known to a good extent, in the case study discussed here there are many unknowns, and consequently a large number of simulations had to be performed in order to constrain paleo-PGA responsible for the mapped damage in the field. Supporting measured data from the field do not exist, such as monitoring block displacement, local stress measurements and site response analysis, except for the final displacements of the damaged block in the vault.

5.2 Archeological setting

The Temple Mount in the Old City of Jerusalem, the most sacred site for the Jewish religion and the third most holy site for Islam, has been inhabited for the last three millennia by different cultures and civilizations. As such, archeological research and excavations are continuously taking place around and inside the mountain to better understand the historic record. The Western Wall, also known as the Wailing Wall in the Jewish tradition, is part of the great wall that surrounded the second Jewish temple which was erected on Temple Mount, and in itself is considered a very sacred site for Judaism, second only to the Temple Mount itself. Excavations near the Western Wall began as early as the 19th century, by the British archeologists Charles Warren and Charles Wilson (Warren, 1876; Wilson et al., 1871), and following a long pause during most of the twentieth century, commenced after 1967 and continue to this day. The archeological excavation campaign near the Western Wall has revealed a series of underground openings and tunnels from different historical periods, an underground system referred today collectively as “the Western Wall Tunnels”, one of the most popular tourist destinations in Israel today. The buildings in the Western Wall Tunnels were not built underground originally, but rather were buried by buildings built during later periods above them. The older buildings, some of which are found filled with soil and gravel, are being revealed today by the ongoing excavations.

One of the most impressive findings in the Western Wall tunnels complex is a great bridge along with an aqueduct that connected between Mount Moria and Mount Zion across the Tyropoeon valley which is assumed to have serviced the traffic to the Temple Mount (Figure 5.1). The time period of the bridge construction will be addressed later in the discussion section. The bridge, hereafter referred to as the ‘Great Causeway’, is actually two bridges stretching one next to the other, each constructed of two rows of adjacent barrel vaults (Weksler-Bdolah et al., 2009). An example of a barrel vault bridge from the Ottoman period next to the town of Beer- Sheva can be seen in Figure 5.2.

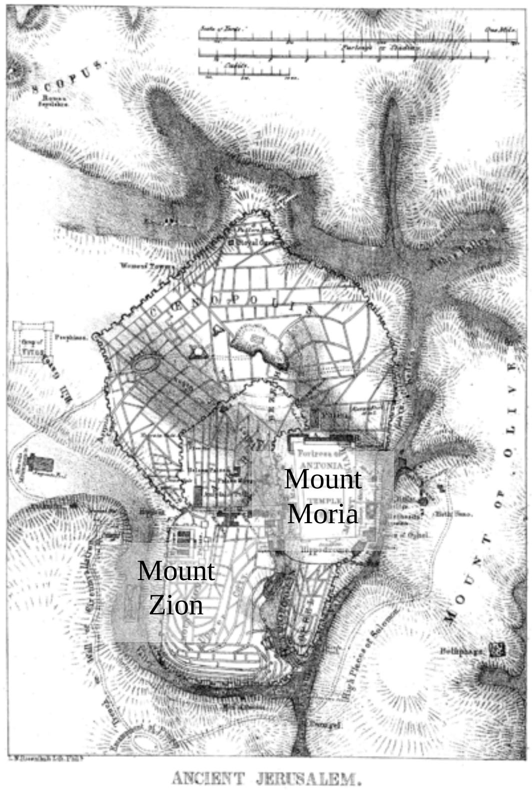

Figure 5.1. Map of ancient Jerusalem (after Barclay, 1858).

Figure 5.2. A barrel vault bridge built by the Turkish army during the First World War, Beer- Sheva Valley, Israel. Picture: Zahi Pan.

The length of the Great Causeway is 100 m, and its width is approximately 11 meters (Weksler-Bdolah et al., 2009) (Figure 5.3a). Not all the vaults have been excavated yet, but investigation of Vault 21 (see Figure 5.3b) reveals some unique block displacements in its roof.

a) 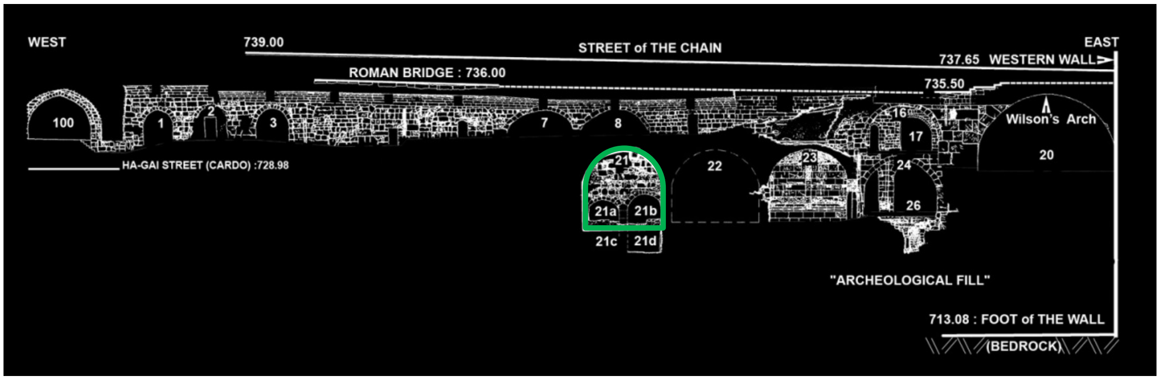

b) 

Figure 5.3. a) a section of the Great Causeway facing north (Onn et al., 2011). Vault 21 marked green. b) a picture taken in vault 21, looking at the ceiling. Note the marked downward displaced block. Picture by Yael Rosental.

A block adjacent to the center row of the vault, exhibits 7 cm of downward displacement, and appears locked in place. Keeping in mind that a vault, like an arch, is essentially a compressive structure, such arrested downward displacement can only result from instantaneous release of compressive stresses followed by re-compression, because the block moved downward and then was locked in place. It is very reasonable to assume that such stress release can occur during structural vibrations induced by dynamic seismic loading. Therefore mapping and modeling of the observed block displacement may be used to obtain some constraints on the paleo- seismic peak ground acceleration (*PGA*) that may have struck the structure, since it has been exposed to possible seismic hazards. This is particularly relevant because of the seismic history of Jerusalem derived from the nearby, seismically active, Dead Sea Transform. In this chapter we will try to constrain the *PGA* value that could have triggered the observed damage in Vault 21. Using available comprehensive earthquake catalogues for the past four millennia for the Levant region (Ben-Menahem, 1991) we will also try to place some time limits for the observed failure. The selected method of analysis will be the two dimensional DDA which has been verified extensively for dynamic applications by many researchers (for example Kamai and Hatzor, 2008; Yagoda-Biran and Hatzor, 2010).

5.3 The model of Vault 21

5.3.1 Initial assumptions

The barrel vault is naturally a three dimensional structure, and modeling it in two dimensions is of course an assumption that has to be justified. As mentioned earlier, the length of the bridge is 100 m, and its width is about 10 meters, so from a purely geometrical point of view, and because there are no forces acting on the vault parallel to its axis direction (see Figure 5.2), it is suggested here that the vault could be modeled as an arch in a state of plane stress. However, plane stress (as well as plane strain) is an assumption usually applied for continuous media. When dealing with discrete block systems, the assumption of plane stress would best be supported by measured stresses in the field, which, unfortunately, do not exist. For the sake of modeling we will assume the vault is in a state of plane stress.

There are many unknowns, when trying to determine the *PGA* that had caused the displacements as observed today in vault 21:

1. Was the observed damage necessarily induced by an earthquake?
2. If so - did the observed damage occur during a single event?
3. Since samples for friction angle determination tests could not be extracted, as the Giant Causeway is a very sensitive archeological excavation site, and as the mortar that must have existed between the blocks was totally washed at some places, what was the effective friction angle between the blocks at the time of the event?

4. What was the overburden at the time of the damage: was it while the bridge was serving as a road to the Temple Mount, or did it occur after the bridge had already been buried by newer buildings?

The only assumption made regarding these unknowns is that the observed displacement occurred during a single event, rather than an accumulation of many events. The rest of the unknowns mentioned above will be constrained through an extensive sensitivity analysis study, the results of which will be presented in the discussion section.

5.3.2 Geometry

Vault 21 was modeled in the 2D – DDA, therefore it is represented as a single arch. The arch is composed of nineteen blocks, numbered consecutively from 1 to 19 (see Figure 5.4). Blocks 1 and 19 were assigned with fixed points, therefore cannot move. Measurement points were assigned to all nineteen blocks, and displacements, rotations and strain readings for these points were printed as output by the code. Nineteen load points were assigned to the model, one at the center of each of the blocks' top face. These loading points were used to transfer overburden loads to the blocks, i.e. the filling above the vault, the pavement rocks of the bridge and excess overburden weight. The physical characteristics of the blocks constructing Vault 21 and numerical control parameters used in the simulations are listed in Table 5-1.

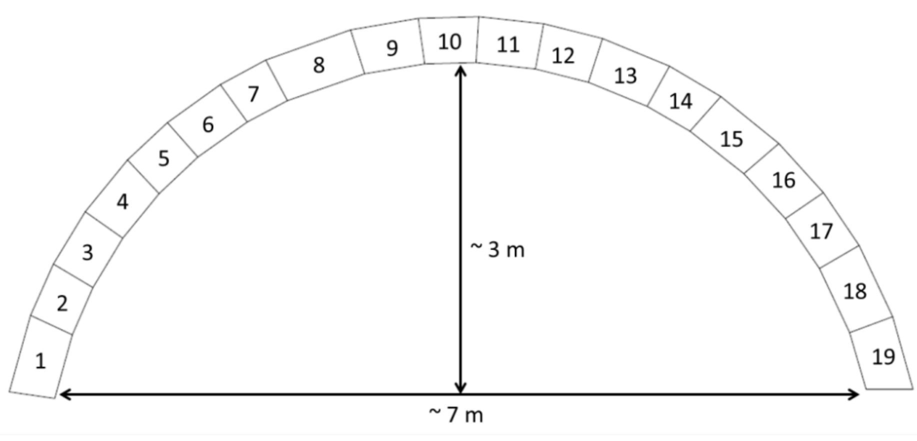

Figure 5.4. Vault 21, with block numbering.

Table 5-1. Physical and numerical parameters used in the simulations of vault 21

parameter	**value**
dynamic parameter *dd*	1 (fully dynamic)
normal contact spring stiffness	1×10^8 kN/m
time step size	0.001 sec
displacement ratio	0.001
density	2500 kg/m^3
Young's modulus	30 GPa
Poisson' ratio	0.25

5.3.3 Overburden

The vault was loaded by either one of two overburden schemes:

1. By the Great Causeway that led to Temple Mount. The load is calculated by an assumed fill density of 18 kN/m^3 and pavement density of 25 kN/m^3 (Eng. Yael Rosental, personal communication). This overburden scheme will be referred to as *light.*
2. By the Great Causeway and the Muslim Quarter built over it today. The estimated load of the Muslim Quarter is 300 kN/m^2 (Eng. Yael Rosental, personal communication), and it is added to the load of the fill and the pavement. This load scheme will be referred to as *heavy*.

5.3.4 Simulations types

The vault was subjected to four types of simulations, under different boundary conditions:

1) Static analyses: the vault was loaded by gravity only, under the two different overburden schemes, and under varying values of friction angle between the blocks, in order to find the minimal friction angle required for static stability.
2) Static analyses for the two loading schemes, under varying friction angles from the minimal friction angle required for static stability, up to 40^o, and removal of the overburden from a single block at a time, for blocks 5 to 15. The rationale behind the removal of overburden is that it was observed in the field, that some of the fill material was washed away from the top of the vault, thus removing the existing overburden from a specific keystone in the vault (Figure 5.5). As will be shown later, removal of the

overburden from different blocks might have significant effect on the stability of the vault, and therefore is considered in the simulations. Overburden was removed from blocks 5-15 only, because blocks 1 and 19 are fixed and therefore overburden removal from them will have no effect. As for blocks 2-4 and 16-18, they are very steeply oriented, and it is therefore assumed that even if fill above them was washed, they could not have remained free of overburden because adjacent fill material would inevitably cover them again.

3) Dynamic analyses for the two loading schemes, with varying friction angles, from the minimal friction angle required for static stability, up to 40°. During the dynamic analyses the vault was subjected to acceleration record of a real earthquake, where the *PGA* of the record was varied between 0.5 and 5 *g*.
4) Dynamic analyses for the two loading schemes, under varying friction angles from the minimal friction angle required for static stability, up to 40°, removal of the overburden from a single block at a time, for blocks 5 to 15, and *PGA* values varying between 0.5 *g* and 5 *g*.

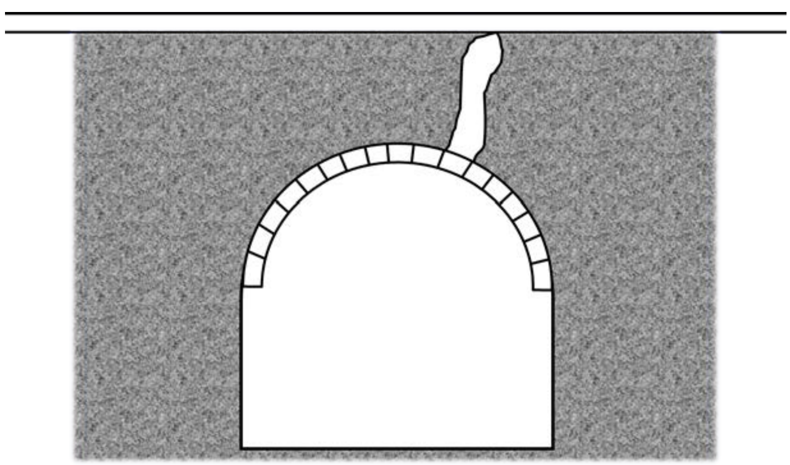

Figure 5.5. Schematic diagram of the vault. Fill material is missing in a certain area, this way removing the overburden load from a single block.

The acceleration record used in the dynamic analyses is the record of the Gulf of Aqaba earthquake, recorded on 25.11.1995, Mw=7.2. The original record was recorded in the city of Eilat, Israel, on fill, some 70 km from the epicenter. The record used here was de-convoluted for rock response, by Zaslavsky and Shapira (2000b). A time window of 10 sec was selected, and the east-west along with the vertical component were used (Figure 5.6). The *PGA* value of the horizontal component in the selected time window is 0.05 *g*, and the record was up-scaled by multiplying the entire time series by a scalar to obtain the desired level of *PGA*. Each simulation was given enough time to stabilize under gravity (between 1 and 10 seconds, depending on the friction angle used). For the dynamic analyses, the acceleration record was applied for 10 sec of real time after stabilization under gravity, followed by four more seconds after the earthquake had terminated.

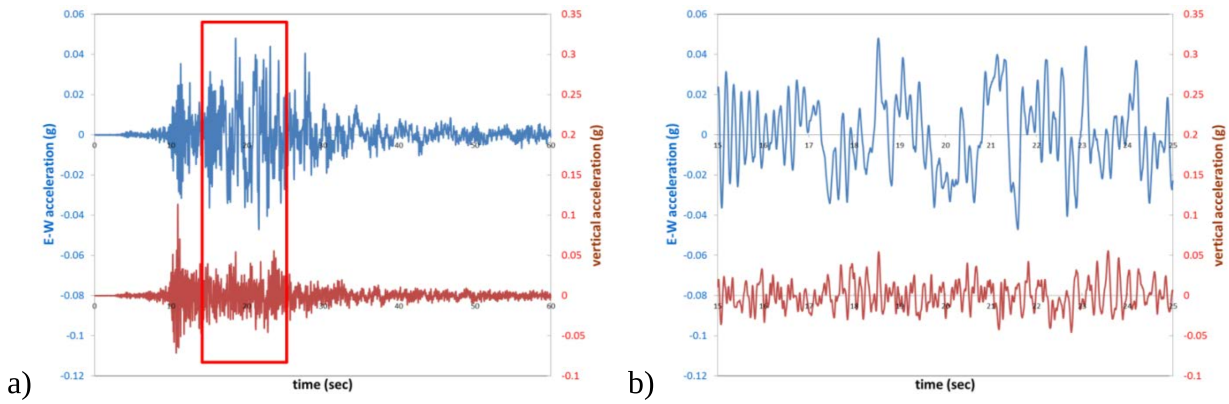

Figure 5.6. The acceleration record for the Nueiba 1995 Mw = 7.2 earthquake de-convoluted for rock response (after Zaslavsky and Shapira, 2000b). a) the entire E-W and vertical record. The red rectangle indicates the time window selected for dynamic analyses. b) the time window of 10 sec, between 15 and 25 sec, used in the dynamic simulations.

5.4 Results

Following the static simulations described in section 5.3.4, it was found that under the light overburden the vault was stable for friction angles of 9° and higher, and for the heavy overburden the vault was stable for friction angles of 12° and higher. Namely, under any reasonable friction angle value for the masonry block interfaces the vault is assumed to be stable under static conditions, as indeed would be expected.

5.4.1 General response of the vault to different variables

Two outputs of the simulations were of interest: first the vertical displacements of the different blocks, and second, and equally important, the graphical output of the analysis at the end of the simulation. The behavior of the vault was then categorized, according to the displacement records, into one of three performance categories:

1) Stable, insignificant displacements: the vault is stable, and the block that exhibited maximum displacement moved less than 1 cm at the end of the simulation. All simulations that fall into this category are colored green.
2) Stable, significant displacements: the vault is stable, and the block that exhibited maximum displacement moved more than 1 cm at the end of the simulation. All simulations that fall into this category are colored orange.
3) Unstable: the vault collapsed. All simulations that fall into this category are colored red.

A total of 1183 simulations were run, under the four different simulation types described in section 5.3.4. A table listing the simulations is available in Appendix B. A total of 805 simulations were performed with the light overburden, and 378 simulations with the heavy overburden. The large difference between the number of simulations for each overburden scheme is a result of the higher stability the vault exhibited under the heavy overburden – when the vault experienced hardly any displacements for low friction angles, higher friction angles were not simulated.

Figure 5.7 presents the distribution of the three behavior categories, in percentages. It can be seen from Figure 5.7a that in almost half of the simulations the vault collapsed, and the other half is almost evenly divided between significant and insignificant displacements. When investigating the results for the different overburden schemes separately, in Figure 5.7b and c, it can be seen that for the light overburden, in more than 50% of the simulations the vault collapsed, while for the heavy overburden, more than 50% were simulations with insignificant displacements, respectively.

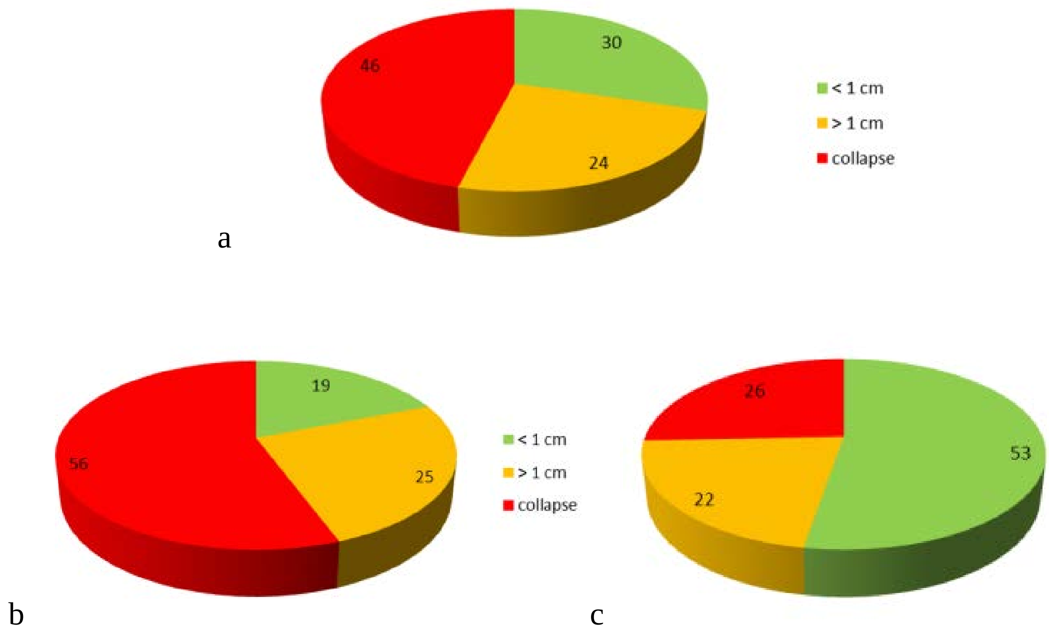

Figure 5.7. Result distributions in percentages of all (a), light overburden (b) and heavy overburden (c) simulations.

It is obvious that the data as presented in Figure 5.7 is biased, since many simulations, especially ones with the heavy overburden scheme, were not run as explained earlier. Therefore, a bias correction was applied, and all the simulations "missing" from the total of 1183 simulations actually run were added. All the simulations added for the correction are simulations that belong in the green category, that is, insignificant displacements. After the bias correction, there are 1913 simulations, where 975 are light overburden simulations, and 938 are heavy overburden simulations. In Figure 5.8 the distribution of the three different behavior categories after the bias correction is plotted. Now more than 50% of the total simulations result in insignificant displacements (green category, Figure 5.8a), and when analyzing the different overburden schemes, while the picture for the light overburden does not change dramatically (Figure 5.8b), the picture of the heavy overburden does, and now more than 80% of the simulations return insignificant displacements (Figure 5.8c).

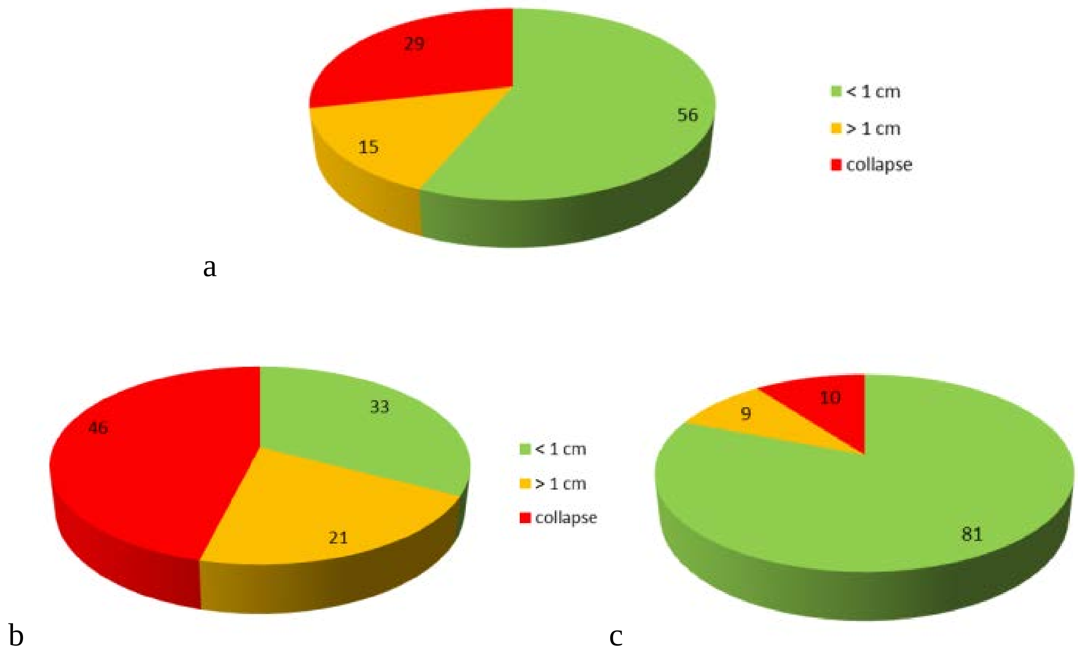

Figure 5.8. Result distributions in percentages after bias correction, of all (a), light overburden (b) and heavy overburden (c) simulations.

The next stage is to examine the response of the vault, again, by the three categories, as a function of the changing variables, or unknowns. The data analyzed here will be the unbiased data, and the response of the vault is investigated under the change in one variable at a time.

5.4.1.1 Response of the vault to changes in friction angle

Figure 5.9a and b present the response of the modeled vault as a function of changing values of friction angle, for the light overburden and heavy overburden, respectively. When looking at the heavy overburden results, in Figure 5.9b, it can be seen that for higher friction angles the stability region grows, and more simulations are stable with insignificant displacements. This is intuitive – the high friction keeps the vault more stable. However, when looking at Figure 5.9a, a different picture is obtained for the light overburden. Even when reaching the high friction angles, there is no significant change in the overall distribution of the different vault behaviors; even with high friction angles the vault still exhibits the same percentages of collapse, as in the lower friction angles.

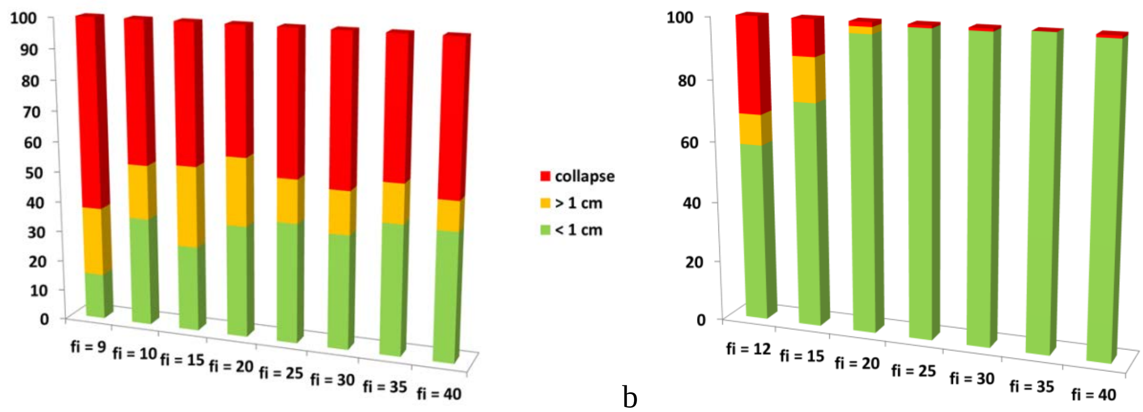

a b

Figure 5.9. the distribution of the vault response under different fricion angles, a) light overburden and b) heavy overburden.

Before attempting to explain this phenomenon, the study of the stability of masonry arches will be briefly reviewed. An analytical approach for describing the limit behavior of a masonry arch at the point of collapse was developed by Heyman (1982), and by Vilnay and Cheung (1986) and Vilnay (1988), who modeled the masonry arch as a three-beam model. Heyman (1982) made three key assumptions: 1) sliding failure cannot occur in an arch, either because of high friction or block locking 2) masonry has no tensile strength and 3) masonry has infinite compressive strength. The most significant assumption considering the strength of the arch is the second one, which indicates that failure of the arch is conditioned by the existence of tensile forces at the joints. Since there is no tensile strength across the joints, such forces cause opening of some of the joints by hinge formation either at the top or the bottom of the joint, and by rotation of the blocks about their edges. The location of hinges and amount of rotation determine the mode of failure the arch experiences, if rotation is not arrested. The existence of tensile forces at the joints can be studied by investigating the position of the thrust line (Heyman, 1982; Vilnay and Cheung, 1986). The thrust line connects all equivalent stress vectors, representing the compressive stresses transmitted between the blocks, at equilibrium with external loads. If the thrust line is entirely contained within an arch, the arch is stable. On the other hand, if the line of thrust touches the edge of the arch ring, a hinge will form. In order for the arch to form a failure mechanism, four or more hinges must be formed, as four hinges will divide the arch to three beams. Heyman (1982), Vilnay and Cheung (1986) and Vilnay (1988) also studied the stability of an arch loaded by an external point load. Applying external point load causes shifts in the location of the line of thrust and of the hinges, and can cause failure if the load is high enough. Figure 5.10 shows the schematics of a semi-circular arch loaded by an external point load P. Note the dashed trace of the line of thrust.

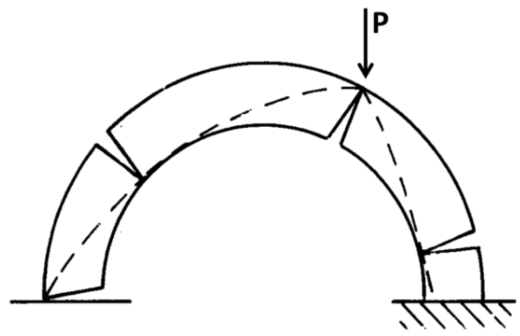

Figure 5.10. Failure mechanism of a semi-circular arch under external point load P. After Heyman (1997).

Going back to our light overburden simulations, the phenomenon discussed earlier can be explained by the failure mechanism illustrated in Figure 5.11, in which snapshots from a single simulation are presented, under *PGA* = 4 *g* and $\phi = 40^{o}$. It seems that at high friction angles the vault exhibits the behavior similar to the one described analytically by Heyman (1982). The deformation of the block system is locked after some initial damage, forming a more or less rigid structure composed of three beams with distinct hinges. Under high *PGA* values, the vault experiences significant displacements, and the beams disconnect from each other, leading to total collapse. In the case of light load, a high friction angle does not allow the displacements between the blocks, which can stabilize the vault even under large displacements, give it some flexibility, and prevent it from collapsing. Heyman (1982) subjected the arch to a static point load, but we show here that dynamic loads result in the same failure mechanism.

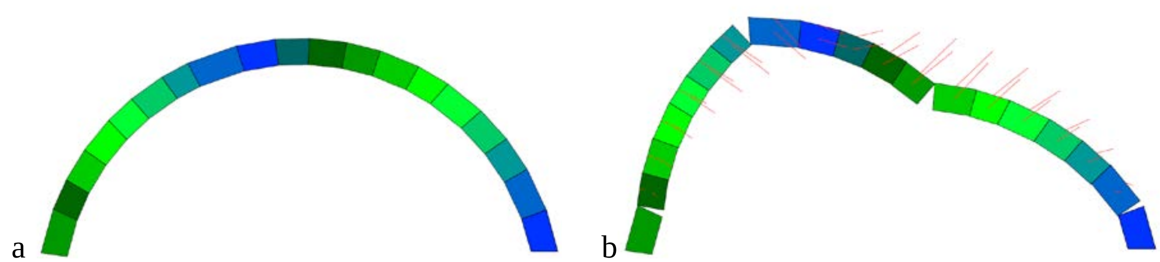

Figure 5.11. Snapshots from a DDA simulation under the light overburden. *PGA* = 4 *g* and $\phi = 40$, a) at the beginning of the simulation and b) after 7 sec of the simulation. Note the vault is actually divided into three rigid beams.

5.4.1.2 Response of the vault to changes in PGA values

In Figure 5.12 the response of the vault as a function of changing values of *PGA* is plotted. As would be intuitively expected, the higher the *PGA* value the more confined the area of stability is. This trend is similar for both light and heavy overburdens, but is much more significant in the case of the light overburden.

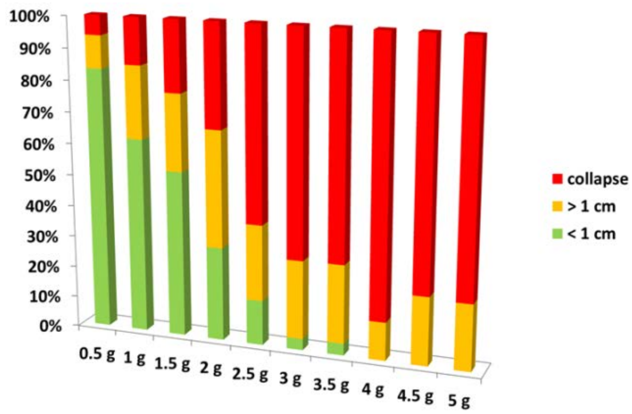

a

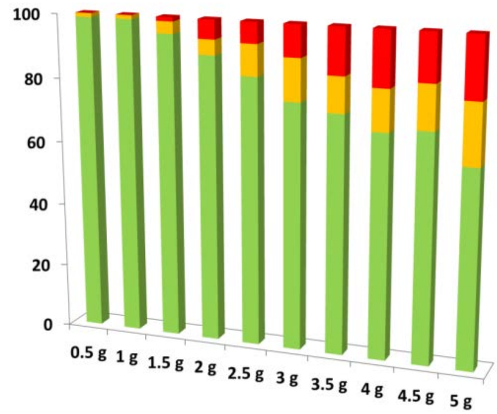

b

Figure 5.12.The distribution of the vault response under different PGA values for a) light overburden and b) heavy overburden.

5.4.1.3 Response of the vault to overburden removal from individual blocks

Overburden was removed from individual blocks since in the field it was observed that some of the fill material was washed away from the top of the vault, thus removing the existing overburden from a specific keystone in the vault. It is suggested that this overburden removal might have a significant effect on relative displacements of the different blocks, and therefore this approach was adopted for many of the simulations.

Figure 5.13 a and b present the response of the vault as a function of changing block number with overburden removal. From Figure 5.13a one can see that the vault is more sensitive to removal of overburden from its flanks, rather than from its center. A similar but less significant trend is visible in the heavy overburden (Figure 5.13b).

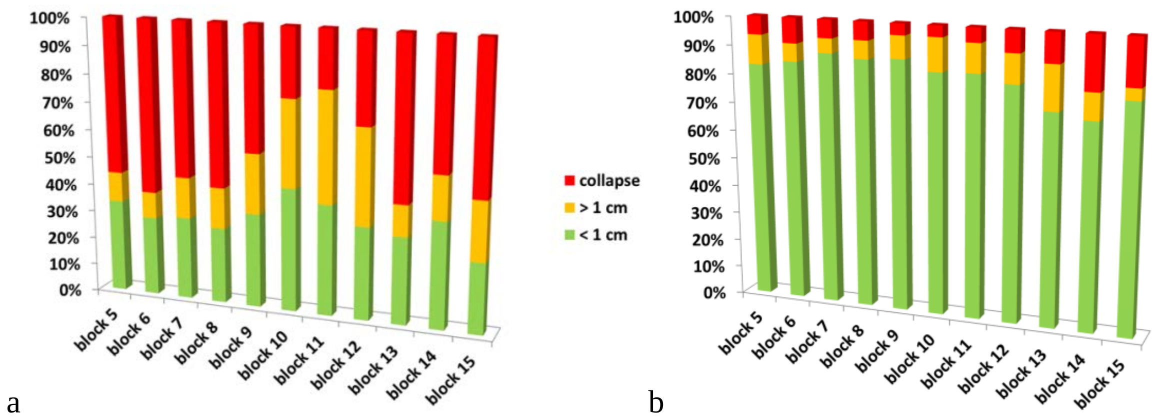

Figure 5.13. The distribution of the vault response when removing the overburden from different blocks, a single block at a time for: a) light overburden and b) heavy overburden.

5.4.2 Response of block 11

The main objective of the project is finding the *PGA* of the event that had caused the damage in Vault 21. In order to do that, the graphical output of each and every simulation of the 1183 simulations run was studied visually. Only simulations that belong to category 2, the orange category – stable vault with significant displacements, can be considered relevant for this purpose. As mentioned earlier, block 11 is the block that moved downwards relative to the rest of the roof. The net displacement of block 11 in the simulations is less important than its displacement relative to the adjacent blocks. In reality, block 11 is displaced about 7 cm relative to its neighbors.

Out of 1183 simulations run, 284 simulations were categorized orange. Of these, 48 returned damage that was initially considered relevant. Of the 48, 18 simulations made it to the final line, and they are listed in Table 5-2, along with their parameters. For the sake of discussion, the simulations listed in Table 5-2 will be referred to as “relevant”.

Table 5-2.The simulations that returned damage that resembles the damage observed at Vault 21

#	Loading scheme	PGA (*g*)	Overburden removed from block #	Friction angle	Relative displacement of block 11
1	Light	-	6	9	1
2	Light	2.5	-	25	1.5 (block 12)
3	Light	2.5	-	30	2 (block 12)
4	Light	2	14	18	2
5	Light	2	9	15	1.5
6	Light	2	8	15	2
7	Light	2	8	14	1.5
8	Light	2	6	14	3
9	Light	2	5	14	1.5
10	Light	1.5	15	17	1
11	Light	1.5	8	14	1.5
12	Light	1.5	8	13	2
13	Light	1.5	8	12	3
14	Light	1	8	10	2.5
15	heavy	5	5	17	1.5
16	heavy	4.5	9	14	1
17	heavy	4.5	5	16	1.2
18	heavy	4	6	15	1.5

Figure 5.14 presents the final snapshots of all relevant simulations listed in Table 5-2. For each simulation the overall view of the vault is presented, as well as an inset of block 11 and its neighbors. The relative displacement of block 11 is labeled in black.

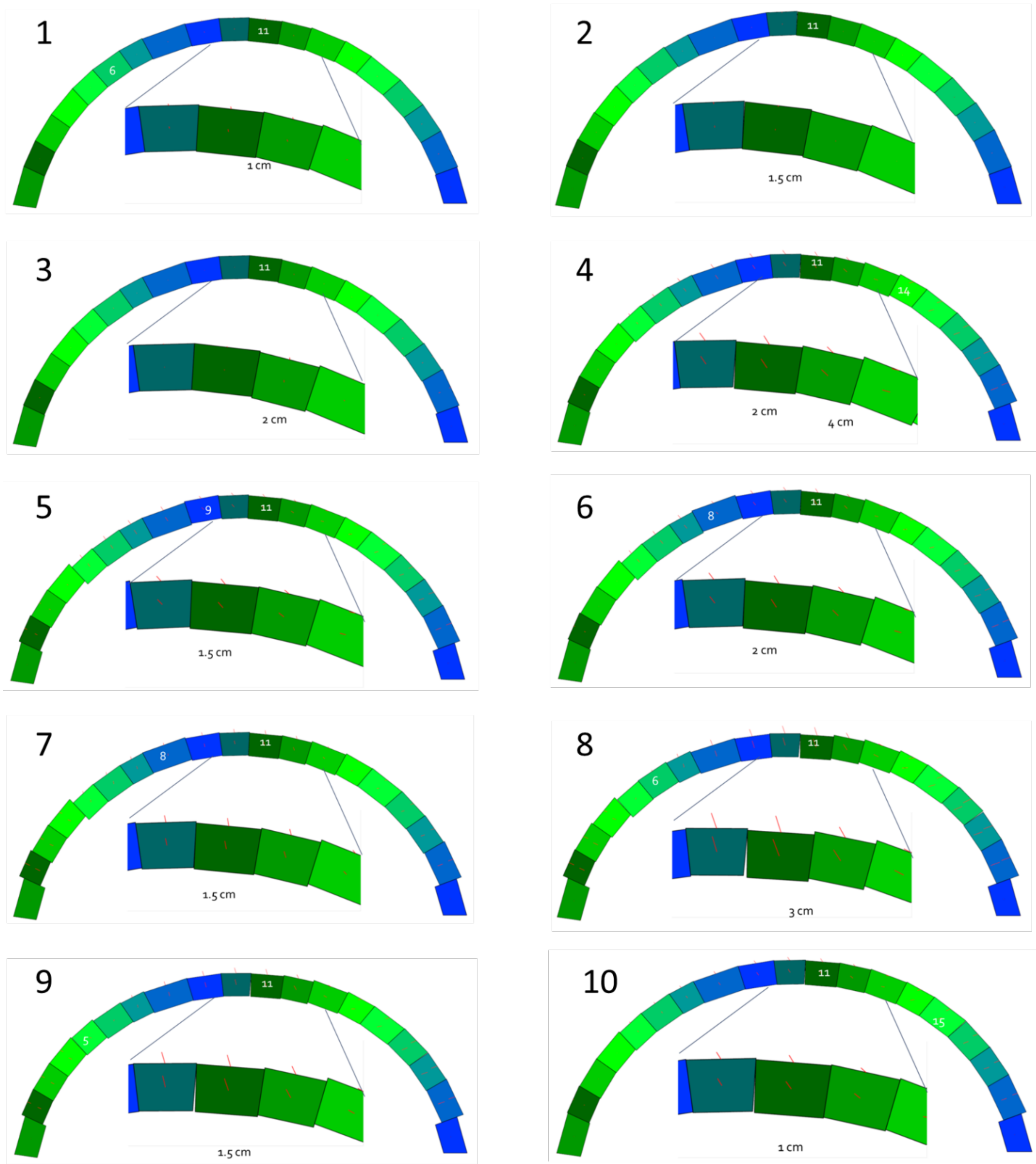

Figure 5.14. Graphic output of the 18 relevant simulations listed in Table 5-2, which best mimicked the damage to block 11 in vault 21. In each simulation, the vicinity of block 11 was enlarged, and the relative displacement of block 11 is stated in the figure.

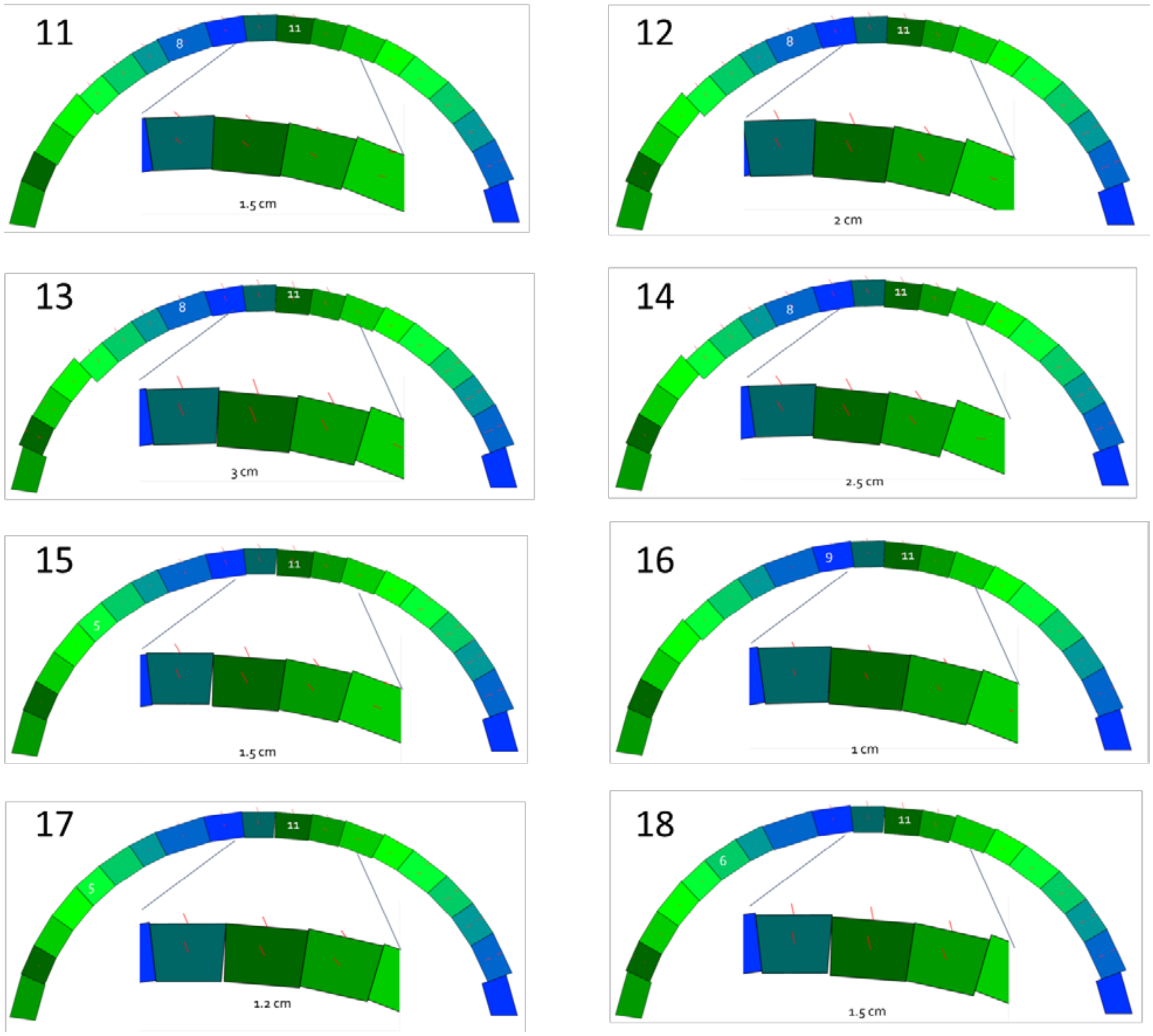

Figure 5.14. Contnd.

Examination of Table 5-2 leads to some interesting insights:

1. Only 4 out of 18 relevant simulations were with heavy overburden (simulations 15-18). That is, 78% of relevant simulations were under light overburden.
2. Only one relevant simulation was under static conditions (simulation 1).
3. Only two relevant simulations were executed with overburden on all blocks (simulations 2-3). In these simulations, it was block 12 that was actually relatively displaced.

4. In all dynamic simulations with overburden removal, the friction angle was between 10-18^{o} (simulations 4-18). This value will be discussed in the discussion section.

Inspection of the terminal snapshots of simulations 8, 13 and 14 in Figure 5.14 reveals that they return the highest values of relative displacements of block 11: 3, 3 and 2.5 cm, respectively. Although the displacement obtained in DDA is lower than the one observed at Vault 21, these simulations are closest to mimicking the damage observed. Inspection of the relevant parameters of simulations 8, 13 and 14, reveals the *PGA* value of these simulations is between 1.5-2 *g*, with overburden removed from a single block. In these simulations the overburden removal is from blocks 6 and 8, from the left flank of the vault, and the friction angle is 10-14^{o}.

5.5 Discussion

From section 5.4.2 we learn that the *PGA* required to cause the damage observed in Vault 21 is between 1.5 and 2 *g*. These values are no doubt very high, much higher than the value of 0.132 *g* expected in Jerusalem according to the Israeli Building Code 413 (S.I.I., 2004). In order to constrain the time of the event that caused the damage to Vault 21, we must search for historical earthquakes that left their marks on Jerusalem.

5.5.1 Historical earthquakes

In an investigation of the last 4000 years earthquake catalogue along the Dead Sea Rift (Ben-Menahem, 1991), many earthquakes that were either felt in Jerusalem, or damaged it, are reported. In order to constrain the time period for the potential earthquake that caused the studied damage in Vault 21, the time span of the Great Causeway while it was serving its purpose, first needs to be determined. There is an agreement between archaeologists concerning the period in which the Great Causeway was buried, and that is the Mamluk period (starting 1260 AD). However, there is a debate concerning the time the Great Causeway was constructed. Bahat (1993, 2007) claims that an older bridge was built during the Hashmonai period (160 – 63 BC), but was destroyed along with the second Temple, and the bridge that was exposed in excavations today was actually built during the Muslim period (638-1100 AD). Weksler-Bdolah et al. (2009) claim that the present bridge was built during the Roman period between the 2nd – 3rd centuries AD. Following Weksler-Bdolah et al. (2009), which consider a longer time span for the Great

Causeway being exposed above the ground surface, we looked for earthquakes that occurred between 70 AD (the time of the destruction of the second Temple, an event that the bridge most definitely would not have survived), and 1260 AD (the beginning of the Mamluk period). Table 5-3 lists the earthquakes from that period of time, which Ben-Menahem (1991) in his catalogue clearly states that these quakes were felt in Jerusalem, or had damaged Jerusalem.

Table 5-3. A list of earthquakes from 70 to 1260 AD that had damaged (shaded) or were felt in Jerusalem. From Ben–Menahem (1991)

Date (AD)	**Location**	**M_L**	**damage description**
306	Off coast Sur	7.1	Destruction at Sur and Sidon, felt in Jerusalem. Tsunami at Ceasaria.
362	31.3N 35.6E	6.7	East of the Lisan. damage to the temple area in Jerusalem.
447	40.2N 28E	7.5	Felt in Jerusalem and Egypt.
528	36.2N 36.1E	7.1	Destruction of Antioch, damage in Jerusalem and Damascus. Felt in Egypt, Turkey, Armenia and Mesopotamia
746	32N 35.5E	7.3	Destruction in buildings in all major cities from Tiberius to Arad.
859	36.2N 36.1E	8	Total destruction of Antioch. Damage in Jerusalem (D=500 km). Felt in Egypt, Turkey, Armenia, Mesopotamia and Mecca.
1032	Off coast Gaza	6.9	Tsunami, heavy damage in Gaza, Felt in Jerusalem and Negev.
1068	Off coast Yavne	7	Tsunami at southern Israeli coasts. Sea receded and returned, felt in Jerusalem, Ramla, Egypt and Arabia.
1070	Arava	6	Felt in Jerusalem.
1114	37.1N 36E	7	Tsunami. Felt in Jerusalem, destruction of Antioch. Epicenter probably on SW tip of EAFS.
1115	37N 38.9E	7.5	Walls of Edessa destroyed. Strong in Syria and Jerusalem.
1170	35.9N 36.4E	7.5	Many thousands of victims. Destruction in Lebanon and Syria. Damage and casualties in the Orontes valley and Israel. Damage to the walls of Sur and Jerusalem.

Placing these earthquakes, with their epicenters located by Ben-Menahem (1991) on a map (Figure 5.15), the distance to Jerusalem can be measured.

Figure 5.15. A location map of the historical earthquakes, according to Ben-Menahem (1991). The red and yellow symbols indicate the locations of epicenters of earthquakes that had damaged or were felt in Jerusalem (indicated by a star), respectively.

With the earthquake magnitude, the *PGA* at a certain distance *R* from the epicenter can be estimated using published attenuation relationships. Here *PGA* was calculated using two attenuation relations: Boore et al. (1997) adapted to the Dead Sea transform (Eq. 5.1),

$$\ln PGA = -0.055 + 0.525(M - 6) - 0.778 \ln \sqrt{R^2 + 31.02}$$ Equation 5-1

and Ben-Menahem (1991), in Eq. 5.2

$$PGA = 17.8 e^{1.21 M_L} \left(R + 25\right)^{-1.32} e^{-R/400}$$ Equation 5-2

Table 5-4 lists the earthquakes with their epicenter distance from Jerusalem, and the *PGA* calculated for Jerusalem by the two methods mentioned above.

Table 5-4. Epicenter distance of relevant earthquakes from Jerusalem, along with the *PGA* calculated for Jerusalem using the Ben-Menahem (1991) and Boore et al. (1997) attenuation relationships

Date	**Location**	**M_L**	**Distance to Jerusalem (km)**	***PGA* (*g*) Ben- Menahem (1991)**	***PGA* (*g*) Boore et al. (1997)**
306	Off coast Sur	7.1	170	0.06	0.03
362	31.3N 35.6E	6.7	63	0.14	0.05
447	40.2N 28E	7.5	1100	0.0009	0.009
528	36.2N 36.1E	7.1	500	0.007	0.013
746	32N 35.5E	7.3	38	0.48	0.11
859	36.2N 36.1E	8	500	0.02	0.02
1032	Off coast Gaza	6.9	130	0.07	0.034
1068	Off coast Yavne	7	80	0.15	0.053
1070	Arava	6	170	0.016	0.017
1114	37.1N 36E	7	600	0.004	0.01
1115	37N 38.9E	7.5	670	0.005	0.013
1170	35.9N 36.4E	7.5	470	0.014	0.017

Clearly from Table 5-4 it can be seen that the *PGA* calculated by the Ben-Menahem (1991) relation is higher than the one calculated by Boore et al. (1997) for short distances from epicenter, while the Boore et al. (1997) relation gives a higher estimation for the longer distances. It is important to state here that while the Boore et al. (1997) relationship is based on analysis of strong motion data recordings, the Ben-Menahem (1991) relationship is based on the Modified Mercalli scale, therefore the *PGA* calculated this way might include some site effects, as the Modified Mercalli intensity scale is based on the *effects* of the earthquake on the surface.

Adopting the *PGA* calculated using the Ben-Menahem (1991) attenuation relationship, there are three potential earthquakes that give high values of *PGA* in Table 5-4: the earthquakes of 362, 746 and 1068 AD. The earthquake of 1068 was neglected, since in his paper Ben-Menahem (1991) states that it was *felt* in Jerusalem, rather than *damaged* Jerusalem. Thus two earthquakes remain relevant: the 362 earthquake at eastern Dead Sea, and the 746 earthquake in the Jordan Valley, with *PGA* values of 0.15 and 0.48 *g*, respectively. However, note that even the high *PGA* value of 0.48 *g* of the 746 earthquake is not sufficient to explain the observed damage in vault 21, which requires *PGA* values of 1.5-2 *g*. In order to reach these high values, site specific amplifications must be considered.

5.5.2 Seismic amplification

Seismic amplification is a phenomenon where ground motions at a site may be increased by focusing of seismic energy, caused by the geometry of the velocity structure, for example basin subsurface topography. Consider for example the basin in Figure 5.16. Inside the basin there is lower velocity sediment, which is surrounded by higher velocity bedrock. When the seismic waves propagate from the bedrock into the basin, because of the velocity differences they are “trapped” inside the basin, and constructive interference amplify the ground motions they cause.

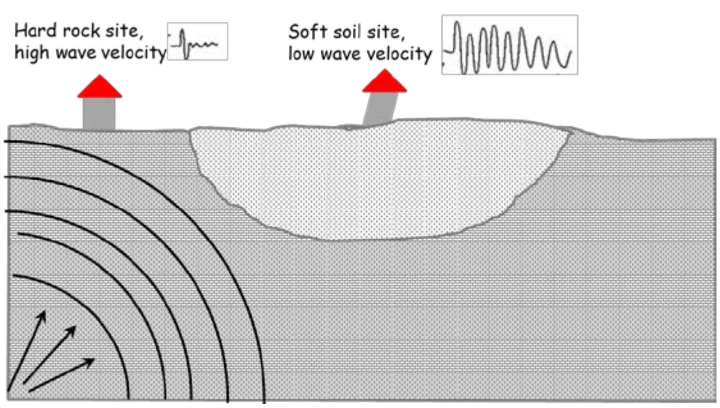

Figure 5.16. Schematics of the site amplification phenomenon.

In our case study of Jerusalem, the geological map in Figure 5.17 shows the Great Causeway is built over two formations from the Turonian: the Netzer and the Shivta formations, both of limestone lithology. Since the lithology does not support existence of amplification, a different mechanism must be found.

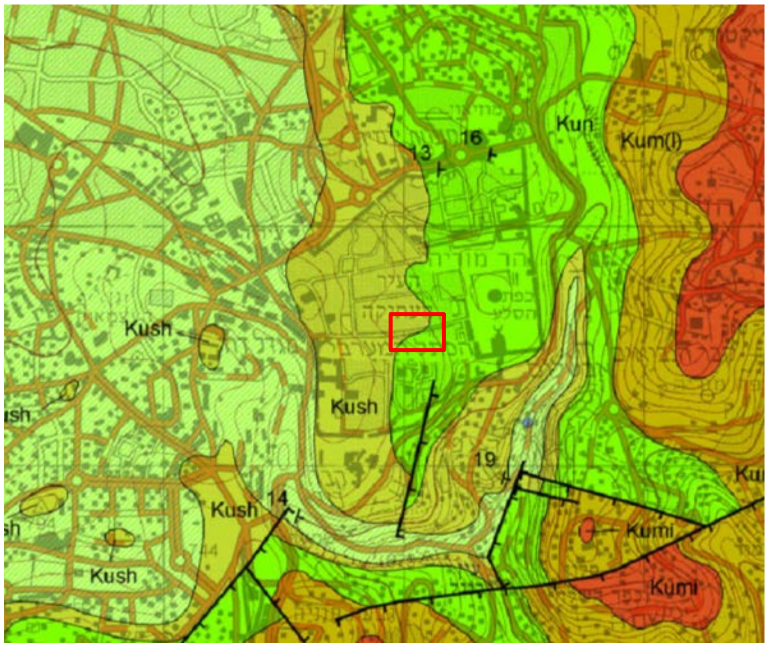

Figure 5.17. Geologic map scaled 1:50,000 of the Old City of Jerusalem. The Great Causeway, location marked by a red rectangle, is either on the Kush = upper Cretaceous Shivta formation, or the Kun = upper Cretaceous Netzer formation (Sneh and Avni, 2011).

In the case of the Great Causeway over the Valley of Tyropoeon, the valley's beds are composed of the bedrock: a hard limestone. The valley itself however is filled with archeological material, from buildings of older periods. Drillings beneath the Great Causeway have reached a depth of 6 m without reaching the bedrock. At the nearby Western Wall the bedrock is 12 m deep (Eng. Yael Rosental, personal communications). It is thus concluded that beneath the Giant Causeway there is a layer of soft fill material, with depth yet to be determined, probably between 6 and 12m, as schematically illustrated in Figure 5.18, with wave velocity much lower than the surrounding bedrock, a geometry that is very favorable for seismic amplifications.

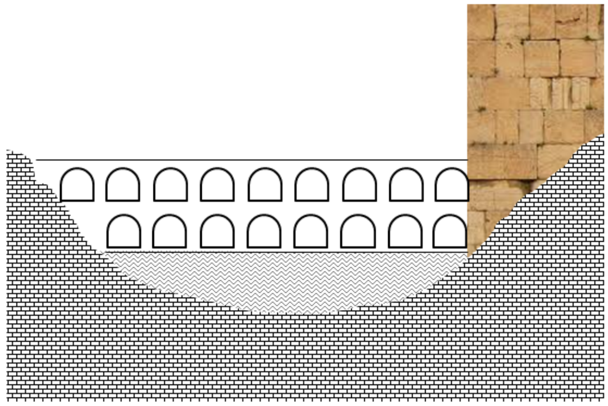

Figure 5.18. A schematic illustration of the basic topography beneath the Giant Causeway. The brick-patterned area is the bedrock, forming the Tyropoeon Valley, the wave-patterned area is the archaeological fill beneath the bridge and the Western Wall is on the right bank of the valley.

As a rule of thumb, one-dimensional amplification factor for a homogeneous un-damped soil on rigid rock at resonance frequency can be approximated by equation 5.3 (Towhata, 2008):

$$A_0 = \frac{\rho_B \cdot v_B}{\rho_S \cdot v_S} \qquad \text{Equation 5-3}$$

If damping is considered then the amplification at resonance may be estimated using equation 5.4:

$$A_0 = \frac{1}{\frac{\rho_S \cdot v_S}{\rho_B \cdot v_B} + \frac{\pi}{2}\zeta} \qquad \text{Equation 5-4}$$

where A_0 is the amplification factor, ρ_S, v_S, ρ_B and v_B are the density and s-wave velocity for the soft layer and the bedrock, respectively, and ζ is the damping ratio.

Taking reasonable values for density and shear wave velocities for the two layers, as listed in Table 5-5, results in amplification factors that reach very high values, as presented in Figure 5.19. The velocities adopted for the fill are also consistent with the definition of soil class *D* and *E*, as classified by NEHRP (2004).

Table 5-5. Values of density and shear wave velocity for amplification calculations

layer	parameters	
	density (kg/m³)	**shear wave velocity (m/sec)**
Bedrock	2500	2000 - 3000
archeological fill (adopted alluvium values)	1800	100 - 500

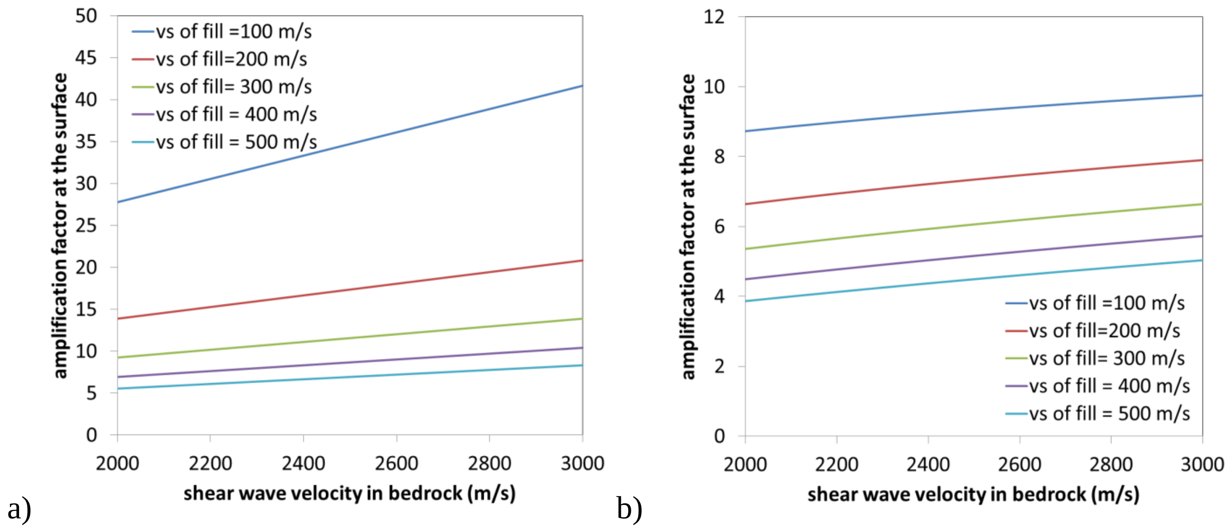

Figure 5.19. Amplification factor calculations for a combination of ρ_S = 1800 kg/m^3 and ρ_B = 2500 kg/m^3. a) no damping introduced, according to Eq. 5.3. b) damping of 5% introduced, according to Eq. 5.4.

Inspection of Figure 5.19a reveals that when no damping is introduced, an amplification factor of 10, just enough to amplify 0.15 *g* to the required 1.5 *g* can be easily reached with a combination of v_B of 2200 m/sec and v_S of 300 m/sec, as well as with a combination of v_B = 2500 m/sec and v_S = 350 m/sec. An amplification factor of 14, enough to amplify 0.15 *g* to 2 *g* can be reached with a combination of v_B = 2500 m/sec and v_s = 250 m/sec.

Naturally, this amplification study is a simple one, and uses a rule of thumb. It must be said though that every site response analysis that is performed, will have its unknowns, and inherent assumptions. For example, a one-dimensional site response analysis performed with SHAKE (Lysmer et al., 1972; Schnabel et al., 1972) will need as input the velocities which are unknown, the shear modulus degradation relationship (G/G_{max}) which is unknown, the damping ratio and its evolution with shear strain, etc. For a two-dimensional site effect analysis, that takes into account the geometry of the valley of the Tyropoeon, the exact mapping of the bedrock under the bridge is required, and at this time is undetermined, along with the unknowns mentioned earlier. Therefore, in light of the few parameters that are known, site amplification estimations using Equations 5.3 and 5.4 provide a starting point, for a future, more robust attempt to quantify the site response and to better refine the paleo *PGA* estimation based on our numerical results.

These values of amplification factors mentioned earlier, along with the conclusion that a high *PGA* value is required for causing the observed damage at Vault 21, imply that the area of the Great Causeway, and probably its surroundings as well, might be subjected to high amplification factors in case of a strong earthquake, and therefore these finding must be taken into account when planning new buildings in that area of the Old City of Jerusalem, and when planning preservations of existing ancient ones. Furthermore, in light of the high amplification value found here, the seismic risk map provided by the Israeli Building Code 413 (S.I.I., 2004) is found wanting, as we show here the local amplifications play a very significant role in structural deformation during shaking in the old city of Jerusalem.

Another interesting point worth mentioning, is the fact that in the simulations that best mimicked the damage cited, the friction angle between the blocks is between 10^{o} and 14^{o}, a value that well represents friction angles for classic plaster/mortar used in interfaces between masonry stones (Ali et al., 2012).

5.6 Summary and Conclusions

A historical damage to an old bridge in the Old City of Jerusalem was analyzed. The bridge, once used for easy access to the Temple Mount and bearing the aqueduct to it, is built of a series of barrel vaults, and today is buried underground. One of the vaults, namely Vault 21, exhibits relative displacement of one of the blocks, which is downward displaced by 7 cm, relative to neighbor blocks. Such a displacement in a compressive structure might imply application of dynamic forces on the vault, such as an earthquake, and a paleo-seismic study was performed. Modeling the vault as a two-dimensional arch, and subjecting it to dynamic as well as static loads, under different loading schemes and different friction angles returned some interesting results, which lead to the following conclusions:

1. Vault 21 was damaged by an earthquake.

2. The damage most likely was caused while the bridge was serving its purpose, and not buried underground.
3. At the time of the earthquake, the fill above some areas of the vault was already washed, thus removing the load off certain blocks, and allowing for differential displacements of the blocks.
4. The PGA causing the damage is between 1.5 and 2 *g*.
5. Two candidate earthquakes might have caused the observed damage: the 362 AD EQ, east of the Lisan Peninsula and 746 AD EQ, in the Jordan Valley.
6. The amplification factor for the bridge is significant, and can reach very high values. Large amplification factors must be taken into account when planning new buildings in the old city of Jerusalem, and when designing preservations for old ones.

6. Discussion and conclusions

The research described in this dissertation focuses on different aspects of seismic hazard analysis using the numerical Discontinuous Deformation Analysis (DDA) method, and examines the response of both natural and man-made structures to ground motions induced by earthquakes, as ground motions are considered one of the most significant damage-causing seismic hazards. The ground motions a certain site would experience during an earthquake are a function of three variables: the source of the seismic waves, the path through which the waves travel and the conditions of the site they reach. The research presented here focuses on the last link in this chain: the site. When considering earthquake parameters that affect the response of structures, the predominant frequency of the seismic waves and the peak ground acceleration of the record are key parameters that have great influence on structural response. The research presented here draws practical conclusions concerning the response of structures, either natural or man-made, to earthquake forces and earthquake induced ground motions.

6.1 Site response analysis with 2D-DDA

A key parameter in site response analysis is the resonance frequency of the site or structure. The first project of the dissertation tests the ability of the 2D-DDA to perform site response analysis. Modeling such a dynamic mechanism has never been attempted in rock engineering context with DDA, or with any other numerical discrete element method that would have been typically applied otherwise to rock engineering problems involving the dynamic interactions of multiple blocks. A multi drum column from the World Heritage Site of Avdat is modeled with 2D-DDA, and its dynamic response is compared with experimental data obtained in a geophysical site response survey conducted at the site. The DDA returns a resonance frequency range that was very close to the value obtained experimentally. The optimal normal contact spring stiffness value, *k*, as obtained by comparison between DDA and the geophysical experiment, falls well within the acceptable range of penalty values obtained from a preliminary calibration made for *k*, independently of the experimental results. Furthermore, it is shown here that the obtained natural frequency is not affected by the choice of time step size. Still, it is recommended that the time step size should be carefully selected, in order to optimize the balance between computing efficiency and accuracy. It should be pointed out that the DDA results show great sensitivity to the user defined numerical control parameter of normal contact spring stiffness, k. The value of k has great effect on both the natural frequency of the column as well as the amplitude: increase in the value of k leads to an increase in the natural frequency and a decrease in the amplitude, as would be expected intuitively, as the column behaves more rigidly. This problem can be evaded by preliminary calibration of the k value, such as that performed here.

To summarize, it is proven here that with preliminary calibration and optimization of the user defined numerical control parameters, 2D-DDA can be used for numerical site response analysis that in turn can help better understand the expected response of a site or structure during a strong earthquake, and therefore mitigate motion induced damages.

6.2 A new failure mode chart for toppling and sliding with consideration of earthquake inertia force

Mapping and predicting the mode of failure of a rock slope subjected to seismic excitations, modeled as a block on an incline under pseudo-static force, can help design proper support, as it is sometimes crucial to take into account seismic forces that can affect the stability of the rock mass. In this dissertation previous research regarding the problem of a block on an incline is reviewed, and, for the first time, the four possible modes of the block are mapped in a three dimensional space, as the modes are a function of three angles: the block angle δ (block width / block height), the friction angle of the interface between the slope and the block ϕ, and the inclination of the slope α. Then, a new failure mode chart is derived, incorporating the frequently used pseudo-static approach in geotechnical earthquake engineering. In the new chart, the mode of failure of the block is a function of δ, ϕ, and a new angle, $\psi = \alpha + \beta$, β being the angle between the resultant of the block weight and the pseudo-static force applied on the block, and the vertical direction. Verification of the 3D-DDA with the formerly derived analytical solution for a block on an inclined plane under gravitational loading alone proves the 3D-DDA can accurately solve the problem. Furthermore, the 2D and 3D-DDA simulations of the block subjected to pseudo-static horizontal force confirm the new analytical boundaries derived here.

The new failure mode chart derived here, with the incorporation of a pseudo-static horizontal force simulating the seismic force of an earthquake, is an easy, more intuitive way to understand and predict the behavior of rock masses subjected to seismic forces, when these are modeled as a pseudo-static horizontal force. When using the new chart, the pseudo-static force for the mode analysis should be carefully selected, taking into account seismic hazard assessments in the region discussed, and preferably site effects, where these are known.

6.3 Paleo-seismological implications of historic block displacements in the Western Wall Tunnels, the Old City of Jerusalem

Constraining peak ground acceleration (*PGA*) values experienced at a site during past strong earthquakes can help predict the expected acceleration values in that site during future events. Furthermore, it can help assess expected amplification factors, another well-known site effect, which has a significant influence on the intensity of the ground motions felt at a site. Applying sophisticated and robust quantitative tools which originate from numerical analysis in rock mechanics to the young and very important *archeo-seismology* field of science can help constrain, quantitatively, historic earthquake parameters such as the *PGA* experienced during these earthquakes, and better constrain the seismic risk associated with a particular region. In Chapter 5 of the dissertation a historical damage to an ancient bridge in the old city of Jerusalem is analyzed. The bridge, built during the 3rd century AD, was used for easy access to the Temple Mount and bearing its aqueduct, was built of a series of barrel vaults, and today is buried underground. In one of the vaults, locally referred to as vault 21, one block was displaced downwards by 7 cm relative to its neighboring blocks. Due to detected limitations of the current 3D-DDA code for reliably modeling dynamic interactions of multiple block system, the vault was modeled as a two dimensional arch in the 2D-DDA under plane stress boundary conditions, and was subjected to dynamic as well as static loads, under different loading schemes and different friction angles. Results of hundreds of simulations led to the conclusion that vault 21 was indeed damaged by an earthquake, during times when the bridge was serving its purpose on the ground surface rather than when it was buried underground, as it is today. We obtain that the observed differential displacement of the studied block in vault 21 could only have been made possible if erosional washing of fill material in specific locations above the vault was allowed to take place.

We conclude that the *PGA* that caused the damage was between 1.5 and 2 *g*, implying high amplification factors at the site, as the highest anticipated *PGA* at the site, calculated by attenuation relationship, is expected to be lower by an order of magnitude at the site for typical seismicity of the region at large. We argue that the obtained amplification must result from the existence of a layer of loose archeological fill material between the bedrock and the bridge foundations, with geomechanical properties similar to those of alluvium. In light of these findings, namely the high amplification value obtained by us by numerical backward analysis, we conclude that the seismic risk map provided by the Israeli Building Code 413 is found wanting, as we demonstrate in this case that local amplifications play a very significant role in structural deformation during shaking in the old city of Jerusalem.

6.4 Outstanding issues

The research described in this dissertation holds several outstanding issues that are important for solving the problems described, but could not be addresses at this stage.

First, the use of the Discontinuous Deformation Analysis method restricts the stresses and strains to be uniform throughout a block. For the problems addressed in this thesis, where either uniformly shaped and sized blocks were used, as in Chapter 3 and Chapter 5, or single blocks under small loadings, as in Chapter 4, a constant strain assumption is acceptable, since the rigid motion of blocks is dominating. However, when the problem at hand involves block systems with varying shapes and sizes, a constant strain assumption might not be valid, and a finite element type of mesh may provide greater accuracy.

In addition, in the research project of the Western Wall Tunnels, our approach was to model the three-dimensional vault as a two dimensional arch, and we justified this approach by assuming that the vault is in a state of plane stress, because there are no stresses acting on the vault parallel to its axis direction, therefore modeling it as a 2D arch is a reasonable assumption. The plane stress approach however is usually applied to continuous media, and in our case, where a discontinuous block system is modeled, we actually have no possibility to verify the plane stress assumption.

Moreover, regarding the research project of the Western Wall Tunnels, there is absolutely no data measurements in the field, but the geometrical measurements of the keystones of the vault, and the downward displacement of the modeled damaged block. In situ stress measurements in the vault could have verified our plane stress assumption for modeling the three-dimensional vault as a two-dimensional arch, and experimental on-site measurements of background noise, as performed in Avdat National Park, could have led to better assessments of site specific resonance frequency and amplifications. At the time this research was carried out such data did not exist, therefore could not be of use.

And finally regarding the Western Wall Tunnels research project, the appropriate way to model the vault is no doubt as a three-dimensional structure, as also implied by the deformations in the field. This modeling approach was actually attempted, but as the current version of the 3D-DDA code is limited in its capability to solve multi-block systems effectively, and a very small time step is required along with a dynamic parameter smaller than 1 (see section 2.1.3 and 2.2.3), the accumulation of displacements could not be achieved. Naturally, the reduction of the model to a 2-dimensional one introduces some of the problems stated above. Modeling the structures in 3D could not be performed at the moment, but should definitely be attempted in the future, once the 3D-DDA code is improved.

6.5 Recommendation for future research

As would be derived from section 6.4, future research can shed some light on outstanding issues that have not been addressed in this thesis for the reasons stated above.

Once the 3D-DDA code is improved, and proves capable of solving multi-block systems with dynamic parameter of unity, the vault at the Western Wall Tunnels can be re-modeled and investigated in 3D, as well as the research project at the city of L'Aquila, which can only be modeled in 3D.

Furthermore, a more robust site-response analysis at the Western Wall tunnels in the Old City of Jerusalem can better estimate the amplification effects beneath the vaults, and the seismic hazard they introduce. Such analysis can be performed with SHAKE, or a two-dimensional site response program, once there are good estimations for the rock and soil parameters and the subsurface geometry, or with two-dimensional DDA as shown by Bao et al. (in press), and such a numerical analysis should be verified by an experimental site response analysis, as the one performed at Avdat National Park.

Appendix A: complete derivation of the boundary between toppling and sliding + toppling, for the problem of block on an incline subjected to pseudo-static force

For boundary 4, which is a dynamic boundary between toppling and toppling with sliding, the block is toppling, and on the verge of sliding, i.e. friction is limiting. There are four unknown variables, N, ϕ, $\ddot{u}$ and θ, therefore four equations must be derived:

Forces in the downslope direction:

$$F\cos\alpha + W\sin\alpha = N\tan\phi + m\ddot{u}\cos\delta$$ Equation A.01

Forces perpendicular to slope:

$$F\sin\alpha + N = W\cos\alpha + m\ddot{u}\sin\delta$$ Equation A.2

Moments about the centroid:

$$\frac{1}{2}Nh\tan\phi = \frac{1}{2}Nb + \frac{1}{12}m\left(h^2 + b^2\right)\ddot{\theta}$$ Equation A.3

And the relationship between the linear acceleration and rotational acceleration:

$$\ddot{u} = \frac{1}{2}\ddot{\theta}\sqrt{h^2 + b^2}$$ Equation A.4

Remembering that

$$h^2 + b^2 = h^2\left(1 + \frac{b^2}{h^2}\right) = h^2\left(1 + \tan^2\delta\right) = \frac{h^2}{\cos^2\delta}$$ Equation A.5

Eq. A.4 can be re-written as:

$$\ddot{u} = \frac{\ddot{\theta}h}{2\cos\delta}$$ Equation A.6

$$\ddot{\theta} = \frac{2\ddot{u}\cos\delta}{h}$$ Equation A.7

Inserting Eq. A.7 into Eq. A.3:

$$N(h\tan\phi - b) = \frac{m}{6}\frac{h^2}{\cos^2\delta}\frac{2\ddot{u}\cos\delta}{h} = \frac{mh\ddot{u}}{3\cos\delta}$$ Equation A.8

$$m\ddot{u} = N\frac{3\cos\delta(h\tan\phi - b)}{h} = 3N\cos\delta\left(\tan\phi - \frac{b}{h}\right) = 3N\cos\delta(\tan\phi - \tan\delta)$$ Equation A.9

Remembering that $F = W\tan\beta$, and inserting Eq. A.9, Eq. A.1 becomes

$$W\tan\beta\cos\alpha + W\sin\alpha = N\left[\tan\phi + 3\cos^2\delta(\tan\phi - \tan\delta)\right]$$

$$N = \frac{W(\tan\beta\cos\alpha + \sin\alpha)}{\tan\phi + 3\cos^2\delta(\tan\phi - \tan\delta)}$$ Equation A.10

Inserting Eq. A.10 and A.9 into Eq. A.2 yields:

$$W\tan\beta\sin\alpha + \frac{W(\tan\beta\cos\alpha + \sin\alpha)}{\tan\phi + 3\cos^2\delta(\tan\phi - \tan\delta)} = W\cos\alpha + \frac{3W(\tan\beta\cos\alpha + \sin\alpha)\sin\delta\cos\delta(\tan\phi - \tan\delta)}{\tan\phi + 3\cos^2\delta(\tan\phi - \tan\delta)}$$ Equation A.11

Finding a common denominator and getting rid of it on both sides of equation:

$$\begin{aligned}&3\sin\alpha\cos^2\delta(\tan\phi - \tan\delta)\tan\beta + \sin\alpha\tan\phi\tan\beta + \sin\alpha + \cos\alpha\tan\beta = \\ &3\cos\alpha\cos^2\delta(\tan\phi - \tan\delta) + \cos\alpha\tan\phi + 3\sin\delta\cos\delta(\cos\alpha\tan\beta + \sin\alpha)(\tan\phi - \tan\delta)\end{aligned}$$ Equation A.12

The left hand side of Eq. A.12 becomes:

$$\tan\phi(\sin\alpha\tan\beta + 3\sin\alpha\cos^2\delta\tan\beta) - 3\sin\alpha\sin\delta\cos\delta\tan\beta + \cos\alpha\tan\beta + \sin\alpha$$

The right hand side of Eq. A.12 becomes:

$$\begin{aligned}&\tan\phi(3\cos\alpha\cos^2\delta + \cos\alpha + 3\sin\delta\cos\delta\cos\alpha\tan\beta + 3\sin\delta\cos\delta\sin\alpha) - 3\cos\alpha\sin\delta\cos\delta \\ &- 3\sin^2\delta\cos\alpha\tan\beta - 3\sin^2\delta\sin\alpha\end{aligned}$$

Combining from both sides of Eq. A.12 all the expressions multiplied by tanϕ:

$$3\sin\alpha\tan\beta\cos^2\delta + \sin\alpha\tan\beta - 3\sin\delta\cos\delta\sin\alpha - 3\sin\delta\cos\delta\cos\alpha\tan\beta - 3\cos\alpha\cos^2\delta - \cos\alpha$$

Multiplying by cosβ:

$$3\sin\alpha\sin\beta\cos^2\delta+\sin\alpha\sin\beta-3\sin\delta\cos\delta\sin\alpha\cos\beta-3\sin\delta\cos\delta\cos\alpha\sin\beta$$
$$-3\cos\alpha\cos^2\delta\cos\beta-\cos\alpha\cos\beta=$$
$$=3\cos^2\delta(\sin\alpha\sin\beta-\cos\alpha\cos\beta)-3\sin\delta\cos\delta(\sin\alpha\cos\beta+\cos\alpha\sin\beta)+\sin\alpha\sin\beta-\cos\alpha\cos\beta=$$
$$=-3\cos^2\delta\cos(\alpha+\beta)-3\sin\delta\cos\delta\sin(\alpha+\beta)-\cos(\alpha+\beta)$$

Combining from both sides of Eq. A.12 all the expressions that are not multiplied by tanϕ:

$$3\left(\sin\alpha\tan\beta\sin\delta\cos\delta-\sin^2\delta\sin\alpha-\sin^2\delta\cos\alpha\tan\beta-\cos\alpha\sin\delta\cos\delta\right)-\sin\alpha-\cos\alpha\tan\beta$$

Multiplying by cosβ:

$$3\left(\sin\alpha\sin\beta\sin\delta\cos\delta-\sin^2\delta\sin\alpha\cos\beta-\sin^2\delta\cos\alpha\sin\beta-\cos\alpha\sin\delta\cos\delta\cos\beta\right)$$
$$-\sin\alpha\cos\beta-\cos\alpha\sin\beta=$$
$$=3\left[\sin\delta\cos\delta(\sin\alpha\sin\beta-\cos\alpha\cos\beta)-\sin^2\delta(\sin\alpha\cos\beta+\cos\alpha\sin\beta)\right]-\sin\alpha\cos\beta-\cos\alpha\sin\beta=$$
$$=3\left[-\sin\delta\cos\delta\cos(\alpha+\beta)-\sin^2\delta\sin(\alpha+\beta)\right]-\sin(\alpha+\beta)$$

Combining both expressions:

$$\tan\phi=\frac{3\left[\sin\delta\cos\delta\cos(\alpha+\beta)+\sin^2\delta\sin(\alpha+\beta)\right]+\sin(\alpha+\beta)}{3\left[\sin\delta\cos\delta\sin(\alpha+\beta)+\cos^2\delta\cos(\alpha+\beta)\right]+\cos(\alpha+\beta)}=\frac{3\sin\delta\left[\cos\delta\cos(\alpha+\beta)+\sin\delta\sin(\alpha+\beta)\right]+\sin(\alpha+\beta)}{3\cos\delta\left[\cos\delta\cos(\alpha+\beta)+\sin\delta\sin(\alpha+\beta)\right]+\cos(\alpha+\beta)}$$

Equation A.13

And finally:

$$\tan\phi=\frac{3\sin\delta\cos\left[\delta-(\alpha+\beta)\right]+\sin(\alpha+\beta)}{3\cos\delta\cos\left[\delta-(\alpha+\beta)\right]+\cos(\alpha+\beta)}$$

Equation A.14

Appendix B: List of numerical simulations performed for Chapter 5

The table spanning over the next 10 pages lists the simulations carried out for the research of Chapter 5. The shaded simulations are those considered relevant for the damage observed to block 11.

#	over-burden scheme	PGA (g)	over-burden removed from block #	friction angle (o)	classification	#	over-burden scheme	PGA (g)	over-burden removed from block #	friction angle (o)	classification
1	light	-	-	8	3	51	light	3.5	-	45	3
2	light	-	-	9	1	52	light	4	-	15	3
3	heavy	-	-	11	3	53	light	4	-	20	3
4	heavy	-	-	12	1	54	light	4	-	25	3
5	light	0.5	-	9	2	55	light	4	-	30	3
6	light	0.5	-	10	2	56	light	4	-	35	3
7	light	0.5	-	11	1	57	light	4	-	40	2
8	light	0.5	-	12	1	58	light	4	-	45	3
9	light	0.5	-	15	1	59	light	4.5	-	15	3
10	light	0.5	-	20	1	60	light	4.5	-	20	3
11	light	1	-	9	3	61	light	4.5	-	25	3
12	light	1	-	10	3	62	light	4.5	-	30	3
13	light	1	-	11	2	63	light	4.5	-	35	3
14	light	1	-	12	2	64	light	4.5	-	40	3
15	light	1	-	13	2	65	light	4.5	-	45	3
16	light	1	-	14	1	66	light	5	-	15	3
17	light	1	-	15	1	67	light	5	-	20	3
18	light	1	-	20	1	68	light	5	-	25	3
19	light	1.5	-	9	3	69	light	5	-	30	2
20	light	1.5	-	10	3	70	light	5	-	35	3
21	light	1.5	-	11	3	71	light	5	-	40	2
22	light	1.5	-	12	3	72	light	5	-	45	2
23	light	1.5	-	15	2	73	heavy	0.5	-	12	1
24	light	1.5	-	20	1	74	heavy	0.5	-	15	1
25	light	2	-	9	3	75	heavy	1	-	12	1
26	light	2	-	10	3	76	heavy	1	-	15	1
27	light	2	-	15	2	77	heavy	1	-	20	1
28	light	2	-	20	2	78	heavy	1.5	-	12	2
29	light	2	-	25	1	79	heavy	1.5	-	13	1
30	light	2	-	30	1	80	heavy	1.5	-	15	1
31	light	2.5	-	10	3	81	heavy	1.5	-	20	1
32	light	2.5	-	15	2	82	heavy	2	-	12	3
33	light	2.5	-	20	2	83	heavy	2	-	13	1
34	light	2.5	-	25	2	84	heavy	2	-	15	1
35	light	2.5	-	30	2	85	heavy	2	-	20	1
36	light	2.5	-	35	2	86	heavy	2	-	30	1
37	light	2.5	-	40	1	87	heavy	2	-	40	1
38	light	3	-	15	3	88	heavy	2.5	-	12	3
39	light	3	-	20	2	89	heavy	2.5	-	13	2
40	light	3	-	25	3	90	heavy	2.5	-	14	1
41	light	3	-	30	3	91	heavy	2.5	-	15	1
42	light	3	-	35	3	92	heavy	2.5	-	20	1
43	light	3	-	40	3	93	heavy	2.5	-	30	1
44	light	3	-	45	1	94	heavy	2.5	-	40	1
45	light	3.5	-	15	3	95	heavy	3	-	12	3
46	light	3.5	-	20	3	96	heavy	3	-	13	3
47	light	3.5	-	25	3	97	heavy	3	-	14	2
48	light	3.5	-	30	3	98	heavy	3	-	15	1
49	light	3.5	-	35	3	99	heavy	3	-	20	1
50	light	3.5	-	40	3	100	heavy	3	-	30	1

#	over-burden scheme	PGA (g)	over-burden removed from block #	friction angle (o)	classification
101	heavy	3	-	40	1
102	heavy	3.5	-	12	3
103	heavy	3.5	-	13	3
104	heavy	3.5	-	14	3
105	heavy	3.5	-	15	2
106	heavy	3.5	-	20	1
107	heavy	3.5	-	30	1
108	heavy	3.5	-	40	1
109	heavy	4	-	12	3
110	heavy	4	-	13	3
111	heavy	4	-	14	3
112	heavy	4	-	15	2
113	heavy	4	-	20	1
114	heavy	4	-	25	1
115	heavy	4	-	30	1
116	heavy	4	-	35	1
117	heavy	4	-	40	1
118	heavy	4.5	-	12	3
119	heavy	4.5	-	13	3
120	heavy	4.5	-	14	3
121	heavy	4.5	-	15	3
122	heavy	4.5	-	16	3
123	heavy	4.5	-	17	2
124	heavy	4.5	-	18	1
125	heavy	4.5	-	20	1
126	heavy	4.5	-	25	1
127	heavy	4.5	-	30	1
128	heavy	4.5	-	35	1
129	heavy	4.5	-	40	1
130	heavy	5	-	12	3
131	heavy	5	-	15	3
132	heavy	5	-	17	3
133	heavy	5	-	18	2
134	heavy	5	-	20	1
135	heavy	5	-	25	1
136	heavy	5	-	30	1
137	heavy	5	-	35	1
138	heavy	5	-	40	1
139	light	-	2	9	2
140	light	-	2	10	1
141	light	-	2	15	1
142	light	-	3	9	2
143	light	-	3	10	1
144	light	-	3	15	1
145	light	-	4	9	3
146	light	-	4	10	1
147	light	-	4	15	1
148	light	-	5	9	3
149	light	-	5	10	1
150	light	-	5	15	1
151	light	-	6	9	2
152	light	-	6	10	1
153	light	-	6	15	1
154	light	-	7	9	1
155	light	-	7	10	1
156	light	-	7	15	1
157	light	-	8	9	1
158	light	-	8	10	1
159	light	-	8	15	1
160	light	-	8	20	1

#	over-burden scheme	PGA (g)	over-burden removed from block #	friction angle (o)	classification
161	light	-	9	9	1
162	light	-	9	10	1
163	light	-	9	15	1
164	light	-	9	20	1
165	light	-	10	9	1
166	light	-	10	10	1
167	light	-	10	15	1
168	light	-	10	20	1
169	light	-	10	25	1
170	light	-	10	30	1
171	light	-	10	35	1
172	light	-	10	40	1
173	light	-	11	9	1
174	light	-	11	10	1
175	light	-	11	11	1
176	light	-	11	12	1
177	light	-	11	15	1
178	light	-	11	20	1
179	light	-	11	25	1
180	light	-	11	30	1
181	light	-	11	35	1
182	light	-	11	40	1
183	light	-	12	9	3
184	light	-	12	10	1
185	light	-	12	11	1
186	light	-	12	12	1
187	light	-	12	15	1
188	light	-	12	20	1
189	light	-	12	25	1
190	light	-	12	30	1
191	light	-	12	35	1
192	light	-	12	40	1
193	light	-	13	9	3
194	light	-	13	10	3
195	light	-	13	11	3
196	light	-	13	12	1
197	light	-	13	15	1
198	light	-	13	20	1
199	light	-	13	25	1
200	light	-	13	30	1
201	light	-	13	35	1
202	light	-	13	40	1
203	light	-	14	9	3
204	light	-	14	10	3
205	light	-	14	11	1
206	light	-	14	12	1
207	light	-	14	15	1
208	light	-	14	20	1
209	light	-	15	9	3
210	light	-	15	10	3
211	light	-	15	11	1
212	light	-	15	12	1
213	light	-	15	15	1
214	light	-	16	9	3
215	light	-	16	10	3
216	light	-	16	11	1
217	light	-	16	12	1
218	light	-	16	13	1
219	light	-	16	15	1
220	light	-	17	9	3

#	over-burden scheme	PGA (g)	over-burden removed from block #	friction angle (o)	classification
221	light	-	17	10	2
222	light	-	17	11	1
223	light	-	17	15	1
224	light	-	18	9	3
225	light	-	18	10	3
226	light	-	18	11	1
227	light	-	18	12	1
228	light	-	18	13	1
229	light	-	18	15	1
230	heavy	-	2	12	1
231	heavy	-	2	15	1
232	heavy	-	2	20	1
233	heavy	-	3	12	1
234	heavy	-	3	15	1
235	heavy	-	3	20	1
236	heavy	-	4	12	1
237	heavy	-	4	15	1
238	heavy	-	4	20	1
239	heavy	-	5	12	1
240	heavy	-	5	15	1
241	heavy	-	5	20	1
242	heavy	-	6	12	1
243	heavy	-	6	15	1
244	heavy	-	6	20	1
245	heavy	-	7	12	1
246	heavy	-	7	15	1
247	heavy	-	7	20	1
248	heavy	-	8	12	1
249	heavy	-	8	15	1
250	heavy	-	8	20	1
251	heavy	-	9	12	1
252	heavy	-	9	15	1
253	heavy	-	9	20	1
254	heavy	-	10	12	1
255	heavy	-	10	15	1
256	heavy	-	10	20	1
257	heavy	-	11	12	1
258	heavy	-	11	15	1
259	heavy	-	11	20	1
260	heavy	-	12	12	3
261	heavy	-	12	13	1
262	heavy	-	12	15	1
263	heavy	-	12	20	1
264	heavy	-	13	12	3
265	heavy	-	13	13	3
266	heavy	-	13	14	1
267	heavy	-	13	15	1
268	heavy	-	13	20	1
269	heavy	-	14	12	3
270	heavy	-	14	13	3
271	heavy	-	14	14	1
272	heavy	-	14	15	1
273	heavy	-	14	20	1
274	heavy	-	15	12	3
275	heavy	-	15	13	3
276	heavy	-	15	14	3
277	heavy	-	15	15	3
278	heavy	-	15	16	1
279	heavy	-	15	20	1
280	heavy	-	16	12	3

#	over-burden scheme	PGA (g)	over-burden removed from block #	friction angle (o)	classification
281	heavy	-	16	13	3
282	heavy	-	16	14	2
283	heavy	-	16	15	3
284	heavy	-	16	16	1
285	heavy	-	16	20	1
286	heavy	-	17	12	3
287	heavy	-	17	13	3
288	heavy	-	17	14	1
289	heavy	-	17	15	1
290	heavy	-	17	20	1
291	heavy	-	18	12	3
292	heavy	-	18	13	1
293	heavy	-	18	15	1
294	heavy	-	18	20	1
295	light	0.5	5	10	3
296	light	0.5	5	11	1
297	light	0.5	5	15	1
298	light	1	5	10	2
299	light	1	5	11	2
300	light	1	5	13	1
301	light	1.5	5	10	3
302	light	1.5	5	11	3
303	light	1.5	5	13	2
304	light	1.5	5	15	2
305	light	1.5	5	20	1
306	light	2	5	12	3
307	light	2	5	14	2
308	light	2	5	15	2
309	light	2	5	20	2
310	light	2	5	30	1
311	light	2.5	5	14	3
312	light	2.5	5	15	3
313	light	2.5	5	17	3
314	light	2.5	5	20	3
315	light	2.5	5	25	3
316	light	2.5	5	30	3
317	light	2.5	5	35	3
318	light	2.5	5	40	3
319	light	3	5	15	3
320	light	3	5	20	3
321	light	3	5	25	3
322	light	3	5	30	3
323	light	3	5	35	3
324	light	3	5	40	3
325	light	3.5	5	15	3
326	light	3.5	5	20	3
327	light	3.5	5	25	3
328	light	3.5	5	30	3
329	light	3.5	5	35	3
330	light	3.5	5	40	3
331	light	4	5	15	3
332	light	4	5	20	3
333	light	4	5	25	3
334	light	4	5	30	3
335	light	4	5	35	3
336	light	4	5	40	3
337	light	4.5	5	15	3
338	light	4.5	5	20	3
339	light	4.5	5	25	3
340	light	4.5	5	30	3

#	over-burden scheme	PGA (g)	over-burden removed from block #	friction angle (o)	classification
341	light	4.5	5	35	3
342	light	4.5	5	40	3
343	light	5	5	15	3
344	light	5	5	20	3
345	light	5	5	25	3
346	light	5	5	30	3
347	light	5	5	35	2
348	light	5	5	40	3
349	light	0.5	6	9	3
350	light	0.5	6	10	1
351	light	0.5	6	15	1
352	light	1	6	9	3
353	light	1	6	10	3
354	light	1	6	11	2
355	light	1	6	15	1
356	light	1.5	6	10	3
357	light	1.5	6	11	3
358	light	1.5	6	13	2
359	light	1.5	6	15	2
360	light	2	6	12	3
361	light	2	6	13	3
362	light	2	6	14	2
363	light	2	6	15	2
364	light	2	6	20	2
365	light	2	6	25	3
366	light	2	6	30	3
367	light	2	6	35	3
368	light	2	6	40	1
369	light	2.5	6	14	3
370	light	2.5	6	15	3
371	light	2.5	6	20	3
372	light	2.5	6	25	3
373	light	2.5	6	30	3
374	light	2.5	6	35	3
375	light	2.5	6	40	3
376	light	3	6	15	3
377	light	3	6	20	3
378	light	3	6	25	3
379	light	3	6	30	3
380	light	3	6	35	3
381	light	3	6	40	3
382	light	3.5	6	15	3
383	light	3.5	6	20	3
384	light	3.5	6	25	3
385	light	3.5	6	30	3
386	light	3.5	6	35	3
387	light	3.5	6	40	3
388	light	4	6	15	3
389	light	4	6	20	3
390	light	4	6	25	3
391	light	4	6	30	3
392	light	4	6	35	3
393	light	4	6	40	3
394	light	4.5	6	15	3
395	light	4.5	6	20	3
396	light	4.5	6	25	3
397	light	4.5	6	30	3
398	light	4.5	6	35	3
399	light	4.5	6	40	3
400	light	5	6	15	3
401	light	5	6	20	3
402	light	5	6	25	3
403	light	5	6	30	3
404	light	5	6	35	3
405	light	0.5	7	9	2
406	light	0.5	7	10	1
407	light	0.5	7	15	1
408	light	1	7	9	3
409	light	1	7	10	3
410	light	1	7	11	2
411	light	1	7	12	2
412	light	1	7	13	2
413	light	1	7	15	1
414	light	1	7	25	1
415	light	1.5	7	9	3
416	light	1.5	7	10	3
417	light	1.5	7	12	2
418	light	1.5	7	15	2
419	light	1.5	7	20	1
420	light	2	7	11	3
421	light	2	7	13	3
422	light	2	7	14	2
423	light	2	7	15	2
424	light	2	7	20	3
425	light	2	7	25	1
426	light	2	7	30	2
427	light	2	7	35	1
428	light	2	7	40	1
429	light	2.5	7	14	3
430	light	2.5	7	15	3
431	light	2.5	7	17	2
432	light	2.5	7	20	3
433	light	2.5	7	25	3
434	light	2.5	7	30	3
435	light	2.5	7	35	3
436	light	2.5	7	40	3
437	light	3	7	14	3
438	light	3	7	15	2
439	light	3	7	16	2
440	light	3	7	20	3
441	light	3	7	25	3
442	light	3	7	30	3
443	light	3	7	35	3
444	light	3	7	40	3
445	light	3.5	7	14	3
446	light	3.5	7	15	3
447	light	3.5	7	20	3
448	light	3.5	7	25	3
449	light	3.5	7	30	3
450	light	3.5	7	35	3
451	light	3.5	7	40	3
452	light	4	7	15	3
453	light	4	7	20	3
454	light	4	7	25	3
455	light	4	7	30	3
456	light	4	7	35	3
457	light	4	7	40	3
458	light	4.5	7	15	3
459	light	4.5	7	20	3
460	light	4.5	7	25	3

#	over-burden scheme	PGA (g)	over-burden removed from block #	friction angle (o)	classification
461	light	4.5	7	30	3
462	light	4.5	7	35	3
463	light	4.5	7	40	3
464	light	5	7	15	3
465	light	5	7	20	3
466	light	5	7	25	3
467	light	5	7	30	3
468	light	5	7	35	3
469	light	5	7	40	3
470	light	0.5	8	9	2
471	light	0.5	8	10	1
472	light	0.5	8	15	1
473	light	1	8	9	3
474	light	1	8	10	2
475	light	1	8	11	2
476	light	1	8	15	1
477	light	1.5	8	9	3
478	light	1.5	8	10	3
479	light	1.5	8	11	3
480	light	1.5	8	12	2
481	light	1.5	8	13	2
482	light	1.5	8	14	2
483	light	1.5	8	15	2
484	light	1.5	8	20	1
485	light	1.5	8	30	1
486	light	2	8	11	3
487	light	2	8	12	3
488	light	2	8	13	2
489	light	2	8	14	2
490	light	2	8	15	2
491	light	2	8	20	2
492	light	2	8	25	2
493	light	2	8	30	3
494	light	2	8	40	3
495	light	2.5	8	13	3
496	light	2.5	8	14	3
497	light	2.5	8	15	3
498	light	2.5	8	16	3
499	light	2.5	8	17	3
500	light	2.5	8	18	3
501	light	2.5	8	20	3
502	light	2.5	8	30	3
503	light	2.5	8	40	3
504	light	3	8	15	3
505	light	3	8	20	3
506	light	3	8	25	3
507	light	3	8	30	3
508	light	3	8	35	3
509	light	3	8	40	3
510	light	3.5	8	15	3
511	light	3.5	8	20	3
512	light	3.5	8	25	3
513	light	3.5	8	30	3
514	light	3.5	8	35	3
515	light	3.5	8	40	3
516	light	4	8	15	3
517	light	4	8	20	3
518	light	4	8	25	3
519	light	4	8	30	3
520	light	4	8	35	3
521	light	4	8	40	3
522	light	4.5	8	15	3
523	light	4.5	8	20	3
524	light	4.5	8	25	3
525	light	4.5	8	30	3
526	light	4.5	8	35	3
527	light	4.5	8	40	3
528	light	5	8	15	3
529	light	5	8	20	3
530	light	5	8	25	3
531	light	5	8	30	3
532	light	5	8	35	3
533	light	5	8	40	3
534	light	0.5	9	9	2
535	light	0.5	9	10	1
536	light	0.5	9	11	1
537	light	0.5	9	15	1
538	light	1	9	9	3
539	light	1	9	10	3
540	light	1	9	11	2
541	light	1	9	12	2
542	light	1	9	15	1
543	light	1	9	20	1
544	light	1.5	9	9	3
545	light	1.5	9	11	3
546	light	1.5	9	13	2
547	light	1.5	9	15	2
548	light	1.5	9	20	1
549	light	1.5	9	30	1
550	light	2	9	11	3
551	light	2	9	13	2
552	light	2	9	15	2
553	light	2	9	20	2
554	light	2	9	30	1
555	light	2.5	9	12	3
556	light	2.5	9	13	3
557	light	2.5	9	15	2
558	light	2.5	9	17	2
559	light	2.5	9	20	3
560	light	2.5	9	25	3
561	light	2.5	9	30	3
562	light	2.5	9	35	3
563	light	2.5	9	40	3
564	light	3	9	14	2
565	light	3	9	15	2
566	light	3	9	17	2
567	light	3	9	20	2
568	light	3	9	25	3
569	light	3	9	30	3
570	light	3	9	35	3
571	light	3	9	40	3
572	light	3.5	9	14	3
573	light	3.5	9	15	3
574	light	3.5	9	18	3
575	light	3.5	9	20	2
576	light	3.5	9	25	1
577	light	3.5	9	30	3
578	light	3.5	9	35	3
579	light	3.5	9	40	3
580	light	4	9	15	3

#	over-burden scheme	PGA (g)	over-burden removed from block #	friction angle (o)	classification
581	light	4	9	20	2
582	light	4	9	25	3
583	light	4	9	30	3
584	light	4	9	35	3
585	light	4	9	40	3
586	light	4.5	9	15	3
587	light	4.5	9	20	3
588	light	4.5	9	25	3
589	light	4.5	9	30	3
590	light	4.5	9	35	3
591	light	4.5	9	40	2
592	light	5	9	15	3
593	light	5	9	20	3
594	light	5	9	25	3
595	light	5	9	30	2
596	light	5	9	35	3
597	light	5	9	40	3
598	light	0.5	10	9	2
599	light	0.5	10	10	1
600	light	1	10	9	3
601	light	1	10	10	2
602	light	1	10	11	2
603	light	1	10	15	1
604	light	1.5	10	10	3
605	light	1.5	10	11	3
606	light	1.5	10	13	2
607	light	1.5	10	15	2
608	light	2	10	12	3
609	light	2	10	14	2
610	light	2	10	15	2
611	light	2	10	20	1
612	light	2.5	10	13	3
613	light	2.5	10	15	2
614	light	2.5	10	17	1
615	light	2.5	10	20	1
616	light	3	10	14	3
617	light	3	10	15	2
618	light	3	10	16	2
619	light	3	10	20	3
620	light	3	10	25	3
621	light	3	10	30	2
622	light	3	10	35	3
623	light	3	10	40	3
624	light	3.5	10	15	3
625	light	3.5	10	20	2
626	light	3.5	10	25	2
627	light	3.5	10	30	3
628	light	3.5	10	31	2
629	light	3.5	10	32	2
630	light	3.5	10	33	2
631	light	3.5	10	34	2
632	light	3.5	10	35	1
633	light	3.5	10	40	3
634	light	4	10	15	3
635	light	4	10	20	2
636	light	4	10	25	3
637	light	4	10	30	2
638	light	4	10	35	3
639	light	4	10	40	2
640	light	4.5	10	15	3

#	over-burden scheme	PGA (g)	over-burden removed from block #	friction angle (o)	classification
641	light	4.5	10	20	2
642	light	4.5	10	25	2
643	light	4.5	10	30	3
644	light	4.5	10	35	2
645	light	4.5	10	40	2
646	light	5	10	15	3
647	light	5	10	20	3
648	light	5	10	25	2
649	light	5	10	30	2
650	light	5	10	35	2
651	light	5	10	40	3
652	light	0.5	11	9	2
653	light	0.5	11	11	1
654	light	0.5	11	15	1
655	light	0.5	11	20	1
656	light	1	11	9	3
657	light	1	11	10	2
658	light	1	11	13	2
659	light	1	11	15	1
660	light	1	11	20	1
661	light	1.5	11	10	3
662	light	1.5	11	11	3
663	light	1.5	11	12	2
664	light	1.5	11	15	2
665	light	1.5	11	20	1
666	light	2	11	12	2
667	light	2	11	15	2
668	light	2	11	20	1
669	light	2	11	25	1
670	light	2.5	11	12	3
671	light	2.5	11	14	3
672	light	2.5	11	15	2
673	light	2.5	11	20	2
674	light	2.5	11	25	2
675	light	2.5	11	30	2
676	light	2.5	11	35	2
677	light	3	11	15	2
678	light	3	11	17	2
679	light	3	11	18	2
680	light	3	11	19	2
681	light	3	11	20	2
682	light	3	11	25	2
683	light	3	11	30	2
684	light	3	11	35	1
685	light	3	11	40	1
686	light	3.5	11	15	3
687	light	3.5	11	17	2
688	light	3.5	11	20	2
689	light	3.5	11	25	2
690	light	3.5	11	30	2
691	light	3.5	11	35	2
692	light	4	11	15	3
693	light	4	11	17	3
694	light	4	11	20	2
695	light	4	11	25	2
696	light	4	11	30	2
697	light	4	11	35	3
698	light	4	11	40	3
699	light	4.5	11	15	3
700	light	4.5	11	17	2

#	over-burden scheme	PGA (g)	over-burden removed from block #	friction angle (o)	classification	#	over-burden scheme	PGA (g)	over-burden removed from block #	friction angle (o)	classification
701	light	4.5	11	18	3	761	light	4	12	40	3
702	light	4.5	11	19	2	762	light	4.5	12	15	3
703	light	4.5	11	20	2	763	light	4.5	12	20	2
704	light	4.5	11	21	2	764	light	4.5	12	25	3
705	light	4.5	11	22	3	765	light	4.5	12	30	2
706	light	4.5	11	25	3	766	light	4.5	12	35	2
707	light	4.5	11	30	3	767	light	4.5	12	40	2
708	light	4.5	11	35	2	768	light	5	12	15	3
709	light	4.5	11	40	2	769	light	5	12	20	2
710	light	5	11	15	3	770	light	5	12	25	2
711	light	5	11	20	3	771	light	5	12	30	3
712	light	5	11	25	2	772	light	5	12	35	2
713	light	5	11	30	3	773	light	5	12	40	2
714	light	5	11	35	2	774	light	0.5	13	9	3
715	light	0.5	12	9	3	775	light	0.5	13	10	2
716	light	0.5	12	10	2	776	light	0.5	13	13	1
717	light	0.5	12	15	1	777	light	0.5	13	15	1
718	light	1	12	9	3	778	light	0.5	13	30	1
719	light	1	12	10	3	779	light	1	13	10	3
720	light	1	12	13	2	780	light	1	13	13	2
721	light	1	12	15	1	781	light	1	13	15	2
722	light	1	12	20	1	782	light	1	13	20	1
723	light	1.5	12	11	2	783	light	1.5	13	11	3
724	light	1.5	12	13	2	784	light	1.5	13	13	2
725	light	1.5	12	15	2	785	light	1.5	13	15	2
726	light	1.5	12	20	1	786	light	1.5	13	20	1
727	light	1.5	12	30	1	787	light	1.5	13	25	1
728	light	2	12	11	3	788	light	1.5	13	30	1
729	light	2	12	13	3	789	light	1.5	13	35	1
730	light	2	12	15	2	790	light	2	13	12	3
731	light	2	12	20	2	791	light	2	13	15	2
732	light	2	12	25	2	792	light	2	13	20	2
733	light	2	12	30	2	793	light	2	13	25	3
734	light	2	12	35	2	794	light	2	13	30	3
735	light	2.5	12	14	2	795	light	2	13	35	3
736	light	2.5	12	15	2	796	light	2	13	40	3
737	light	2.5	12	20	2	797	light	2.5	13	13	3
738	light	2.5	12	25	2	798	light	2.5	13	14	3
739	light	2.5	12	30	3	799	light	2.5	13	15	3
740	light	2.5	12	35	1	800	light	2.5	13	20	2
741	light	2.5	12	40	3	801	light	2.5	13	25	3
742	light	3	12	14	3	802	light	2.5	13	30	3
743	light	3	12	15	3	803	light	2.5	13	35	1
744	light	3	12	17	3	804	light	2.5	13	40	3
745	light	3	12	20	3	805	light	3	13	15	3
746	light	3	12	25	2	806	light	3	13	20	3
747	light	3	12	30	2	807	light	3	13	25	3
748	light	3	12	35	3	808	light	3	13	30	3
749	light	3	12	40	3	809	light	3	13	35	3
750	light	3.5	12	15	3	810	light	3	13	40	3
751	light	3.5	12	20	2	811	light	3.5	13	15	3
752	light	3.5	12	25	2	812	light	3.5	13	20	3
753	light	3.5	12	30	3	813	light	3.5	13	25	3
754	light	3.5	12	35	3	814	light	3.5	13	30	3
755	light	3.5	12	40	2	815	light	3.5	13	35	3
756	light	4	12	15	3	816	light	3.5	13	40	2
757	light	4	12	20	2	817	light	4	13	15	3
758	light	4	12	25	3	818	light	4	13	20	3
759	light	4	12	30	3	819	light	4	13	25	3
760	light	4	12	35	3	820	light	4	13	30	3

#	over-burden scheme	PGA (g)	over-burden removed from block #	friction angle (o)	classification
821	light	4	13	35	3
822	light	4	13	40	3
823	light	4.5	13	15	3
824	light	4.5	13	20	3
825	light	4.5	13	25	3
826	light	4.5	13	30	3
827	light	4.5	13	35	3
828	light	4.5	13	40	3
829	light	5	13	15	3
830	light	5	13	20	3
831	light	5	13	25	3
832	light	5	13	30	3
833	light	5	13	35	3
834	light	5	13	40	3
835	light	0.5	14	11	3
836	light	0.5	14	12	1
837	light	1	14	11	3
838	light	1	14	12	2
839	light	1	14	13	2
840	light	1	14	15	2
841	light	1	14	20	1
842	light	1.5	14	12	3
843	light	1.5	14	15	2
844	light	1.5	14	18	2
845	light	2	14	13	3
846	light	2	14	15	2
847	light	2	14	17	2
848	light	2	14	18	2
849	light	2	14	20	2
850	light	2.5	14	15	3
851	light	2.5	14	20	3
852	light	2.5	14	23	2
853	light	2.5	14	25	2
854	light	3	14	23	3
855	light	3	14	25	3
856	light	3	14	30	3
857	light	3	14	35	3
858	light	3	14	40	3
859	light	3.5	14	15	3
860	light	3.5	14	20	3
861	light	3.5	14	25	3
862	light	3.5	14	30	3
863	light	3.5	14	35	1
864	light	3.5	14	40	3
865	light	4	14	15	3
866	light	4	14	20	3
867	light	4	14	25	3
868	light	4	14	30	3
869	light	4	14	35	3
870	light	4	14	40	3
871	light	4.5	14	15	3
872	light	4.5	14	20	3
873	light	4.5	14	25	3
874	light	4.5	14	30	3
875	light	4.5	14	35	2
876	light	4.5	14	40	3
877	light	5	14	15	3
878	light	5	14	20	3
879	light	5	14	25	3
880	light	5	14	30	3

#	over-burden scheme	PGA (g)	over-burden removed from block #	friction angle (o)	classification
881	light	5	14	35	3
882	light	5	14	40	3
883	light	0.5	15	11	2
884	light	0.5	15	13	3
885	light	0.5	15	15	1
886	light	1	15	11	3
887	light	1	15	13	2
888	light	1	15	15	2
889	light	1.5	15	12	3
890	light	1.5	15	14	3
891	light	1.5	15	15	2
892	light	1.5	15	16	3
893	light	1.5	15	17	2
894	light	1.5	15	20	1
895	light	2	15	15	3
896	light	2	15	17	3
897	light	2	15	20	3
898	light	2	15	25	3
899	light	2	15	30	2
900	light	2	15	35	3
901	light	2	15	40	3
902	light	2.5	15	15	3
903	light	2.5	15	20	2
904	light	2.5	15	25	3
905	light	2.5	15	30	2
906	light	2.5	15	35	3
907	light	2.5	15	40	3
908	light	3	15	15	3
909	light	3	15	20	3
910	light	3	15	24	3
911	light	3	15	25	2
912	light	3	15	30	3
913	light	3	15	35	3
914	light	3	15	40	2
915	light	3.5	15	15	2
916	light	3.5	15	20	3
917	light	3.5	15	25	2
918	light	3.5	15	30	2
919	light	3.5	15	35	2
920	light	3.5	15	40	3
921	light	4	15	15	3
922	light	4	15	20	3
923	light	4	15	25	3
924	light	4	15	30	3
925	light	4	15	35	3
926	light	4	15	40	3
927	light	4.5	15	15	3
928	light	4.5	15	20	3
929	light	4.5	15	25	3
930	light	4.5	15	30	3
931	light	4.5	15	35	2
932	light	4.5	15	40	3
933	light	5	15	15	3
934	light	5	15	20	3
935	light	5	15	25	3
936	light	5	15	30	3
937	light	5	15	35	2
938	light	5	15	40	3
939	heavy	0.5	5	12	1
940	heavy	1	5	12	1

#	over-burden scheme	PGA (g)	over-burden removed from block #	friction angle (o)	classification
941	heavy	1.5	5	12	1
942	heavy	2	5	12	3
943	heavy	2	5	13	1
944	heavy	2.5	5	13	2
945	heavy	2.5	5	14	1
946	heavy	3	5	13	3
947	heavy	3	5	14	2
948	heavy	3.5	5	14	3
949	heavy	3.5	5	15	2
950	heavy	4	5	15	3
951	heavy	4	5	16	2
952	heavy	4.5	5	16	2
953	heavy	4.5	5	17	2
954	heavy	4.5	5	30	1
955	heavy	5	5	16	3
956	heavy	5	5	17	2
957	heavy	5	5	18	2
958	heavy	5	5	30	1
959	heavy	0.5	6	12	1
960	heavy	1	6	12	1
961	heavy	1.5	6	12	1
962	heavy	2	6	12	2
963	heavy	2.5	6	12	3
964	heavy	2.5	6	13	2
965	heavy	2.5	6	14	1
966	heavy	3	6	13	3
967	heavy	3	6	14	1
968	heavy	3.5	6	14	3
969	heavy	3.5	6	15	1
970	heavy	4	6	14	3
971	heavy	4	6	15	2
972	heavy	4	6	16	1
973	heavy	4.5	6	15	3
974	heavy	4.5	6	16	2
975	heavy	4.5	6	18	1
976	heavy	4.5	6	25	1
977	heavy	5	6	16	3
978	heavy	5	6	17	2
979	heavy	5	6	18	2
980	heavy	5	6	25	1
981	heavy	5	6	30	1
982	heavy	0.5	7	12	1
983	heavy	1	7	12	1
984	heavy	1.5	7	12	1
985	heavy	2	7	12	1
986	heavy	2.5	7	12	3
987	heavy	2.5	7	13	1
988	heavy	2.5	7	14	1
989	heavy	3	7	13	2
990	heavy	3	7	15	1
991	heavy	3.5	7	13	3
992	heavy	3.5	7	14	1
993	heavy	3.5	7	15	1
994	heavy	4	7	14	3
995	heavy	4	7	15	2
996	heavy	4	7	17	1
997	heavy	4.5	7	15	3
998	heavy	4.5	7	16	2
999	heavy	4.5	7	17	1
1000	heavy	5	7	16	3
1001	heavy	5	7	17	2

#	over-burden scheme	PGA (g)	over-burden removed from block #	friction angle (o)	classification
1002	heavy	0.5	8	12	1
1003	heavy	0.5	8	15	1
1004	heavy	0.5	8	20	1
1005	heavy	1	8	12	1
1006	heavy	1	8	15	1
1007	heavy	1	8	20	1
1008	heavy	1.5	8	12	1
1009	heavy	1.5	8	15	1
1010	heavy	1.5	8	20	1
1011	heavy	2	8	12	1
1012	heavy	2	8	15	1
1013	heavy	2	8	20	1
1014	heavy	2.5	8	12	1
1015	heavy	2.5	8	15	1
1016	heavy	2.5	8	20	1
1017	heavy	3	8	12	2
1018	heavy	3	8	15	1
1019	heavy	3	8	20	1
1020	heavy	3.5	8	12	3
1021	heavy	3.5	8	13	2
1022	heavy	3.5	8	14	1
1023	heavy	3.5	8	15	1
1024	heavy	4	8	12	3
1025	heavy	4	8	13	3
1026	heavy	4	8	14	2
1027	heavy	4	8	15	1
1028	heavy	4.5	8	14	3
1029	heavy	4.5	8	15	2
1030	heavy	4.5	8	16	1
1031	heavy	5	8	15	3
1032	heavy	5	8	16	2
1033	heavy	5	8	30	1
1034	heavy	0.5	9	12	1
1035	heavy	1	9	12	1
1036	heavy	1.5	9	12	1
1037	heavy	2	9	12	1
1038	heavy	2.5	9	12	1
1039	heavy	3	9	12	2
1040	heavy	3.5	9	12	3
1041	heavy	3.5	9	13	2
1042	heavy	4	9	13	3
1043	heavy	4	9	14	2
1044	heavy	4.5	9	14	2
1045	heavy	4.5	9	15	2
1046	heavy	5	9	14	3
1047	heavy	5	9	15	2
1048	heavy	0.5	10	12	1
1049	heavy	1	10	12	1
1050	heavy	1.5	10	12	1
1051	heavy	2	10	12	1
1052	heavy	2.5	10	12	2
1053	heavy	3	10	12	2
1054	heavy	3	10	13	2
1055	heavy	3.5	10	12	3
1056	heavy	3.5	10	13	2
1057	heavy	3.5	10	15	1
1058	heavy	4	10	13	3
1059	heavy	4	10	14	2
1060	heavy	4.5	10	14	3
1061	heavy	4.5	10	15	2
1062	heavy	4.5	10	17	1

#	over-burden scheme	PGA (g)	over-burden removed from block #	friction angle (o)	classification
1063	heavy	5	10	15	2
1064	heavy	5	10	16	2
1065	heavy	0.5	11	12	1
1066	heavy	0.5	11	15	1
1067	heavy	0.5	11	20	1
1068	heavy	1	11	12	1
1069	heavy	1	11	15	1
1070	heavy	1	11	20	1
1071	heavy	1.5	11	12	1
1072	heavy	1.5	11	15	1
1073	heavy	2	11	12	1
1074	heavy	2.5	11	12	2
1075	heavy	2.5	11	13	1
1076	heavy	2.5	11	15	1
1077	heavy	3	11	12	3
1078	heavy	3	11	13	2
1079	heavy	3	11	14	1
1080	heavy	3.5	11	13	3
1081	heavy	3.5	11	14	2
1082	heavy	3.5	11	15	1
1083	heavy	4	11	14	3
1084	heavy	4	11	15	2
1085	heavy	4.5	11	15	3
1086	heavy	4.5	11	16	2
1087	heavy	4.5	11	18	1
1088	heavy	5	11	16	2
1089	heavy	5	11	17	2
1090	heavy	5	11	18	2
1091	heavy	5	11	20	1
1092	heavy	0.5	12	13	1
1093	heavy	1	12	13	1
1094	heavy	1.5	12	13	1
1095	heavy	2	12	13	2
1096	heavy	2	12	15	1
1097	heavy	2.5	12	13	3
1098	heavy	2.5	12	14	2
1099	heavy	3	12	14	3
1100	heavy	3	12	15	2
1101	heavy	3.5	12	15	2
1102	heavy	3.5	12	17	1
1103	heavy	4	12	15	3
1104	heavy	4	12	16	2
1105	heavy	4	12	17	1
1106	heavy	4.5	12	16	3
1107	heavy	4.5	12	17	2
1108	heavy	4.5	12	18	1
1109	heavy	5	12	17	3
1110	heavy	5	12	18	2
1111	heavy	5	12	19	2
1112	heavy	0.5	13	14	2
1113	heavy	0.5	13	15	1
1114	heavy	1	13	14	2
1115	heavy	1	13	15	1
1116	heavy	1	13	17	1
1117	heavy	1.5	13	14	2
1118	heavy	1.5	13	15	2
1119	heavy	2	13	14	3
1120	heavy	2	13	15	2
1121	heavy	2.5	13	15	3
1122	heavy	2.5	13	16	2
1123	heavy	2.5	13	17	1

#	over-burden scheme	PGA (g)	over-burden removed from block #	friction angle (o)	classification
1124	heavy	3	13	16	2
1125	heavy	3	13	17	2
1126	heavy	3	13	18	1
1127	heavy	3.5	13	16	3
1128	heavy	3.5	13	17	2
1129	heavy	4	13	17	3
1130	heavy	4	13	18	2
1131	heavy	4.5	13	18	3
1132	heavy	4.5	13	19	2
1133	heavy	5	13	19	3
1134	heavy	5	13	20	2
1135	heavy	0.5	14	14	1
1136	heavy	1	14	14	1
1137	heavy	1.5	14	14	3
1138	heavy	1.5	14	15	1
1139	heavy	2	14	14	3
1140	heavy	2	14	15	2
1141	heavy	2.5	14	15	3
1142	heavy	2.5	14	16	2
1143	heavy	3	14	16	3
1144	heavy	3	14	17	2
1145	heavy	3.5	14	17	3
1146	heavy	3.5	14	18	2
1147	heavy	3.5	14	20	1
1148	heavy	4	14	18	3
1149	heavy	4	14	19	2
1150	heavy	4.5	14	19	3
1151	heavy	4.5	14	20	2
1152	heavy	4.5	14	21	1
1153	heavy	4.5	14	25	1
1154	heavy	4.5	14	30	1
1155	heavy	4.5	14	40	1
1156	heavy	5	14	20	3
1157	heavy	5	14	21	2
1158	heavy	5	14	22	3
1159	heavy	5	14	25	3
1160	heavy	5	14	30	3
1161	heavy	5	14	35	1
1162	heavy	5	14	40	3
1163	heavy	0.5	15	16	1
1164	heavy	1	15	16	1
1165	heavy	1.5	15	16	1
1166	heavy	2	15	16	3
1167	heavy	2	15	17	1
1168	heavy	2.5	15	17	2
1169	heavy	2.5	15	18	1
1170	heavy	3	15	17	3
1171	heavy	3	15	18	3
1172	heavy	3	15	19	1
1173	heavy	3.5	15	18	3
1174	heavy	3.5	15	19	2
1175	heavy	3.5	15	20	1
1176	heavy	4	15	19	3
1177	heavy	4	15	20	2
1178	heavy	4	15	22	1
1179	heavy	4.5	15	20	3
1180	heavy	4.5	15	22	1
1181	heavy	5	15	21	3
1182	heavy	5	15	22	3
1183	heavy	5	15	23	1

References

Adhikary, D. P., Dyskin, A. V., Jewell, R. J., and Stewart, D. P., 1997, A study of the mechanism of flexural toppling failure of rock slopes: Rock Mechanics and Rock Engineering, v. 30, no. 2, p. 75-93.

Ali, Q., Badrashi, Y. I., Ahmad, N., Alam, B., Rehman, S., and Banori, F. A. S., 2012, Experimental investigation on the characterization of solid clay brick masonry for lateral shear strength evaluation: International Journal of Earth Sciences and Engineering, v. 5, no. 4, p. 782-791.

Amini, M., Majdi, A., and Aydan, O., 2009, Stability Analysis and the Stabilization of Flexural Toppling Failure: Rock Mechanics and Rock Engineering, v. 42, no. 5, p. 751-782.

Amini, M., Majdi, A., and Veshadi, M. A., 2012, Stability Analysis of Rock Slopes Against Block-Flexure Toppling Failure: Rock Mechanics and Rock Engineering, v. 45, no. 4, p. 519-532.

Ashby, J. P., 1971, Sliding and Toppling Modes of Failure in Models and Jointed Rock Slopes: University of London, Imperial College.

Ashford, S. A., Sitar, N., Lysmer, J., and Deng, N., 1997, Topographic effects on the seismic response of steep slopes: Bulletin of the Seismological Society of America, v. 87, no. 3, p. 701-709.

Autodesk, 2011, AutoCAD, Autodesk, Inc.

Aydan, O., and Kawamoto, T., 1992, The stability of slopes and underground openings against flexural toppling and their stabilization Rock Mechanics and Rock Engineering, v. 25, no. 3, p. 143-165.

Bahat, D., 1993, The Western Wall Tunnels: Qadmoniot, v. 101-102, p. 38-48 [in Hebrew].

Bahat, D., 2007, New discoveries in the Western Wall Tunnels: Qadmoniot, v. 40, p. 41-47 [in Hebrew].

Bao, H., Yagoda-Biran, G., and Hatzor, Y. H., in press, Site response analysis with two-dimensional numerical discontinuous deformation analysis method: Earthquake Eng. Struct. Dyn.

Barclay, J. T., 1858, The City of the Great King: Philadelphia, James Challen and Sons.

Ben-Menahem, A., 1991, Four thousand years of seismicity along the Dead Sea Rift: J. Geophys. Res., v. 96, no. B12, p. 20,195-20,216.

Beresnev, I. A., and Atkinson, G. M., 1997, Modeling finite-fault radiation from the omega(n) spectrum: Bulletin of the Seismological Society of America, v. 87, no. 1, p. 67-84.

Bobet, A., 1999, Analytical solutions for toppling failure: International Journal of Rock Mechanics and Mining Sciences, v. 36, no. 7, p. 971-980.

Boore, D. M., and Joyner, W. B., 1997, Site amplifications for generic rock sites: Bulletin of the Seismological Society of America, v. 87, no. 2, p. 327-341.

Boore, D. M., Joyner, W. B., and Fumal, T. E., 1997, Equations for estimating horizontal response spectra and peak acceleration from western North American earthquakes: A summary of recent work: Seis. Res. Lett., v. 68, p. 127-153.

Bouchon, M., and Barker, J. S., 1996, Seismic response of a hill: The example of Tarzana, California: Bulletin of the Seismological Society of America, v. 86, no. 1, p. 66-72.

Bray, J. W., and Goodman, R. E., 1981, The Theory of Base Friction Models: International Journal of Rock Mechanics and Mining Sciences, v. 18, p. 453-468.

Brideau, M. A., and Stead, D., 2010, Controls on Block Toppling Using a Three-Dimensional Distinct Element Approach: Rock Mechanics and Rock Engineering, v. 43, no. 3, p. 241-260.

Burridge, R., Mainardi, F., and Servizi, G., 1980, Soil amplification of plane seismic waves: Physics of the Earth and Planetary Interiors, v. 22, no. 2, p. 122-136.

Caputo, R., Hinzen, K. G., Liberatore, D., Schreiber, S., Helly, B., and Tziafalias, A., 2011, Quantitative archaeoseismological investigation of the Great Theatre of Larissa, Greece: Bulletin of Earthquake Engineering, v. 9, no. 2, p. 347-366.

Cruz, E., Riddell, R., and Midorikawa, S., 1993, A study of site amplification effects on ground motions in Santiago, Chile: Tectonophysics, v. 218, no. 1-3, p. 273-280.

Doolin, D. M., and Sitar, N., 2004, Time integration in discontinuous deformation analysis: Journal of Engineering Mechanics ASCE, v. 130, no. 3, p. 249-258.

Fabian, P., 1998, Evidence of earthquake destruction in the archaeological record - the case of ancient Avedat., *in* IGS Ann. Meeting, Mizpe Ramon.

Field, E. H., 1996, Spectral amplification in a sediment-filled valley exhibiting clear basin-edge-induced waves: Bulletin of the Seismological Society of America, v. 86, no. 4, p. 991-1005.

Goodman, R. E., and Bray, J. W., 1976, Toppling of rock slopes, *in* Specialty conference on rock engineering for foundations and slopes, Boulder, Colorado, p. 201-234.

Goodman, R. E., and Seed, H. B., 1966, Earthquake-induced displacements in sand embankments: J.Soil Mech. Foundation Div, ASCE, v. 90, no. SM2, p. 125-146.

Hatzor, Y. H., Arzi, A. A., Zaslavsky, Y., and Shapira, A., 2004, Dynamic stability analysis of jointed rock slopes using the DDA method: King Herod's Palace, Masada, Israel: International Journal of Rock Mechanics and Mining Sciences, v. 41, no. 5, p. 813-832.

Heyman, J., 1982, The Masonry Arch: Chichester, Ellis Horwood Limited, 117 p.

Heyman, J., 1997, The stone skeleton: Cambridge, Cambridge University Press.

Hilbert, L. B., Yi, W., Cook, N. G. W., Cai, Y., and ., G.-P. L., 1994, A new discontinuous finite element method for interaction of many deformable bodies in geomechanics, *in* Proceedings of the Eighth International Conference on Computer Methods and Advances in Geomechanics., p. 831-836.

Hinzen, K. G., 2009, Simulation of Toppling Columns in Archaeoseismology: Bulletin of the Seismological Society of America, v. 99, no. 5, p. 2855-2875.

Hinzen, K. G., 2012, Rotation of vertically oriented objects during earthquakes: Journal of Seismology, v. 16, no. 4, p. 797-814.

Hinzen, K. G., Fleischer, C., Reamer, S. K., Schreiber, S., Schutte, S., and Yerli, B., 2011, Quantitative methods in archaeoseismology: Quaternary International, v. 242, no. 1, p. 31-41.

Hoek, E., and Bray, J. W., 1977, Rock Slope Engineering: London, The Institution of Mining and Metallurgy, 402 p.

Housner, G. W., 1963, The behavior of inverted pendulum structures during earthquakes: Bulletin of the Seismological Society of America, v. 53, no. 2, p. 403-417.

Idriss, I. A., and Seed, H. B., 1967, Response of horizontal soil layers during earthquakes: Department of Civil Engineering, Institute of Transportation and Traffic, University of California, Berkeley.

Jing, L., 2003, A review of techniques, advances and outstanding issues in numerical modeling for rock mechanics and rock engineering: Int. J. Rock Mech. Min. Sci., v. 40, p. 283-353.

Jing, L., and Hudson, J. A., 2002, Numerical methods in rock mechanics: International Journal of Rock Mechanics and Mining Sciences, v. 39, no. 4, p. 409-427.

Jing, L., and Stephansson, O., 2007, Fundamentals of Discrete Element Methods for Rock Engineering: Theory and Applications, Developments in Geotechnical Engineering, Elsevier, Amsterdam

Kamai, R., and Hatzor, Y. H., 2008, Numerical analysis of block stone displacements in ancient masonry structures: a new method to estimate historic ground motions: International Journal for Numerical and Analytical Methods in Geomechanics, v. 32, p. 1321-1340.

Kieffer, S. D., 1998, Rock Slumping – a compound failure mode of jointed hard rock slopes.: U. C. Berkeley.

Liu, C. H., Jaksa, M. B., and Meyers, A. G., 2008, Improved analytical solution for toppling stability analysis of rock slopes: International Journal of Rock Mechanics and Mining Sciences, v. 45, no. 8, p. 1361-1372.

Lysmer, J., Seed, H. B., and Schanable, P. B., 1972, SHAKE - A computer program for earthquake response analysis for horizontally layered sites: Berkeley, U. o. C. Rpt. EERC 72-12.

MacLaughlin, M. M., and Doolin, D. M., 2006, Review of validation of the discontinuous deformation analysis (DDA) method: International Journal for Numerical and Analytical Methods in Geomechanics, v. 30, no. 4, p. 271-305.

Majdi, A., and Amini, M., 2011, Analysis of geo-structural defects in flexural toppling failure: International Journal of Rock Mechanics and Mining Sciences, v. 48, no. 2, p. 175-186.

Makris, N., and Roussos, Y. S., 2000, Rocking response of rigid blocks under near-source ground motions: Geotechnique, v. 50, no. 3, p. 243-262.

Mazor, E., and Korjenkov, A., 2001, Applied Archeoseismology, *in* Mazor, E., and Krasnov, B., eds., The Makhteshim Country Laboratory of Nature: Moscow, Pensoft, p. 123-136.

Negev, A., 1988, The Nabatean cities in the Negev, 62-63.

NEHRP, 2004, Building Seismic Safety Council Federal Emergency Management Agency FEMA 450.

Newmark, N., 1965, Effects of earthquakes on dams and embankments: Geotechnique, v. 15, no. 2, p. 139-160.

Ohnishi, Y., Nishiyama, S., Sasaki, T., and Nakai, T., 2005, The application of DDA to practical rock engineering problems: issues and recent insights, *in* Proceedings of the 7th International Conference on the Analysis of Discontinuous Deformation, Honolulu, Hawaii, p. 277-287.

Olsen, K. B., 2000, Site amplification in the Los Angeles basin from three-dimensional modeling of ground motion: Bulletin of the Seismological Society of America, v. 90, no. 6, p. S77-S94.

Onn, A., Weksler-Bdolah, S., and Bar-Nathan, R., 2011, Jerusalem, The Old City, Wilson’s Arch and the Great Causeway: Hadashot Arkheologiyot – Excavations and Surveys in Israel, v. 123.

S.I.I., 2004, Israel Building Code #413, 2nd amendment: The Standards Institution of Israel.

Sagaseta, C., 1986, On the modes of instability of a rigid block on an inclined plane: Rock Mechanics and Rock Engineering, v. 19, p. 261-266.

Sagaseta, C., Sanchez, J. M., and Canizal, J., 2001, A general analytical solution for the required anchor force in rock slopes with toppling failure: International Journal of Rock Mechanics and Mining Sciences, v. 38, no. 3, p. 421-435.

Schnabel, P. B., Lysmer, J., and Seed, H. B., 1972, SHAKE: A computer program for earthquake response analysis of horizontally layered sites: Earthquake Engineering Research Center, University of California.

Scholtes, L., and Donze, F. V., 2012, Modeling progressive failure in fractured rock masses using a 3D discrete element method: International Journal of Rock Mechanics and Mining Sciences, v. 52, p. 18-30.

Seed, H. B., and Idriss, I. A., 1969, Influence of soil conditions on ground motions during earthquakes: Journal of the Soil Mech. and Found Div., ASCE, v. 95(SM1), p. 99-137.

Semblat, J. F., Duval, A. M., and Dangla, P., 2000, Numerical analysis of seismic wave amplification in Nice (France) and comparisons with experiments: Soil Dynamics and Earthquake Engineering, v. 19, no. 5, p. 347-362.

Semblat, J. F., Kham, A., Parara, E., Bard, P. Y., Pitilakis, K., Makra, K., and Raptakis, D., 2005, Seismic wave amplification: Basin geometry vs. soil layering: Soil Dynamics and Earthquake Engineering, v. 25, no. 7-10, p. 529-538.

Shi, G.-h., 1988, Discontinuous Deformation Analysis – a new numerical method for the statics and dynamics of block system [Ph.D. thesis]: Berkeley, University of California, 378 p.

Shi, G.-h., 1993, Block System Modeling by Discontinuous Deformation Analysis, Topics in Engineering: Southampton, UK, Computational Mechanics Publication, 209 p.

Shi, G.-h., 1996a, Discontinuous Deformation Analysis Programs, version 96, User's manual, *in* Young, R. M.-C., ed.

Shi, G.-h., 1996b, Manifold method, *in* Proceedings of the first international forum on DDA and simulations of discontinuous media, Berkeley, p. 52-262.

Shi, G.-h., 1997, The Numerical Manifold Method and Simplex Integration: Waterways Experiment Station.

Shi, G.-h., 2001, Three dimensional discontinuous deformation analyses, *in* Proceedings of the 38th US Rock Mechanics Symposium, Washington, DC, p. 1421–8.

Shi, G.-h., and Goodman, R. E., 1985 Two dimensional discontinuous deformation analysis: Int J. numer. anal. methods geomech, v. 9, p. 541-556

Shi, G.-h., and Goodman, R. E., 1989, Generalization of two dimensional discontinuous deformation analysis for forward modeling: Int J. numer. anal. methods geomech, v. 13, p. 359-380.

Siddiqqi, J., and Atkinson, G. M., 2002, Ground-motion amplification at rock sites across Canada as determined from the horizontal-to-vertical component ratio: Bulletin of the Seismological Society of America, v. 92, no. 2, p. 877-884.

Sneh, A., and Avni, Y., 2011, Jerusalem, sheet 11-ii: Geological Survey of Israel, scale 1:50000.

Steidl, J. H., Tumarkin, A. G., and Archuleta, R. J., 1996, What is a reference site?: Bulletin of the Seismological Society of America, v. 86, no. 6, p. 1733-1748.

Towhata, I., 2008, Geotechnical earthquake engineering, Springer series in geomechanics and geoengineering: Berlin, Springer.

Vilnay, O., 1988, Dynamic behavior of three-voussoir arch: J. Struct. Eng, ASCE, v. 114, no. 5, p. 1173-1186.

Vilnay, O., and Cheung, S.-S., 1986, Stability of Masonry Arches: J. Struct. Eng, ASCE, v. 112, no. 10, p. 2185-2199.

Voegele, M. D., 1979, Rational Design of Tunnel Supports: an Interactive Graphics Based Analysis of the Support Requirements of Excavations in Jointed Rock Masses: Department of Civil and Mineral Engineering, University of Minnesota, G1-79-15.

Warren, C., 1876, Underground Jerusalem: London, Richard Bentley.

Weksler-Bdolah, S., Onn, A., and Rosenthal-Heginbottom, R., 2009, The Eastern Cardo and the Wilson Bridge in Light of New Excavations - the Remains from the Second Temple Period and from Aelia Capitolina, *in* Di Segni, L., Hirschfeld, Y., Patrich, J., and Talgam, R., eds., Man near a Roman arch: Jerusalem, Israel Exploration Society, p. 135-139, in Hebrew.

Wilson, C. W., Warren, C., Morrison, W., and Stanley, A. P., 1871, The recovery of Jerusalem: New York, D. Appleton.

Yagoda-Biran, G., and Hatzor, Y. H., 2010, Constraining paleo PGA values by numerical analysis of overturned columns: Earthquake Engineering and Structural Dynamics, v. 39, p. 462-472.

Yeung, M. R., 1991, Application of Shi's Discontinuous Deformation Analysis to the Study of Rock Behavior: University of California, Berkeley, 339 p.

Yu, Z., Ishijima, Y., and Sato, M., 1987, Distinct Element Method - Application to Analyze Sliding and Toppling Failures: Nonferrous Metals, v. 39, no. 4, p. 1-11.

Zaslavsky, Y., Perelman, N., Kalmanovich, M., Shvartsburg, A., and Portnov, P., 2011, Experimental assessment of dynamic characteristics of two monuments in Avdat National Park: Geophysical Institute of Israel, 562/608/11.

Zaslavsky, Y., and Shapira, A., 2000a, Experimental study of topographic amplification using the Israel seismic network: Journal of Earthquake Engineering, v. 4, no. 1, p. 43-65.

Zaslavsky, Y., and Shapira, A., 2000b, Questioning nonlinear effects in Eilat during MW=7.1 gulf of Aqaba earthquake, *in* Proceedings, XXVII General assembly of the European Seismological Commission (ESC), Lisbon, Portugal, p. 343-347.

Zilberman, E., 1989, Landscape development in the central, northern and north-western Negev in the Neogene and Quaternary [in Hebrew]. Hebrew University, Jerusalem.